condensed matter

# Nanoscience and Nanotechnology, Proceedings of the INFN-LNF 2018 Conference

Edited by
Stefano Bellucci

Printed Edition of the Special Issue Published in *Condensed Matter*

www.mdpi.com/journal/condensedmatter

MDPI

# Nanoscience and Nanotechnology, Proceedings of the INFN-LNF 2018 Conference

# Nanoscience and Nanotechnology, Proceedings of the INFN-LNF 2018 Conference

Special Issue Editor

**Stefano Bellucci**

MDPI • Basel • Beijing • Wuhan • Barcelona • Belgrade

*Special Issue Editor*
Stefano Bellucci
INFN-Laboratori Nazionali di Frascati
Italy

*Editorial Office*
MDPI
St. Alban-Anlage 66
4052 Basel, Switzerland

This is a reprint of articles from the Special Issue published online in the open access journal *Condensed Matter* (ISSN 2410-3896) from 2018 to 2019 (available at: https://www.mdpi.com/journal/condensedmatter/special_issues/Nano2018).

For citation purposes, cite each article independently as indicated on the article page online and as indicated below:

LastName, A.A.; LastName, B.B.; LastName, C.C. Article Title. *Journal Name* **Year**, *Article Number*, Page Range.

**ISBN 978-3-03921-968-1 (Pbk)**
**ISBN 978-3-03921-969-8 (PDF)**

Cover image courtesy of Claudio Federici (INFN-LNF).

# Contents

# About the Special Issue Editor

**Stefano Bellucci** obtained the Laurea in Physics Degree at University Sapienza Rome (summa cum laude) in 1982 and his Ph.D. in Physics of elementary particles at SISSA, Trieste, in 1986. He worked as a Research Associate at Brandeis University, Waltham, MA, USA (1983–1985); as a visiting researcher at M.I.T., Cambridge, MA, USA (1985–1986), at University of Maryland, USA (1986–1987), at University of California at Davis, USA (1987–1988). He was appointed as a Tenured Researcher (Research Staff) at INFN (Istituto Nazionale di Fisica Nucleare) Laboratori Nazionali di Frascati (LNF) in 1987. He was appointed as INFN First Researcher (Senior Research Staff) in 2005. In 2013, the Italian Ministry of University habilitated him as Full Professor in Theoretical Physics of Fundamental Interactions and in Theoretical Condensed Matter Physics. He coordinated (1999–2002, 2011–2015) all LNF theoretical physics activities. His research interests include theoretical physics, condensed matter, biophysics, physical chemistry, nanoscience and nanotechnology, nanocarbon-based composites, toxicology, biomedical applications. His lab has cultivated over 40 Ph.D. and master students. He has published over 550 papers with 12107 citations (4611 citations since 2014) in peer-reviewed journals with Hirsch index h = 52, and more than 10 invited book chapters, http://scholar.google.com/citations?hl=en&user=mOq8urEAAAAJ. He is the editor and/or co-author of over 10 books with Springer. He is in the list of Top Italian Scientists published by VIA Academy. Received B.W. Lee Prize at Erice School of Subnuclear Physics (Erice, Italy) 1982. In 1980, he was selected as Summer student at CERN (Geneva). He led INFN applied physics CSN5 experiments: 2006–2010 NEXT for new electron sources and X radiation, 2004–2006 MINCE for micro and nanotechnology, 2001–2004 NANO for carbon-based nanotechnology. From 2007 to 2010, he was INFN Scientist and technologist in charge of the EU FP7-ICT-2007-1 Collaborative Project CATHERINE "Carbon nAnotube Technology for Highspeed nExt-geneRation nano-InterconNEcts". He is the Series Editor of Springer Lecture Notes in Nanoscale Science and Technology, and was the biannual (2012–2014) Associate Editor of Nanoscience and Nanotechnology Letters. He is an Editorial Board Member of and many scientific journals, e.g., the Journal of Nanomaterials, Computer Modelling and New Technologies. Editor in Chief of the MDPI journal Materials, in the Section Board for "Carbon Materials". He is Director of the NATO Emerging Security Challenges Division, SPS Programme projects "Nanocomposite based photonic crystal sensors of biological and chemical agents," "Development of Biosensors using Carbon Nanotubes". He is the INFN scientist in charge of the EU project "Graphene-Based Revolutions in ICT and Beyond, GRAPHENE Flagship" Core1, and the INFN scientist in charge of the Italian Ministry of Health project "Delivery and imaging of miRNAs by multifunctional carbon nanotubes and circulating miRNAs as innovative therapeutic and diagnostic tools for pediatric pulmonary hypertension" and of the Italian Space Agency project "SHAPE—A New Theoretical Framework of the Microgravity-Cell Interaction". He is the LNF Spokesperson of the NEMESYS Condensed Matter Theory INFN CSN4 project.

# Preface to "Nanoscience and Nanotechnology, Proceedings of the INFN-LNF 2018 Conference"

Nanoscience and Nanotechnology, Proceedings of the INFN-LNF 2018 Conference. Since 2000, the NEXT Nanotechnology group at INFN—Laboratori Nazionali di Frascati (LNF) has organized an annual series of international meetings in the area of nanotechnology. The 2018 conference was devoted to recent developments in nanoscience and their manifold technological applications. The conference consisted of several tutorial/keynote lectures, as well as research talks presenting frontier nanoscience research developments and innovative nanotechnologies in the areas of biology, medicine, aerospace, optoelectronics, energy, materials and characterizations, and low-dimensional nanostructures and devices. Selected, original papers based on the 2018 conference talks and related discussions have been published, after a careful refereeing process, in the MDPI journal Condensed Matter and are included in the present dedicated issue.

**Stefano Bellucci**
*Special Issue Editor*

condensed matter

MDPI

*Editorial*

# Nanoscience and Nanotechnology, Proceedings of the INFN-LNF 2018 Conference

**Stefano Bellucci**

INFN-Laboratori Nazionali di Frascati, Via E. Fermi 40, 00044 Frascati, Italy; bellucci@lnf.infn.it

Received: 5 November 2019; Accepted: 8 November 2019; Published: 13 November 2019

**Abstract:** The NEXT Nanotechnology group at INFN-Laboratori Nazionali di Frascati (LNF) has organized, since the year 2000, a yearly series of international meetings in the area of nanotechnology. The 2018 conference has been devoted to recent developments in nanoscience and their manifold technological applications. These consisted of a number of tutorial/keynote lectures, as well as research talks presenting frontier nanoscience research developments and innovative nanotechnologies in the areas of biology, medicine, aerospace, optoelectronics, energy, materials and characterizations, low-dimensional nanostructures and devices. Selected, original papers based on the 2018 conference talks and related discussions have been published, after a careful refereeing process, in the MDPI journal *Condensed Matter*, and are currently included in the present dedicated issue.

**Keywords:** chemical stability; graphene; temperature dependence in HOPG; electrodeposition process; boron sheet's electronic structure

## 1. Introduction

The Physics and Chemistry of Nanostructures, a fast-growing research field which has attracted increasing attention over many years, especially for many promising nanotechnological applications, led me in 1999 to plan, install, and coordinate the so-called NEXT nanotechnology Laboratories, hosted within the INFN-Laboratori Nazionali di Frascati, near Rome (Italy).

One of the main objectives of such Laboratories is to allow us, on the one hand, experimental tests of theories, models, and simulations and, on the other hand, to design and realize devices, which may yield a prototype for industrial exploitation, in such a way as to constitute a basis for Technology Transfer.

At NEXT, we always believed to be of crucial importance, for the quality of the research, to work in a national or international context which, through collaborations and public research financed projects, can promote professional growth, yielding results with a high impact on the scientific community, producing, whenever possible, useful applications [1,2]. Training and, in general, teaching have always occupied a central place in the NEXT activities, as we believe it is imperative to make the developed methods, and the obtained results, available to younger generations.

Working actively in such a multidisciplinary field led us, also in this respect, into the parallel activity of schools and workshops organization, as well as editorial projects. Hence, we organized, since the year 2000, a series of international meetings in the area of nanoscience and its nanotechnological applications. The conferences have been held under the patronage of INFN (Italian Institute for Nuclear Physics), CNR (Italian Research Council), and various universities, in close collaboration with industrial partners, including 3M, MTS, RS Components, VARIAN, MICOS, Newport, Veeco, and many more.

The 20 yearly meetings on nanoscience and nanotechnology (n&n) 2000–2019, hosted important lecturers, e.g., O. Groening, P. Kelires, I. Berbezier, R. Garcia, J. Gonzalez, J. Solyom, R. Cingolani, J. Kirschner, K.Takayanagi, M. Terrones, L. Vescan, B. Yakobson, U. Valbusa, R. Egger, M. Pimprikar, N.

Pugno, V. Balzani, P. Baglioni, B. Fubini, J.M. Kenny, M.S. Sarto, F. Beltram, P. Milani, K. Wandelt, B. Voigtlaender, L. Balents, G. Grasso, targeting as an audience young postdocs and PhD students, assessing the state-of-the-art of frontier nanoscience research developments and innovative nanotechnologies in the areas of biology, medicine, aerospace, optoelectronics, energy, materials and characterizations, low-dimensional nanostructures and devices.

From this activity, many proceedings collections, as well as 3 Springer-edited volumes, originated [3–13]. Of the latter volumes, the book on biomedical applications of nanoparticles—Nanoparticles and Nanodevices in Biological Applications: The INFN Lectures—is one of the very first attempts to write a series of books on selected topics in Nanoscale Science and Technology based on lectures given at the well-known INFN schools of the same name. The aim of this collection is to provide a reference corpus of suitable, introductory material to relevant subfields, as they mature over time, by gathering the significantly expanded and edited versions of tutorial lectures, given over the years by internationally known experts. A recent example can be found in [14].

## 2. Fluctuation Theory in Chemical Kinetics

In the paper [15], stability properties of chemical reactions of arbitrary orders have been considered. In each chemical experiment, the formation of a chemical equilibrium can be studied by optimizing the reaction rate. Under infinitesimal simultaneous variations of the concentrations of reacting species, the binary component equilibrium is achieved when either one of the orders or concentrations of reactants vanishes. The chemical concentration capacities of the components are calculated to describe the local stability of the equilibrium. The correlation between the components is obtained as the mixed second-order derivative of the rate with respect to concentrations. The global stability analysis is performed by introducing a symmetric matrix with its diagonal components as the chemical capacities and off-diagonal components as the local correlation. It turns out that the local chemical stability requires the orders of the reactants to be either negative or larger than unity. The corresponding global stability requires the positivity of a cubic factor over the orders of the reactants. This illustrates how a chemical reaction takes place by attaining its activation state and asymptotically approaches the equilibrium when two components are mixed with arbitrary orders. Qualitative discussions are provided to support our analysis towards the formation of an optimized equilibrium. Finally, along with future directions, verification of the model is discussed towards the formation of carbon-based reactions, formation of organic/inorganic chemical equilibria, and catalytic oxidation of $CO–H_2$ mixtures in presence of Pt.

## 3. Effect of High-Temperature Annealing on Graphene with Nickel Contacts

Graphene has shown great potential for ultra-high frequency electronics. However, using graphene in electronic devices creates a requirement for electrodes with low contact resistance. Thermal annealing is sometimes used to improve the performance of contact electrodes. However, high-temperature annealing may introduce additional doping or defects to graphene. Moreover, an extensive increase in temperature may damage electrodes by destroying the metal–graphene contact. In the work [16], the effects of high-temperature annealing on graphene and nickel–graphene contacts were studied. Annealing was done in the temperature range of 200–800 °C, and the effect of the annealing temperature was observed by two and four-point probe resistance measurements and by Raman spectroscopy. It is observed that the annealing of a graphene sample above 300 °C increased the level of doping, but did not always improve electrical contacts. Above 600 °C, the nickel–graphene contact started to degrade, while graphene survived even higher process temperatures.

## 4. Temperature Effects on the HOPG Intercalation Process

Graphite intercalation via chemical strategies is a common procedure to delaminate stratified crystals and obtain a suspension of graphene flakes. The intercalation mechanism at the molecular level is still under investigation in view of enhancing graphene production and reducing damage to

the original pristine crystal. The latter can undergo surface detriment due to both blister evolution and carbon dissolution. The role of the electrolyte temperature in this process has never been investigated. In work [17], by using an in situ atomic force microscopy (AFM) apparatus, the surface morphology changes after the application of fast cyclic-voltammetries at 343 K have been explored, in view of de-coupling the crystal swelling phenomenon from the other electrochemical processes. It was found that blisters do not evolve because of the increasing temperature, while the quality of the graphite surface becomes significantly worse, due to the formation of some adsorbates on possible defect sites of the electrode surface. These results suggest that the chemical baths used in graphite delamination must be carefully monitored in temperature for avoiding undesired electrode detriment.

## 5. Model of Nano-Metal Electroplating Process in Trapezoid Profile Groove

The principle of the electrodeposition method is to immerse the coated products in a water electrolyte solution, the main components of which are salts or other soluble compounds—metal coatings. The process of electrodeposition of metals is important in micro- and nano-electronics, as it is used in the production of multilayer printed circuit boards (MPC). MPCs consist of many layers, most of which are complex electrical circuits. The simplicity, availability, and technological capabilities of the electrodeposition process make it possible to use it for local electrochemical deposition, especially with an unchanged decrease in topological dimensions. Electrodeposition is a complex process occurring at the interface of type 1 and 2 conductors, and depends on various factors such as temperature, mixing rate, and electrolyte composition, as well as ion solvation processes, adsorption at the phase boundary, the state of the double electric layer, the phenomena of electrode polarization, diffusion, and convection flows near the deposition surface. However, the process of local metallization is affected by a complex surface relief.

In some cases, mathematical modeling methods can replace a full-scale experiment, saving material and time costs. In this article, we consider the possibility of mathematical modeling of electrochemical deposition of copper and silver under local metallization in a hollow trapezoidal profile groove using the basic package of COMSOL Multiphysics. The software COMSOL Multiphysics was utilized in [18] to perform a simulation of the processes of electrodeposition of the metals copper and silver in the groove of the trapezoidal profile. The results obtained for the thicknesses of the deposited layers of copper and silver can optimize the deposition regimes. For example, it is advisable to carry out metal deposition in a periodic mode, changing the polarity of the electrode to the opposite. This should ensure the alignment of the concentration of metal ions in the depth of the groove, and thus reduce the thickness variation of the layers on the vertical walls.

## 6. Electronic Structure of Boron Flat Holeless Sheet

The electronic band structure, namely energy band surfaces and densities-of-states (DoS), of a hypothetical flat and ideally perfect, i.e., without any type of holes, boron sheet with a triangular network is calculated in [19] within a quasi-classical approach. It is shown to have metallic properties as is expected for most of the possible structural modifications of boron sheets. The Fermi curve of the boron flat sheet is found to be consisted of 6 parts of 3 closed curves, which can be approximated by ellipses representing the quadric energy-dispersion of the conduction electrons. The effective mass of electrons at the Fermi level in a boron flat sheet is found to be too small compared with the free electron mass and to be highly anisotropic. The low effective mass of conduction electrons indicates their high mobility and, hence, high conductivity of the boron sheet. The effects of buckling/puckering and the presence of hexagonal or other type of holes expected in real boron sheets can be considered as perturbations of the obtained electronic structure and theoretically considered as effects of higher order.

## 7. Simulation of the Process of Obtaining Nanoparticles by Thermal Decomposition

Today, nanopowders are in great demand for the creation of new materials and technologies, fundamentally new devices. The process of obtaining nanopowders is therefore an important direction in nanotechnology.

The synthesis of nanocrystalline powders of metals and compounds using pyrolysis is associated with the use of complex and organometallic compounds. Numerous studies show that thermal decomposition is a complex process, depending on a variety of parameters. Therefore, the current task is to develop synthesis methods, that is, the simulation of deposition modes in which the most accurate particles can be obtained. By changing the conditions for thermal decomposition and input parameters, one can control the quality and morphology of the resulting metal nanoparticles.

The goal of the work [20] was to analyze a model for obtaining nanopowders by thermal decomposition. The relevance of the pyrolysis process is that the rate of the formation and growth of metal nanoparticles is regulated by changes in the ratio of the number of reactants and the process temperature. In the work [20], the possibility of modeling the process of thermal decomposition in the COMSOL Multiphysics program for the preparation of nanoparticles of metals and their alloys was determined. To identify the most suitable pyrolysis medium, two environments were presented: A water solution and ethanol.

## 8. Conclusions

With the advent of the era of nanotechnology, many new possibilities emerged to find manifold applications from enabling technologies stemming out of innovative materials [21,22]. An example is graphene, a two-dimensional carbon allotrope, which is characterized by light weight, strength, and very high electrical and thermal conductivity [23,24]. Graphene can be utilized in nanoelectronics to replace conventional materials (e.g. copper), which suffer many limitations, for example in applications involving small sizes and high frequencies [25,26].

The results presented in the present book highlight some of the most recent advances in nanoscience and nanotechnology studies, from both the physical and chemical point of view, with an eye also to possible engineering applications.

These studies demonstrate directly how effective, and at the same time stimulating, implementing the "cross fertilization" procedure is. Indeed, multidisciplinary research allows one to catch more easily the analogies' inherent different areas of science, as well as to take advantage and optimize different methods and techniques, often borrowed from other research areas.

In the present special issue, we included six published papers. The latter contributions, on the one hand, are developed at the theory level and, on the other hand, show experimental results on realization and experimental characterization of nanostructured systems, suitable of yielding progress towards the realization of systems and devices, that can ultimately lead to industrial applications. The results show that recent scientific research advances in these areas may provide important steps in the direction of fostering innovation and technological development.

**Acknowledgments:** I wish to thank the sponsors of the conference on Nanoscience and Nanotechnology 2018, i.e. INFN, Metreo, Nanovea, Qi Technologies, Graphen Tech for their support. I am grateful to A. Cataldo for his collaboration in the organization of the conference.

**Conflicts of Interest:** The author declares no conflict of interest.

## References

1. Bellucci, S. Carbon nanotubes: Physics and applications. *Phys. Status Solidi(c)* **2005**, *2*, 34–47. [CrossRef]
2. Bellucci, S. Nanotubes for particle channeling, radiation and electron sources. *Nucl. Instrum. Methods Phys. Res. B.* **2005**, *234*, 57–77. [CrossRef]
3. De Crescenzi, M.; Bellucci, S. Nanoscience and nanotechnology 2001. *J. Phys. Condens. Matter* **2003**, *18*, 1967–1971.

4. Bellucci, S. Guest Editorial: Selected Papers from the INFN-LNF Conference on Nanoscience and Nanotechnology. *J. Phys. Condens. Matter* **2006**, *18*, S1967–S2238. [CrossRef]
5. Bellucci, S. Proceedings of the International School and Workshop 'Nanoscience and Nanotechnology 2006', Rome, Italy, 6–9 November 2006. *J. Phys. Condens. Matter* **2007**, *19*, 390301–395024. [CrossRef]
6. Bellucci, S. Guest Editorial: Selected Papers from the INFN-LNF Conference on Nanoscience and Nanotechnology. *J. Phys. Condens. Matter* **2008**, *20*, 474201–474214. [CrossRef]
7. Bellucci, S. Guest Editorial: Selected Papers from the INFN-LNF Conference on Nanoscience and Nanotechnology. *J. Nanophotonics* **2009**, *3*, 031999. [CrossRef]
8. Bellucci, S. Nanoparticles and Nanodevices in Biological Applications. In *The INFN Lectures-Lecture Notes in Nanoscale Science and Technology, 4*; Springer: Berlin, Germany, 2009; Volume I. [CrossRef]
9. Bellucci, S. Selected Peer-Reviewed Articles from the INFN-LNF Conference on Nanoscience and Nanotechnology. *Nanosci. Nanotechnol. Lett.* **2011**, *3*, 815. [CrossRef]
10. Bellucci, S. Physical Properties of Ceramic and Carbon Nanoscale Structures. In *The INFN Lectures-Lecture Notes in Nanoscale Science and Technology, 11*; Springer: Berlin, Germany; Volume II. [CrossRef]
11. Bellucci, S. A Special Issue dedicated to the Conference on Nanoscience and Nanotechnology. *Nanosci. Nanotechnol. Lett.* **2012**, *4*, 1031–1032. [CrossRef]
12. Bellucci, S. Self-Assembly of Nanostructures. In *The INFN Lectures, Lecture Notes in Nanoscale Science and Technology, 12*; Springer: Berlin, Germany, 2012; Volume III. [CrossRef]
13. Bellucci, S. Selected Peer-Reviewed Articles from the INFN-LNF Conference on Nanoscience and Nanotechnology. *Nanosci. Nanotechnol. Lett.* **2013**, *5*, 1131. [CrossRef]
14. Shunin, Y.; Bellucci, S.; Gruodis, A.; Lobanova-Shunina, T. Nonregular Nanosystems: Theory and Applications. In *Lecture Notes in Nanoscale Science and Technology, 26*; Springer: Cham, Switzerland, 2018. [CrossRef]
15. Tiwari, B.N.; Kishore, S.C.; Marina, N.; Bellucci, S. Fluctuation Theory in Chemical Kinetics. *Condens. Matter* **2018**, *3*, 49. [CrossRef]
16. Kaplas, T.; Jakstas, V.; Biciunas, A.; Luksa, A.; Setkus, A.; Niaura, G.; Kasalynas, I. Effect of High-Temperature Annealing on Graphene with Nickel Contacts. *Condens. Matter* **2019**, *4*, 21. [CrossRef]
17. Bussetti, G.; Yivlialin, R.; Goletti, C.; Zani, M.; Duò, L. Temperature Effects on the HOPG Intercalation Process. *Condens. Matter* **2019**, *4*, 23. [CrossRef]
18. Egorova, O.Y.; Kosushkin, V.G.; Kozhitov, L.V. Model of Nano-Metal Electroplating Process in Trapezoid Profile Groove. *Condens. Matter* **2019**, *4*, 26. [CrossRef]
19. Chkhartishvili, L.; Murusidze, I.; Becker, R. Electronic Structure of Boron Flat Holeless Sheet. *Condens. Matter* **2019**, *4*, 28. [CrossRef]
20. Kuzmicheva, A.; Kosushkin, V.; Kozhitov, L. Simulation of the Process of Obtaining Nanoparticles by Thermal Decomposition. Condens. *Matter* **2019**, *4*, 19.
21. Geim, A.K. Graphene: Status and prospects. *Science* **2009**, *324*, 1530–1534. [CrossRef]
22. Van Noorden, R. Moving towards a graphene world. *Nature* **2006**, *442*, 228–229. [CrossRef]
23. Neto, A.; Guinea, F.; Peres, N.M.R.; Novoselov, K.S.; Geim, A.K. The electronic properties of graphene. *Rev. Mod. Phys.* **2009**, *81*, 109–162. [CrossRef]
24. Balandin, A.A.; Ghosh, S.; Bao, W.; Calizo, I.; Teweldebrhan, D.; Miao, F.; Lau, C.N. Superior Thermal Conductivity of Single-Layer Graphene. *Nano Lett.* **2009**, *8*, 902–907. [CrossRef]
25. Avouris, P.; Chen, Z.; Perebeinos, V. Carbon-based electronics. *Nat. Nanotechnol.* **2007**, *2*, 605–615. [CrossRef] [PubMed]
26. Freitag, M. Physics in the nanoworld. *Nat. Nanotechnol.* **2008**, *3*, 455–457. [CrossRef] [PubMed]


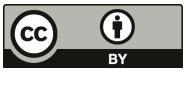

condensed matter

MDPI

*Article*

# Fluctuation Theory in Chemical Kinetics

**Bhupendra Nath Tiwari [1,2,*], S. Chandra Kishore [1], Ninoslav Marina [1,3] and Stefano Bellucci [2]**

[1] University for Information Science and Technology, St. Paul the Apotle, Ohrid 6000, Macedonia; Chandra.kishore@uist.edu.mk (S.C.K.); ninoslav.marina@uist.edu.mk (N.M.)
[2] INFN-Laboratori Nazionali di Frascati, Via E. Fermi 40, 00044 Frascati, Italy; bellucci@lnf.infn.it
[3] School of Engineering and Applied Science, Princeton University, Princeton, NJ 08544, USA
* Correspondence: bntiwari.iitk@gmail.com

Received: 12 November 2018; Accepted: 12 December 2018; Published: 17 December 2018

**Abstract:** In this research, we study the stability properties of chemical reactions of arbitrary orders. In a given chemical experiment, we focus on the formation of a chemical equilibrium by optimizing the reaction rate. Under infinitesimal simultaneous variations of the concentrations of reacting species, the binary component equilibrium is achieved when either one of the orders or concentrations of reactants vanishes. The chemical concentration capacities of the components are calculated to describe the local stability of the equilibrium. The correlation between the components is obtained as the mixed second-order derivative of the rate with respect to concentrations. The global stability analysis is performed by introducing a symmetric matrix with its diagonal components as the chemical capacities and off-diagonal components as the local correlation. We find that the local chemical stability requires the orders of the reactants to be either negative or larger than unity. The corresponding global stability requires the positivity of a cubic factor over the orders of the reactants. In short, our consideration illustrates how a chemical reaction takes place by attaining its activation state and asymptotically approaches the equilibrium when two components are mixed with arbitrary orders. Qualitative discussions are provided to support our analysis towards the formation of an optimized equilibrium. Finally, along with future directions, we discuss verification of our model towards the formation of carbon-based reactions, formation of organic/inorganic chemical equilibria and catalytic oxidation of $CO - H_2$ mixtures in presence of Pt.

**Keywords:** chemical stability; reaction rate; chemical equilibria; fluctuation theory; kinetic theory

## 1. Introduction

For several decades, the study of equilibrium in chemical reactions has provided a broad scope for research in the field of chemical physics by exploiting the concept of collision theory [1]. From this viewpoint of chemical kinetics, the equilibrium formation plays an important role in the occurrence of a chemical reaction. According to the concept of collision theory, various atoms, molecules, and ions collide with each other to create a pathway for the completion of the reaction. Thus, the temperature and concentration of reacting species arise as the governing parameters of the corresponding chemical rate. This follows from the notion of the collision energy and molecular structures [1,2]. It is worth mentioning that the rate constant of the reaction varies as an exponential function of the temperature [2]. In this concern, it is well understood that an increase in the temperature increases the rate of the reaction, therefore an enhanced formation of products.

Here, under varying concentrations and orders of reacting species, we focus on analytical solutions of the rate equation of a given chemical reaction. Namely, our investigation allows to access the nature of the chemical equilibrium as a function of input parameters. In the light of the collision theory, this is realized by the existing information that a chemical reaction takes place based on a transition state model [3]. Herewith, a product is formed via an intermediate state [4], when its corresponding energy

crosses the barrier potential, termed as the activation energy, also see [5] for the associated quantum mechanical effects. In the sequel, we illustrate functionalities of the chemical rate of an arbitrary single stage reaction by considering its occurrence at a definite temperature and composition of the reaction, viz. the concentration of constituents. Consequently, the forward and backward rates depend upon the concentration of the reactants and that of the products, respectively. In this context [6], as a function of the concentration of constituents, fluctuations in the chemical rate could explain the formation of an irreversible reaction, as well.

Considering the microscopic aspects, molecular structures of various reacting species contribute towards the happening of a chemical reaction [7,8]. Furthermore, the reaction rate varies with respect to the frequency factor of the products, as well. Notice that the rate is directly related to the structural complexities, viz. the collision frequency and orientation probability factor of the species [9]. Briefly, parameters governing the rate of a chemical reaction are summarized [10] as follows. Firstly, at a constant temperature, the rate generically decreases as a monotonic function with respect to its duration. Secondly, at a given temperature, for an irreversible reaction, the rate largely depends on the concentration of the participating species, see [11]. Thirdly, the rate constant depends on the temperature as per the Arrhenius's first law [6]. In a nutshell, at a constant temperature, the rate of an arbitrary reaction can be factored as a weighted product of the concentrations of the species. Therefore, for a given reversible reaction, the change of the concentration of the reactants per unit time (or that of the product) define its rate.

To examine fundamentals concerning chemical interactions, we require an understanding of the chemical affinity and reactivity of participating species, see [12] for experimental perspectives concerning aqueous solution and its implications. For example, the notion of a chemical bond arises from the concept of chemical affinity [13]. This occupies a key importance in chemistry to rationalize the notion of the reactivity and performance of compounds, in addition to their variations of physical states with respect to the temperature and pressure. We notice that the chemical affinity [12] can be viewed as an electronic property, whereby dissimilar species form new chemical compounds. In this concern, the reason follows from the physical properties of the atoms and molecules [7,8]. Specifically, for a given set of dissimilar reactants, we can describe the tendency of atoms or compounds to form a new state via the corresponding chemical reaction. In this scenario, it is worth stating that certain atoms or molecules possess the ability to aggregate each other to form a definite bonding.

Mostly statistical and thermodynamic factors are used to determine characteristics of a given chemical reaction [14,15]. Fundamentally, such notions emerge as factors affecting the rate of the chemical reaction, see [13] for an introduction towards a universal chemical attraction and combinations. Following the same, we can measure the chemical affinity of the reacting species via their chemical rates [4,13]. Various aspects towards the happening of a chemical reaction are governed via the formation of an equilibrium. As mentioned before, this concept well correlates with the rate of a chemical reaction and its reversibility. Furthermore, Ref. [16] provides theoretical and experimental accounts of chemical kinetics and chemical physics.

In the present study, we emphasize the chemical equilibrium formation by invoking the setup of the fluctuation theory [17–22]. This had various applications in examining the stability properties of condensed matter systems [17], black objects [18], equilibrium thermodynamics [19,20] and optical systems [22]. In this concern, one of the authors [21] has demonstrated the associated geometric perspectives of stability in the light of entropy functions. From this motivation, our primary objective is to examine the nature of the chemical equilibrium and system stabilities when the concentrations of one or more species are varied. Following the above viewpoints, we provide a detailed account of fluctuation theory relations to chemical kinetics towards an optimal happening of chemical reactions.

Following the above observations, we discuss fluctuations of the rate of an arbitrary reaction to offer guidelines towards the modeling of organic and inorganic chemical interactions [23]. Namely, we provide the fluctuation theory analysis of the equilibrium formation under variations of the concentrations $\{c_1, c_2\}$ of reactants $\{A, B\}$ with their partial orders $\{m, n\}$. As per the above analysis,

for any positive concentrations $c_1$ and $c_2$ of the reactants $A$ and $B$, we find that the stability of an equilibrium solely depends on the partial orders $m$ and $n$ of the reactants. In this concern, we provide a comparative analysis of various organic and inorganic chemical equilibrium formations with respect to variations of the concentrations and orders of $A$ and $B$.

Namely, for the zeroth-order reaction with its order $m + n = 0$, the stability of equilibrium depends on the product of $m$ and $n$. Similarly, for the first-order reactions, i.e., when $m + n = 1$, we find that the fluctuation determinant vanishes identically. For a second- or higher-order reaction with $m + n \geq 2$, we notice that the sign of the fluctuation determinant varies as the negative of the product of the partial orders $m$ and $n$ of the reactants $A$ and $B$ respectively. Indeed, our analysis remains valid for fractional- and negative-order reactants and their equilibrium formation [24,25]. This is because our analysis is valid for any real valued concentrations $c_1$ and $c_2$ and any real values of the partial orders $m$ and $n$ of the reactants $A$ and $B$ forming the equilibrium. Our model is further supported by various inorganic and organic equilibrium formations as well as a catalytic oxidation of $CO - H_2$ mixtures in presence of Pt. This offers a clear-cut classification of the inorganic and organic chemical equilibria, happening of an arbitrary chemical reaction and the formation of new products.

The rest of the presentation is organized as follows. In Section 2, we provide a brief account of reaction mechanism and kinetic rate, viz. the notion of a chemical equilibrium and fluctuation theory. In Section 3, we compute the stability quantities concerning a chemical equilibrium under fluctuations of the reaction rate with respect to concentrations of the reactants. In Section 4, we offer qualitative discussions of the results and their interpretations towards the formation of a chemical equilibrium. In Section 5, we discuss verification of our model towards the formation of an inorganic or organic equilibrium, and catalytic oxidation of $CO - H_2$ mixtures in presence of Pt. The perspective directions and future scope emerging from our proposition are highlighted in Section 6. In Section 7, we briefly summarize by offering the conclusions.

## 2. Reaction Mechanisms and Kinetic Rates

In this section, we begin by recalling fundamentals of chemical reactions towards the formation of a chemical equilibrium [26]. First, a chemical reaction is said to occur when the reactants change into products. The progress of such a change is governed by the laws of chemical kinetics [2], which deal with the changes that take place in a given reaction. Herewith, we mainly focus on the reaction rate that depends on the concentration of reactants and products. Please note that the concentrations taken here can be expressed either in the unit of the mass, molar or volume depending upon the state of the reacting species.

### *2.1. Chemical Equilibrium*

In this section, we provide a brief overview of the chemical rate to study its fluctuation theory properties. From perspectives of a chemical equilibrium formation [26], we focus on an arbitrary chemical reaction with a given set of reactants and products. From the viewpoints of chemical science, the equilibrium is pictured as an extremal system at which the amount of the species involved remain unchanged unless an external force is applied to it. For reason, a chemical equilibrium is formed at a constant temperature, pressure, volume, and composition of the reacting species. Furthermore, it is worth mentioning that a chemical equilibrium taking place in a closed system [27] can be represented as

$$\text{Reactant} \rightleftharpoons \text{product}, \tag{1}$$

where "$\rightleftharpoons$" represents the chemical equilibrium among the reactants and products. In the sequel, it follows that a chemical equilibrium can be understood based on macroscopic observations [7,8]. Normally, it is achieved when the forward and reverse reactions take place with a constant rate, where the macroscopic amount of chemical species remains the same.

Historically, an explanation for the conversion occurring in a given chemical reaction in an equilibrium condition was proposed by Leopold Pfaundler von Hadermur during 1880's. A priori, von Hadermur hypothesized the concept of a chemical reaction based on his observations following from the kinetic theory of gases with reference to collisions [1] between the molecules as early as 1867. In particular, at a given temperature, he observed that the equal number of molecules were created and dissociated in due course of their collisions. His theory also suggests that there cannot be the same translational and internal energy for all molecules [7,8]. This is because the collisions of the selected molecules can contribute to the formation of reaction, which solely happens by creating or dissociating the molecules. Consequently, the concept of the chemical affinity arises via the kinetic and statistical interactions among all possible molecules.

The concept of the chemical affinity [13] was further examined by equilibrium displacement mechanism by Guldberg, Waage and Berthollet, which indicates that one cannot explain the formation of an equilibrium only by the mass of the species in a given solution, see [28] for a recent account. Thus, to achieve a chemical equilibrium, one eventually exploits the concept of the active masses of the species, viz. their concentrations.

In general, given an arbitrary single component reaction $A \to B$ with $[A]$ as the concentration of the reactant $A$, its rate [13] is defined as per the ratio

$$\text{Rate} := -\frac{\Delta[A]}{\Delta t}, \tag{2}$$

where $\Delta[A]$ represents the change in the concentration $[A]$ in the time interval $\Delta t$. Similarly, for the product $B$ having concentration $[B]$, its corresponding rate [13] is defined as

$$\text{Rate} := +\frac{\Delta[B]}{\Delta t} \tag{3}$$

It is worth mentioning that the above equilibrium is not immediately achieved. In practice, it could be attained in a few micro to milli seconds. An optimized formation of such equilibria is the subject matter of this research. Notice that the above rate law can be generalized to arbitrary chemical reaction having finitely many reactants and products, as well. Namely, given the most general chemical reaction

$$aA + bB + \ldots \rightleftharpoons cC + dD + \ldots \tag{4}$$

taking place at a constant temperature, its corresponding rate [13] reads as per the power law

$$Rate = k[A]^m[B]^n \ldots, \tag{5}$$

where the constant $k$ is termed as the rate constant of the reaction, exponents $\{m, n, \ldots\}$ represent respective orders and $\{a, b, c, d, \ldots\}$ are the stoichiometric coefficients corresponding the constituents $\{A, B, \ldots\}$. Various chemical reactions have different rates, such as a faster reaction proceeds with a higher rate; however, a slower reaction has a lower rate. First, it is worth emphasizing that a higher rate is attained due to sudden decrease in the concentration of reactants, whereas a lower rate arises due to a slow decrease of their concentrations. For a given chemical reaction, there are mainly four factors that control its rate, viz. the (i) concentration of the reactants, (ii) their physical state, (iii) reaction temperature and (iv) use of catalysts. As mentioned before, the number of collisions of the molecules is directly proportional to the concentration of reactants [1,2]. In general, when more collisions of the molecules occur, an increase in the rate of the reaction takes place. Thus, the concentration of reactants plays an important role in happening of a chemical reaction.

Secondly, the physical state of a reaction depends on the collision frequency, which decides how straightforwardly the reactants can combine. In a given phase of reactants, their molecules are brought into contact by the random thermal motion whereby they get mixed to form a new state. If the phases of reactants are different, the contact between them takes place only at the interface of the phases.

Hence, there is a less possibility of the happening of the reaction. Quantum mechanically, it follows that a vigorous stirring or grinding is needed for a fast happening of the reaction. In addition, the surface area of reactants emerges as an essential quantity in determining the rate of the reaction. It is worth mentioning that finer and smaller solid or liquid reactants—having a greater surface area—create possible active sites for a reactant to interact with others. This leads a faster occurrence of the reaction.

Thus, the temperature plays an important role in enhancing the reaction rate, viz. it increases the frequency of colliding molecules [1]. Namely, an increase in the frequency increases the interaction between the participating molecules, whereby a boost takes place in the rate of the reaction. As the kinetic energy of the molecules depended on their speed, therefore it increases as we increase the temperature of the reaction. As a result, when larger number of molecules collide, we find an increase in the chemical rate. Consequently, the rate of a chemical reaction is measured by changes in the concentration of reactants or that of the products per unit time.

### 2.2. Fluctuation Theory

In this subsection, we focus on the behavior of the chemical rate as in Equation (5) with respect to the concentrations $\{c_1, c_2\}$. To discuss the most general binary component chemical reaction, we consider the formation of an equilibrium for the reaction as in Equation (4). As per this formulation, given a pair of reactants $\{A, B\}$ with their active concentrations $\{[A], [B]\}$ and orders $m$ and $n$ respectively, the forward rate $r_{dir}$ varies as the power law as given by Equation (5) with respect to $\{[A], [B]\}$. Notice further that the orders $\{m, n\}$ remain fixed in a given chemical experiment. With reference to the above observation that $\{c_1, c_2\}$ plays an important role, we investigate the formation of an equilibrium as depicted in Equation (4).

To address the question how the reactants $\{A, B\}$ form an equilibrium, we need to optimize the corresponding rate under infinitesimal variations of $\{c_1, c_2\}$. Namely, at a given time $t = t_0$, with their respective concentrations as $[A] = c_1$ and $[B] = c_2$, from Equation (5), it follows [13] that we have the following reaction rate

$$r(c_1, c_2) = k c_1^m c_2^n \tag{6}$$

Depending upon the state of the reacting species, the concentrations $\{c_1, c_2\}$, when taken as (i) the mass concentration, are measured in $\mathrm{kg/m^3}$, (ii) the molar concentration, are measured in $\mathrm{mol/m^3}$, and (iii) the volume concentration, are dimensionless. Furthermore, it is worth mentioning that the unit of the rate constant $k$ depend upon the global order of a chosen reaction [4,13]. Namely, when the concentrations $\{c_1, c_2\}$ are measured in the units of mol/L, then for the above-mentioned chemical reaction of the order $(m + n)$, the rate constant $k$ has units of $mol^{1-(m+n)} L^{(m+n)-1} s^{-1}$. Thus, from Equation (6), it follows that the rate $r(c_1, c_2)$ has the unit mol/L/s.

In due course of the above reaction, when the concentration of only one of reactants varies and that of the other is held fixed, we have the following transformations

$$\begin{aligned} c_1 &\longrightarrow c_1 + \delta c_1 \text{ with a modified rate } r(c_1 + \delta c_1, c_2) \\ c_2 &\longrightarrow c_2 + \delta c_2 \text{ with a modified rate } r(c_1, c_2 + \delta c_2) \end{aligned} \tag{7}$$

When both the concentrations $\{c_1, c_2\}$ simultaneously change to $\{c_1 + \delta c_1, c_2 + \delta c_2\}$, the rate $r(c_1, c_2)$ as in Equation (6) changes as

$$r \longrightarrow r(c_1 + \delta c_1, c_2 + \delta c_2) = r' \tag{8}$$

In the limit of $r \approx r'$, the chemical equilibrium is formed. That is, the equilibrium is formed at the fixed point of the rate $r(c_1, c_2)$ as in Equation (6). As per the fluctuation theory analysis [17–22], the local nature of the chemical equilibrium depends on the sign of the chemical concentration capacities, which are defined as the pure second derivatives of $r(c_1, c_2)$ with respect to $\{c_1, c_2\}$ respectively.

The corresponding global nature of the equilibrium is characterized by the sign of the determinant of fluctuation matrix of the rate $r(c_1, c_2)$. Before proceeding further, let us consider a first-order reaction with $m = 1$ and $n = 1$ as per the equilibrium

$$A + B \rightleftharpoons C + D \tag{9}$$

In general, the equilibrium between the reactants $A, B$ of their orders $\{m, n\}$ and $C, D$ of their orders $\{p, q\}$ is achieved when the rate of the forward reaction becomes same as that of the reverse reaction. As mentioned before, up to a constant factor, the rate of the forward reaction varies as the product of concentrations of the reactants as in Equation (5), viz. for two components $\{A, B\}$ we have the following power law

$$r_{dir} = k_{dir}[A]^m[B]^n, \tag{10}$$

where the constant factor $k_{dir}$ is termed as the rate constant of the forward reaction [13]. Similarly, let $k_{inv}$ be the rate constant of the backward reaction. Then, the corresponding rate modulates as per the product of concentrations of the products $\{C, D\}$ as

$$r_{inv} = k_{inv}[C]^p[D]^q, \tag{11}$$

where $[C]$ and $[D]$ are their respective concentrations. Thus, it is understood that the law of mass action arises as per the equality $r_{dir} = r_{inv}$. From the above equations, we find the equilibrium constant $K$ reads as the ratio of the rate constants of the forward reaction $r_{dir}$ to that of the backward reaction $r_{inv}$. Thus, in the light of chemical affinity [12], we have the following equilibrium constant

$$K = \frac{[C]^p[D]^q}{[A]^m[B]^n} \tag{12}$$

Having determined the fluctuation properties of the forward reaction about the equilibrium from Equation (12), we can also estimate that of the backward reactions, as well. Namely, for a given equilibrium constant $K$, our present investigation helps in understanding the nature of a chemical equilibrium formation as fluctuations over the law of mass action. Therefore, it is worth emphasizing that a chemical reaction never proceeds till its end, but it rather attains an equilibrium state [26], which exclusively depends upon the available number of reactants participating in the reaction [13]. It is important to note that a reaction in its equilibrium retains its dynamic characteristics; however, its forward and reverse directions eventually both possesses the same rate. This gives an impression of the termination of a chemical reaction. For example, such an equilibrium formation is supported by the following titration

$$NaOH + HCl \rightleftharpoons NaCl + H_2O \tag{13}$$

In this setup, a reaction can proceed in forward or backward direction depending upon external conditions and catalysts present in the reaction. Indeed, in the light of various physiochemical investigations [29], an equilibrium formation happens via the donation of a proton $H^+$, whose concentration $[H^+]$ defines the $pH$ values of the solution as

$$pH = -\ln[H^+] \tag{14}$$

Concerning the equilibrium formation, the $pH$ value plays an important role. Historically, the term $pH$ represents the potential of hydrogen which corresponds to a numerical value indicating the acidity or the basicity of a given aqueous solution. In short, the $pH$ value of a solution is defined as the negative logarithm of hydrogen ions concentration $[H^+]$ as in Equation (14). It is worth mentioning that the value of $pH$ ranges from 0 to 14 with the classification that its values less than 7 indicating an acidic

solution, greater than 7, as a basic solution, and equal to 7 as the neutral [13]. Indeed, for non-aqueous solutions, the $pH$ measurement is realized by a different scale than its aqueous counterparts as above in Equation (14), viz. the acidity functions, see [30]. Namely, the corresponding $pH$ of a solvent as the hydrogen ion activity depends on the chemical potential, state and the temperature governing the system.

Subsequently, $pH$ value emerges as an important conception in various studies including the chemical equilibria, acid-base pairs, titration reactions, donor-acceptor and strong base formation. Following the same, in Section 6, we provide the below statistical fundamentals behind the reaction mechanism and chemical equilibrium formation for various chemical reactions that pave path for industrial developments.

## 3. Chemical Equilibrium Formation

In this section, we commence by describing binary component chemical reactions and their equilibrium formation [30]. Here, by following the above-mentioned fluctuation theory perspective, we examine equilibrium formation for binary component chemical reactions, their associated flow components, capacities, and fluctuation quantities regarding the local and global chemical stabilities as below.

In this work, we mainly focus on the behavior of the above rate as in Equation (6) with respect to fluctuations of the concentrations $\{c_1, c_2\}$. To address the question how the reactants $\{A, B\}$ form an equilibrium, we need to determine an optimized rate $r(c_1, c_2)$ under infinitesimal variations of $\{c_1, c_2\}$. Before proceeding further, let us emphasize that we offer an equilibrium formation via an intrinsic perspective of the fluctuation theory.

### *3.1. Flow Components*

Given two reactants $\{A, B\}$ with their concentrations $\{c_1, c_2\}$, the associated rate $r(c_1, c_2)$ takes a power law of the form as in Equation (6). In this context, the $i$th flow component is defined as the first partial derivative of the chemical rate $r(c_i)$ with respect to the concentration $c_i$. Herewith, under fluctuations of $\{c_1, c_2\}$, we have the following flow components

$$r_1 = \frac{\partial r}{\partial c_1} = kmc_1^{m-1}c_2^n \tag{15}$$

with respect to $c_1$, and that of the other with respect to $c_2$ as

$$r_2 = \frac{\partial r}{\partial c_2} = knc_1^m c_2^{n-1} \tag{16}$$

Thus, it follows that an equilibrium—defined as the simultaneous roots of flows equations $r_1 = 0 = r_2$ as in Equations (15) and (16)—is formed when either one of the orders $\{m, n\}$ vanishes or one of the concentrations $\{c_1, c_2\}$ vanishes. More precisely, the reaction attains its steady state when we have either (i) $m = 0$ and $n = 0$ or (ii) $c_1 = 0$, or (iii) $c_2 = 0$.

### *3.2. Concentration Capacity*

As per the above fluctuation theory analysis [17–22], the chemical concentration capacity of the components $A$ takes the following power law form

$$r_{11} = \frac{\partial^2 r}{\partial c_1^2} = km(m-1)c_1^{m-2}c_2^n \tag{17}$$

For all non-zero concentrations $\{c_1, c_2\}$, we see that $r_{11}$ (representing the local stability of the chemical system with respect to fluctuations in the concentration of the component $A$) vanishes identically whenever we have either $m = 0$ or $m = 1$. Similarly, the chemical concentration capacity of the components $B$ simplifies as

$$r_{22} = \frac{\partial^2 r}{\partial c_2^2} = kn(n-1)c_1^m c_2^{n-2} \tag{18}$$

Herewith, for all non-zero concentrations $\{c_1, c_2\}$, $r_{22}$ (representing the local stability of the chemical system with respect to fluctuations in the concentration of the component $B$) vanishes whenever it is of the zero or unit orders, viz. $n = 0, 1$.

### *3.3. Concentration Correlation*

It follows that the correlation between the components $A$ and $B$ is given by

$$r_{12} = \frac{\partial^2 r}{\partial c_1 \partial c_2} = knmc_1^{m-1} c_2^{n-1} \tag{19}$$

Please note that $r_{12}$ signifying simultaneous fluctuations of the components $A$ and $B$ vanishes only when either one of them is of zeroth order at non-vanishing concentrations $\{c_1, c_2\}$. Thus, the corresponding rate $r(c_1, c_2)$ becomes independent of either $c_1$ or $c_2$.

### *3.4. Equilibrium Stability*

To study the stability of the equilibrium [17–22], let us define the fluctuation matrix as

$$H = \begin{bmatrix} r_{11} & r_{12} \\ r_{12} & r_{22} \end{bmatrix} \tag{20}$$

Thus, from the above evaluation of the chemical capacities $\{r_{11}, r_{22}\}$ as in Equations (17) and (18) and the associated correlation $r_{12}$ as in Equation (19), we have the following fluctuation matrix

$$H = kc_1^{m-2} c_2^{n-2} \begin{bmatrix} m(m-1)c_2^2 & mnc_1c_2 \\ mnc_1c_2 & n(n-1)c_1^2 \end{bmatrix} \tag{21}$$

Consequently, it is direct to see that the determinant $\Delta := r_{11}r_{22} - r_{12}^2$ of $H$ simplifies as

$$\Delta = k^2 mn(1-m-n)c_1^{2m-2} c_2^{2n-2} \tag{22}$$

Herewith, we see that the determinant $\Delta$ vanishes identically when one of the concentrations $(c_1, c_2)$ vanishes or one of the reactants is of the zero order or the sum of orders of the reactants is unity. In particular, it is worth mentioning that we have $\Delta = 0$ along the line $m + n = 1$. For example, such an equilibrium arises for the chemical reaction with an equal order of reactants $\{A, B\}$ with its rate $r = k\sqrt{c_1 c_2}$. Furthermore, from Equation (22), it follows that the determinant $\Delta$ is identically zero for all pair of reactants $\{A, B\}$ with their respective orders as $\{m, 1-m\}$.

#### 3.4.1. Local Stability

It is interesting to note that the local chemical equilibrium stability requires a positive value of either $m(m-1)$ or $n(n-1)$. This results into the condition that the orders $m$ and $n$ should either be negative or larger than unity. In other words, the system is locally unstable for an arbitrary pair of reactants $\{A, B\}$ with their orders $m, n \in (0, 1)$.

#### 3.4.2. Global Stability

From Equation (22), we see that the global stability of the chemical equilibrium requires the positivity of a cubic factor $mn(1-m-n)$ under variations of $\{m, n\}$. This happens for the orders $\{m, n\}$ such that (i) $1 > m + n$ with $m$ and $n$ having the same signatures, and (ii) $1 < m + n$ with $m$ and $n$ having the opposite signatures.

Furthermore, concerning the chemical fluctuation invariants, another interesting quantity is the trace $tr(H) := r_{11} + r_{22}$ of the fluctuation matrix $H$. From Equation (21), the concentrations $\{1/c_1, 1/c_2\}$ lie on a conic section whenever the ratio of the trace $tr(H)$ and the chemical rate $r(c_1, c_2)$ as in Equation (6) takes a constant value. In this case, it follows that $\{c_1, c_2\}$ satisfy

$$\frac{m(m-1)}{c_1^2} + \frac{n(n-1)}{c_2^2} = k_e, \tag{23}$$

where $k_e = tr(H)/kc_1^{-m}c_2^{-n}$. In the sequel, for various values of the orders $\{m, n\}$, we offer qualitative features of the fluctuations quantities $\{r, r_1, r_2, r_{11}, r_{22}, r_{12}, \Delta, tr(H)\}$ under variations of the concentrations $\{c_1, c_2\}$. Notice also that all the other fluctuation quantities vanish identically for a zeroth-order chemical reaction, except its rate $r(c_1, c_2)$. In the next section, the above fluctuations quantities are plotted for a set of typical orders $(m, n)$ as

$$\mathcal{C} := \{(-1,-1), (-1, 1/2), (-1, 2), (1/2, 1/2), (1/2, 2), (2, 2)\} \tag{24}$$

It is worth noticing that the set $\mathcal{C}$ includes all the types of possibilities concerning a stable chemical equilibrium formation for the reactants $\{A, B\}$.

## 4. Discussion of the Results

Below, for the above-mentioned typical orders $(m, n)$ as in Equation (24), we provide qualitative discussion of the fluctuation quantities. Namely, we highlight the qualitative features of the fluctuation theory analysis by varying the rate in the concentration plane of the reactants. As mentioned before, the concentrations are measured in mol/L and the corresponding rate $r(c_1, c_2)$ is measured in the unit of mol/L/s. With reference to the Figures 1–6, the $X$-axis and $Y$-axis denote the concentrations $c_1$ and $c_2$ respectively.

### *4.1. Chemical Reactions with Orders* $(-1, -1)$

For chemical reactions with the reactants $\{A, B\}$ of their respective orders as $m = -1$ and $n = -1$, we give qualitative behavior of the rate $r(c_1, c_2)$ in the Figure 1a. In this case, we see that $r$ has four peaks of fluctuations where the two them have a positive amplitude of the order 0.2, while the other two have a negative amplitude of the same order. Furthermore, for given concentration of the reactants, we observe that there are fluctuations solely along the limiting lines $c_2 \to 0$ and $c_1 \to 0$. As we approach the origin $(0, 0)$ in the concentration plane, the equilibrium is achieved as a long-term effect, i.e., $r$ takes a constant value.

From the Figure 1b, we find that the rate of change of $r_1(c_1, c_2)$ has a negative amplitude of the order $-0.1$ for a positive value of the concentration $c_2$ of the reactant $B$. However, for the other case $c_2 < 0$, we observe symmetrical fluctuations of the same order of the positive amplitude. Furthermore, we notice a satellite peak for decreasing concentration $c_2$ with an alternating spike while approaching the concentration axis $c_2 = 0$.

From Figure 1c, we see an analogous behavior of the rate of change of the flow component $r_1(c_1, c_2)$ with a right-angle rotation of the concentration of the reactants $\{A, B\}$. Interestingly, the amplitude of fluctuations of $r_1(c_1, c_2)$ remains the same and only the axes are being exchanged in the interval of $-50 < c_1, c_2 < 50$.

With the above observations of $\{r_1, r_2\}$, we notice from Figure 1d that the same number of four peaks of fluctuations in the capacity $r_{11}(c_1, c_2)$ occurs around the origin $(0, 0)$. On the other hand, for $c_1 \to 0$, a constant positive capacity $r_{11}$ is maintained along the negative $c_2$-axis. Furthermore, a constant negative capacity $r_{11}$ is followed along the positive $c_2$-axis.

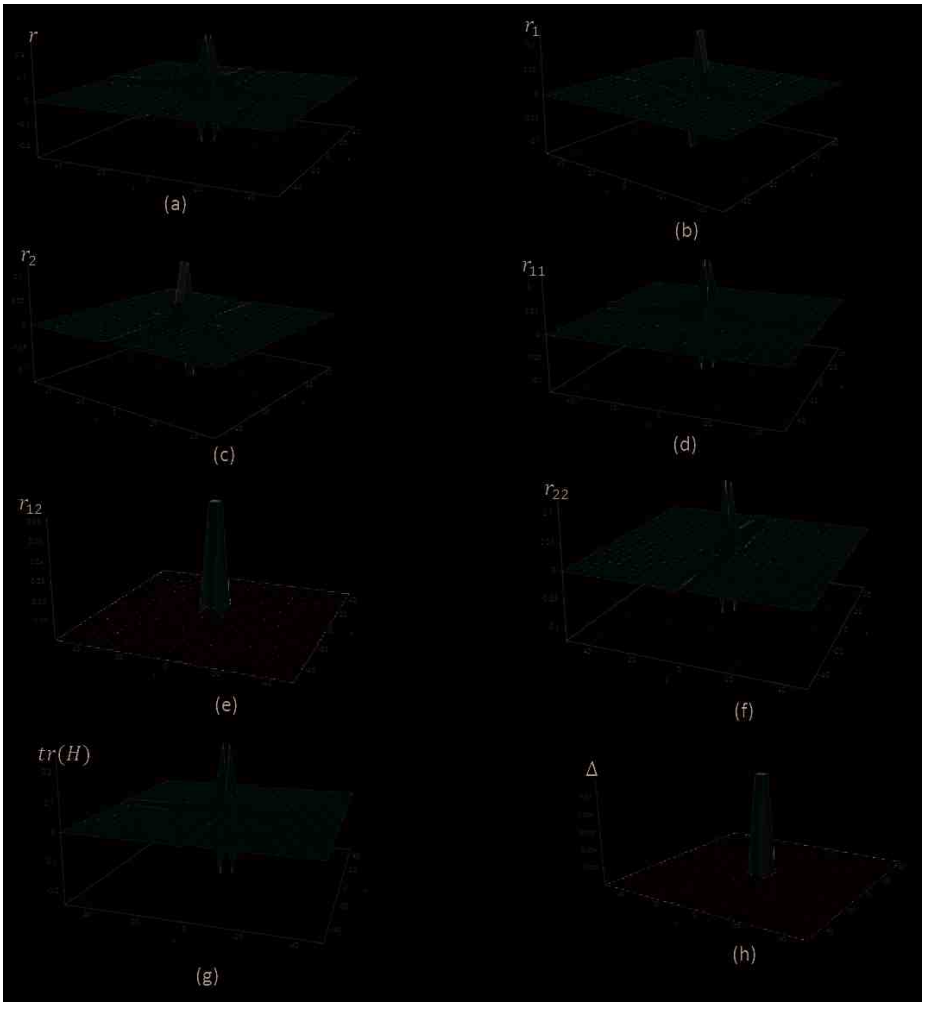


**Figure 1.** The fluctuation quantities as a function of the chemical concentrations $\{c_1, c_2\}$ for $m = -1$ and $n = -1$ plotted in the interval $-50 \leq c_1, c_2 \leq 50$ against (**a**) the rate $r(c_1, c_2)$, (**b**) flow $r_1(c_1, c_2)$, (**c**) flow $r_2(c_1, c_2)$, (**d**) capacity $r_{11}(c_1, c_2)$, (**e**) correlation $r_{12}(c_1, c_2)$, (**f**) capacity $r_{22}(c_1, c_2)$, (**g**) trace $tr(H)$ and (**h**) determinant $\Delta(c_1, c_2)$. (Note: with $c_1$, $c_2$ measured in mol/L on $X$ and $Y$ axis respectively, the other quantities on $Z$-axis are measured in the units as: $r \rightarrow$ mol/L/s; $r_1, r_2 \rightarrow \text{s}^{-1}$; $r_{11}, r_{12}, r_{22}, tr(H) \rightarrow \text{mol}^{-1}\ \text{L}\ \text{s}^{-1}$; $\Delta \rightarrow \text{mol}^{-2}\ \text{L}^2\ \text{s}^{-2}$).

From the above Figure 1e, it is evident that the cross-correlation $r_{12}(c_1, c_2)$ of the rate of the reaction takes a positive value for any $\{c_1, c_2\}$ with a maximum amplitude of 0.06. For a given pair of concentrations $\{c_1, c_2\}$, the cross-correlation $r_{12}$ increases steeply as we approach the origin $(0, 0)$ in the concentration plane. Interestingly, we find that the chemical equilibrium is uniformly maintained between $A$ and $B$ throughout the concentration plane, except the origin $(0, 0)$.

Figure 1f depicts the variation of the capacity $r_{22}(c_1, c_2)$ as a function of the concentrations $-50 < c_1, c_2 < 50$. It could be analyzed thus that there are symmetrical fluctuations in $r_{22}$ taking place around the origin $(0, 0)$ with a reduced amplitude in comparison to the rate $r$ as in Figure 1a. We see a pair of pulse-like oscillations in $r_{22}$ both in the positive and negative directions about the origin.

In addition, fluctuations along the $c_1$-axis are notably observed as $c_2 \to 0$. A uniform and constant capacity $r_{22}$ of a positive amplitude is maintained along the negative $c_1$-axis, whereas the capacity $r_{22}$ possesses a constant negative amplitude along the positive $c_1$-axis.

The above Figure 1g represents common characteristics at the origin as mentioned in the previous observations. Thus, we notice steady and equal oscillations in the value of the trace $tr(H)$ of the fluctuation matrix $H$ of the rate of the reaction. Similarly, a constant dip in $tr(H)$ is observed along the $c_1$ axis as $c_2 \to 0$. In contrast to the above, viz. as $x \to 0$, a constant positive trace is found along $c_2$ axis under fluctuations of $\{c_1, c_2\}$.

Figure 1h shows a similar behavior for the determinant $\Delta(c_1, c_2)$ of the fluctuation matrix of the chemical rate to the cross-correlation $r_{12}$ as depicted above in Figure 1e. It follows that $\Delta$ and $r_{12}$ both have positive amplitudes of fluctuations for any values of $\{c_1, c_2\}$. In contrast to the chemical correlation $r_{12}$, we find that $\Delta$ possesses a smaller amplitude of fluctuations with its maximum value of the order 0.01. For a given pair of concentrations $\{c_1, c_2\}$, it is observed that $\Delta$ equally increases steeply as $\{c_1, c_2\}$ approach the origin. Concerning the quest of a global stability, it follows that the equilibrium is uniformly maintained between the reactants $\{A, B\}$ as long as the concentrations $\{c_1, c_2\}$ take non-zero values.

### *4.2. Chemical Reactions with Orders* $(-1, \frac{1}{2})$

We depict below the characteristics of the chemical fluctuations in Figure 2 for various chemical concentrations $\{c_1, c_2\}$ of the reactants $A$ and $B$ of their order $m = -1$ and $n = 1/2$ respectively.

For $c_2 > 0$, there are fluctuations in the rate $r(c_1, c_2)$ for $m = -1$ and $n = 1/2$ for the reactants $A$ and $B$. Namely, from Figure 2a it follows that the rate has fluctuations with the maximum amplitude of 3 when $c_1$ approaches the origin from its small positive value. On the other hand, for $c_1$ approaching the origin from its small negative value, there is a dip in the rate with its maximum negative value $-3$. Furthermore, the fluctuations in $r(c_1, c_2)$ are asymmetric about the line $c_1 = 0$. In contrast to the above, the rate remains constant for $c_2 < 0$. The same observation holds for $c_2 > 0$ with a large positive or negative value of $c_1$.

From Figure 2b, along the concentration line $c_1 = 0$, we see that the flow component $r_1(c_1, c_2)$ has a valley as $c_2$ increases from the origin, which emerges symmetrically as we approach $c_1 = 0$ from its corresponding small positive and negative values. The amplitude of $r_1$ increases as we increase $c_2$, namely, we find that $r_1$ has the maximum amplitude of $-2.0$ at $c_2 = 50$ and it declines as $c_2$ reaches the origin. Furthermore, there are no fluctuations in $r_1$ for any value of $c_1$ with $c_2 < 0$. Also, $r_1$ remains constant far away from the region $c_1 = 0$ and $c_2 > 0$.

From the Figure 2c, it follows that the amplitude of $r_2(c_1, c_2)$ decreases as either $c_1$ or $c_2$ increases from the origin. There is a small positive damping uphill in $r_2$ with an amplitude 0.15 as we approach the concentration $c_2 = 0$ with an increasing value of $c_1 > 0$. Similarly, there is an uphill in $r_2$ in the region $c_1 = 0$ as $c_2$ approaches the origin from its positive values. In the region $c_1 < 0$ and $c_2 > 0$, we see that there is an asymmetric peak of the negative amplitude $-0.5$ as we approach the regions (i) $c_1 = 0$ for $c_2 > 0$ and (ii) $c_2 = 0$ for $c_1 < 0$. Furthermore, for all value of $c_1$, we notice that $r_2$ remains constant for $c_2 < 0$.

From the Figure 2d, it is observed that the capacity $r_{11}(c_1, c_2)$ has fluctuations for $c_2 > 0$, for species of $A$ and $B$ of the orders $m = -1$ and $n = 1/2$ respectively. In contrast to the rate of the reaction $r(c_1, c_2)$, the capacity has the maximum amplitude 1.5 when $c_1$ approaches the origin from its small positive values with $c_2 > 0$. When $c_1$ approaches the origin from its small negative values, we find a crest of negative amplitude $-1.5$. Moreover, we see that the capacity $r_{11}$ fluctuates asymmetrically about the region $c_1 = 0$ and $c_2 > 0$. In this case, we find that $r_{11}$ takes a small constant value for any $c_1$ with $c_2 < 0$. Furthermore, $r_{11}$ a small constant value for $c_2 > 0$ with a large value of $|c_1|$.

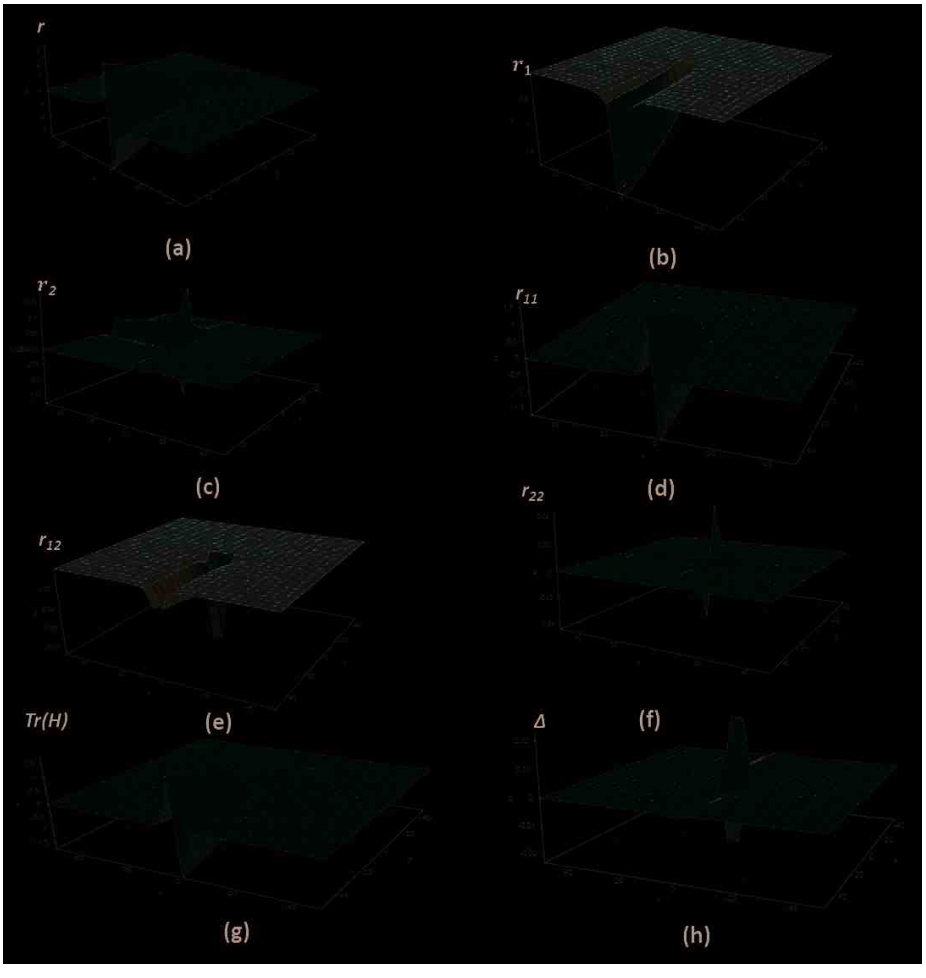


**Figure 2.** The fluctuation quantities as a function of the chemical concentrations $\{c_1, c_2\}$ for $m = -1$ and $n = \frac{1}{2}$ plotted in the interval $-50 \leq c_1, c_2 \leq 50$ against (**a**) the rate $r(c_1, c_2)$, (**b**) flow $r_1(c_1, c_2)$, (**c**) flow $r_2(c_1, c_2)$, (**d**) capacity $r_{11}(c_1, c_2)$, (**e**) correlation $r_{12}(c_1, c_2)$, (**f**) capacity $r_{22}(c_1, c_2)$, (**g**) trace $tr(H)$ and (**h**) determinant $\Delta(c_1, c_2)$. (Note: with $c_1$, $c_2$ measured in mol/L on $X$ and $Y$ axis respectively, the other quantities on $Z$-axis are measured in the units as: $r \to$ mol/L/s; $r_1, r_2 \to \text{s}^{-1}$; $r_{11}, r_{12}, r_{22}, tr(H) \to \text{mol}^{-1}\ \text{L}\ \text{s}^{-1}$; $\Delta \to \text{mol}^{-2}\ \text{L}^2\ \text{s}^{-2}$).

As depicted in Figure 2e, we find that there are no fluctuations in the correlation $r_{12}(c_1, c_2)$ for any value of $c_1$ with $c_2 < 0$. On the other hand, for all positive values of $c_2$, we notice a valley in the region $c_1 = 0$. At the origin, it follows that $r_{12}$ has a negative peak with the amplitude 0.08. Furthermore, there are small non-vanishing fluctuations in $r_{12}$ in the concentration region $c_2 = 0$ within the limit $-20 < c_1 < 20$. For all other values of $c_1$ and $c_2$, there are no fluctuations in the cross-correlation.

The capacity $r_{22}(c_1, c_2)$ is plotted in Figure 2f for various values of the concentrations $\{c_1, c_2\}$ with orders $m = -1$ and $n = 1/2$ of the reactants $A$ and $B$ respectively. In this case, we see that there are fluctuations of positive amplitude of the order 0.04 for small negative values of $c_1$ with a positive value of $c_2$. On the other hand, for $c_1 > 0$, we notice a downhill in $r_{22}$ along the concentration axis $c_2 = 0$. Furthermore, in the region $c_1 = 0$, there exists an uphill in the capacity $r_{22}$ as we approach the line $c_2 = 0$ from a positive value. In the region $c_1 < 0$ and $c_2 > 0$, we observe an asymmetric peak of

negative amplitude 0.04. In short, the capacity $r_{22}$ has fluctuations in the region (i) $c_1 = 0$ for $c_2 > 0$ and (ii) $c_2 = 0$ for $c_1 < 0$. Furthermore, it remains constant for all value of $c_1$ with concentration $c_2 < 0$.

In the above Figure 2g, we provide qualitative behavior of the trace $tr(c_1, c_2)$ of fluctuations of the reactants $\{A, B\}$ with their orders $m = -1$ and $n = 1/2$. Specifically, we find that $tr(H)$ takes a similar fluctuation property to that of the capacity $r_{11}$ with its maximum amplitude 1.5 when the concentration $c_1$ approaches the origin from a positive value of $c_2$. For $c_1$ approaching the origin from a negative value, the trace $tr(H)$ shows a negative value of the amplitude 1.5. In the region $c_2 > 0$, we observe that $tr$ has asymmetric fluctuations around $c_1 = 0$. For the orders $m = -1$ and $n = 1/2$, for various values of $c_1$, from the Figure 2g, it follows that $tr$ vanishes for all $c_2 < 0$. In this case, it is worth mentioning that $tr$ disappears for $c_2 > 0$ and $|c_1| > 20$.

The Figure 2h depicts qualitative feature of the determinant $\Delta(c_1, c_2)$ of the fluctuation matrix of the rate of reaction with orders $m = -1$ and $n = 1/2$. In this case, we observe that the reaction could become unstable only along $c_1 = 0$. In particular, for $c_2 > 0$, we see a negative value of the determinant $\Delta$. In the limit of $c_1 \to 0$ with $c_2 > 0$, we find the amplitude of $-0.02$ for $\Delta(c_1, c_2)$. For the negative value of $c_2$, we find a positive uphill in $\Delta$ along the line $c_1 = 0$ with its maximum amplitude of 0.02 around the origin. In the remaining part of the reaction plane, viz. for large values of $c_1$, we notice that $\Delta(c_1, c_2)$ vanishes identically for all values of $c_2$.

### *4.3. Chemical Reactions with Orders* $(-1, 2)$

In Figure 3a, we give qualitative behavior of the rate $r(c_1, c_2)$ for the orders $m = -1$ and $n = 2$ of the reactants $\{A, B\}$. We see that the rate $r$ possess an asymmetric nature about the line $c_1 = 0$ and has symmetric fluctuations about the concentration axis $c_2 = 0$. Namely, for a large positive $c_2$, the rate $r$ has a negative amplitude of the order 1000 when we approach the axis $c_1 = 0$ from its small negative values. On the other hand, for $c_2 > 0$, we observe a positive amplitude of the order 1000 for the rate $r$ while approaching $c_1 = 0$ from its positive values. Similarly, for $c_2 < 0$, it is observed that $r$ takes the same negative amplitude of 1000 while one approaches $c_1 = 0$ from its negative end. Indeed, as we approach $c_1 = 0$ from a negative value, the rate $r$ receives a positive value of 1000 for $c_2 < 0$. Furthermore, for all other values of $c_2$, there are no fluctuations in $r$ for a large $|c_1| > 20$.

For $m = -1$ and $n = 2$, the flow component $r_1(c_1, c_2)$ as plotted in Figure 3b shows that we have large negative fluctuations about the concentration axis $c_1 = 0$ for extreme positive and negative values of $c_2$. Namely, for $c_2 = \pm 50$, the rate $r_1$ takes a negative value of 600. Furthermore, the behavior of $r_1$ remains symmetric about the axes $c_1 = 0$ and $c_2 = 0$. Indeed, there are no fluctuations in $r_1$ far away from axis $c_1 = 0$.

The variations in the flow component $r_2(c_1, c_2)$ with chemical concentration $\{c_1, c_2\}$ at orders $-1$ and 2 of the reactants $A$ and $B$ are demonstrated in Figure 3c. The graph shows that $r_2$ gradually increases from its minimum value of $-40$ to its maximum value of 40 when $c_2$ varies from 50 to $-50$ while approaching $c_1 = 0$ from its negative values. When approaching $c_1 = 0$ from its positive values, $r_2$ decreases from its maximum value of 40 to its minimum $-40$ as $c_2$ decreases from $+50$ to $-50$. Consequently, we find a dual characteristic of $r_2$ along the axis $c_1 = 0$. Interestingly, we see that there are no fluctuations in $r_2$ for large absolute values of $c_1$.

In Figure 3d, we provide the local stability properties of a chemical system for the reactant $A$ and $B$ of their orders $m = -1$ and $n = 2$ respectively. In particular, we see that the capacity $r_{11}(c_1, c_2)$ is symmetric about the axis $c_2 = 0$. Namely, it follows that $r_{11}$ takes large negative value of the order 600 as we approach $c_1 = 0$ from its negative values. In contrast, $r_{11}$ receives a large positive amplitude of the order 600 as we approach $c_1 = 0$ from its positive values. Thus, we see a saddle behavior in $r_{11}$ along the axis $c_1 = 0$. As in the previous cases, there are no fluctuations in $r_{11}$ for $|c_1| > 20$.

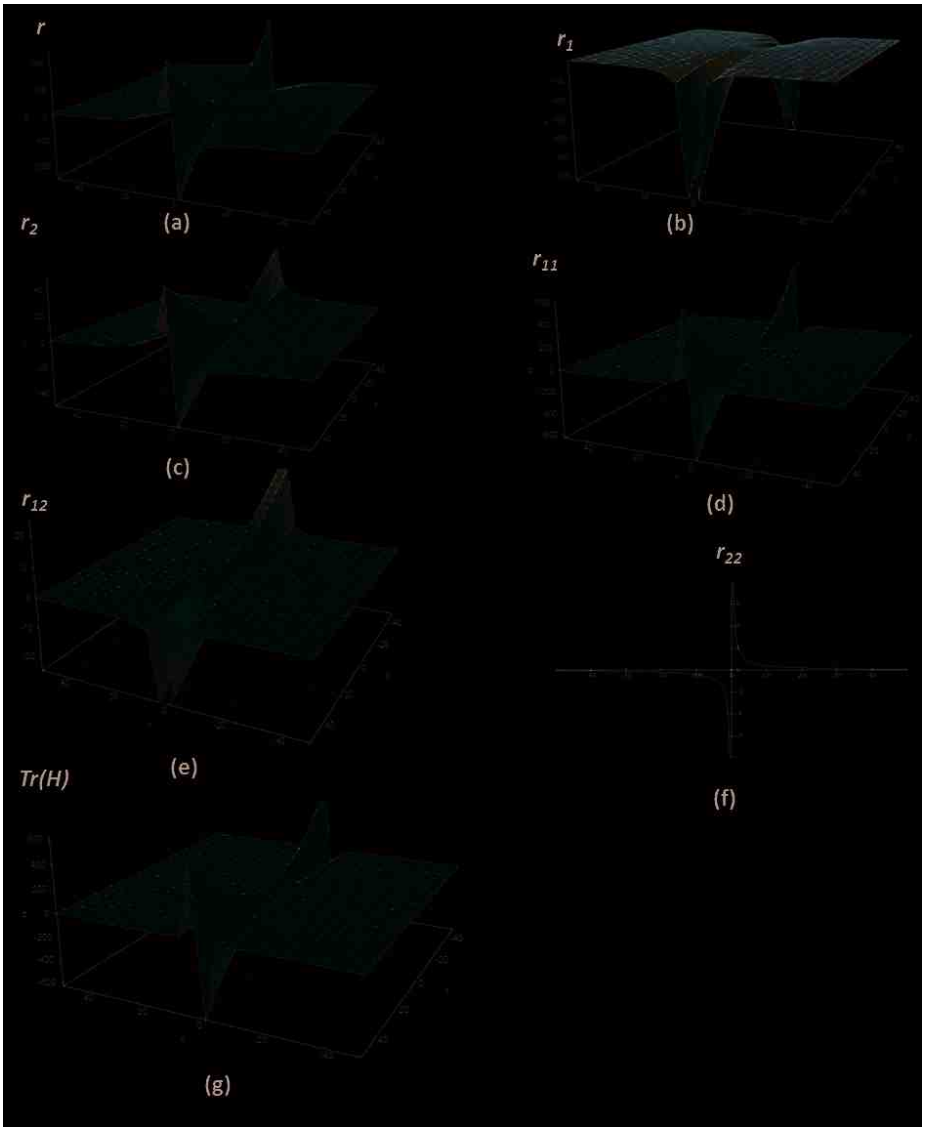


**Figure 3.** The fluctuation quantities as a function of the chemical concentrations $\{c_1, c_2\}$ for $m = -1$ and $n = 2$ plotted in the interval $-50 < c_1, c_2 < 50$ against (**a**) the rate $r(c_1, c_2)$, (**b**) flow $r_1(c_1, c_2)$, (**c**) flow $r_2(c_1, c_2)$, (**d**) capacity $r_{11}(c_1, c_2)$, (**e**) correlation $r_{12}(c_1, c_2)$, (**f**) capacity $r_{22}(c_1, c_2)$ and (**g**) trace $tr(H)$. (Note: with $c_1$, $c_2$ measured in mol/L on $X$ and $Y$ axis respectively, the other quantities on $Z$-axis are measured in the units as: $r \rightarrow$ mol/L/s; $r_1, r_2 \rightarrow \mathrm{s}^{-1}$; $r_{11}, r_{12}, r_{22}, tr(H) \rightarrow \mathrm{mol}^{-1}\ \mathrm{L}\ \mathrm{s}^{-1}$; $\Delta \rightarrow \mathrm{mol}^{-2}\ \mathrm{L}^2\ \mathrm{s}^{-2}$).

From the Figure 3e, we see that the cross-correlation $r_{12}(c_1, c_2)$ increases along the axis $c_1 = 0$ as the concentration $c_2$ decreases from 50 to $-50$. In particular, there is a negative peak of fluctuations of the order 20 in $r_{12}$ for large positive values of $c_2$ along the axis $c_1 = 0$. On the other hand, we find that $r_{12}$ has a positive amplitude of the order 20 for large negative values of $c_2$. Furthermore, we observe

symmetric fluctuations in $r_{12}$ along $c_1 = 0$ for all values of $c_2$. In this case, for all values of $c_2$, the cross-correlation $r_{12}$ vanishes identically for a large $|c_1| > 20$.

In Figure 3f, it is shown that the capacity $r_{22}(c_1, c_2)$ becomes independent of $c_2$, and therefore it displays a rectangular hyperbolic behavior with $c_1$, viz. we have $c_1 r_{22}(c_1, c_2) = 2$. Herewith, the capacity $r_{22}$ increases indefinitely as $c_1$ approaches the origin from its positive values. Similarly, it tends to a large negative value while $c_1$ approaches the origin from its negative values. Namely, the reaction happens only for positive value of $c_1$, whereby its intensity decreases as $c_1$ increases further. Physically, we see that the chemical system is not stable in initial stages of the reaction.

From Figure 3g, we find that trace $tr(c_1, c_2)$ possess a symmetric behavior about the line $c_2 = 0$ for the orders $m = -1$ and $n = 2$ of the reactants $A$ and $B$ respectively. In this case, it is observed that the trace $tr$ has a large negative peak of the amplitude 600 as we approach the axis $c_1 = 0$ from its negative values. On the other hand, we observe that $tr(H)$ takes a positive value of the order 600 while approaching $c_1 = 0$ from its positive values. As in the case of $r_{11}$, it follows that $tr(H)$ has a saddle point behavior along the concentration axis $c_1 = 0$. Furthermore, it is worth mentioning that $tr(H)$ differs from the capacity $r_{11}$ largely in the limit of small values of $c_1$. It is observed for $m = -1$ and $n = 2$ that $tr(H)$ of the fluctuation matrix $H$ vanishes for $|c_1| > 20$.

### *4.4. Chemical Reactions with Orders* $(\frac{1}{2}, \frac{1}{2})$

The Figure 4 represent the fluctuation quantities as a function of the chemical concentrations $\{c_1, c_2\}$ for $m = \frac{1}{2}$ and $n = \frac{1}{2}$ of the reactants $\{A, B\}$ plotted in the interval $-50 < c_1, c_2 < 50$. Namely, from Figure 4a, we see that the rate $r(c_1, c_2)$ shoots up as both the active chemical concentrations $\{c_1, c_2\}$ increase. On the other hand, it remains constant for both an increasing value of $c_1$ and decreasing $c_2$, or vice-versa. Moreover, it follows that $r$ falls off for decreasing values of $\{c_1, c_2\}$.

The flow component $r_1(c_1, c_2)$ as the rate of change of the $r(c_1, c_2)$ with respect to $c_1$ as shown in Figure 4b increases in the second quadrant as $c_1$ decrease from 50 to 0 and $c_2$ increases from 0 to 50. The same behavior of $r_1$ is found in the fourth quadrant when $c_1$ increases from $-50$ to 0 and $c_2$ decreases from 0 to $-50$. In the limit of $c_1 \to 0$, two extreme values of the amplitude 2.5 of $r_1$ are achieved as $c_2$ takes it maximum and minimum values. However, in the first and third quadrants, we notice no fluctuations in $r_1$ under variations of $\{c_1, c_2\}$.

From Figure 4c, we find that the flow component $r_2(c_1, c_2)$ shows an inverse behavior of the component $r_1(c_1, c_2)$ as depicted in Figure 4b. Specifically, it follows that $r_2$ increases when we have either an increasing $c_1 \in (0, 50)$ and decreasing $c_2 \in (0, 50)$, or an increasing $c_2 \in (-50, 0)$ and decreasing $c_1 \in (0, -50)$. In this case, an extreme value of $r_2 = 2.5$ is found for the maximum and minimum values of $c_1$ in the limit $c_2 \to 0$. Moreover, there are no changes in $r_2$ whenever $c_1$ and $c_2$ have contrasting variations.

From the above Figure 4d, it is interesting to note that the capacity $r_{11}(c_1, c_2)$ decreases in the first quadrant to its minimum value $-0.6$ as $c_2$ approaches to the origin from its small positive values along the axis $c_1 = 0$. Also, $r_{11}$ increases to its maximum value 0.60 in 3rd quadrant along $c_1 = 0$ when $c_2$ approaches the origin from its small negative values. In the intermediate quadrants 2 and 4, we observe that $r_{11}$ remain constant with a vanishingly small negative value.

As $c_1$ and $c_2$ decrease in the first quadrant, from Figure 4e, we see that the cross-correlation $r_{12}(c_1, c_2)$ increases to its maximum value of 0.1 in the absence of the reactants. Furthermore, we find that $r_{12}$ attains its minimum value of $-0.1$ as $(c_1, c_2)$ approaches the origin from their small negative values. It is noteworthy that the behavior of $r_{12}$ in 3rd quadrant is asymmetrical in its nature to that of the 1st quadrant. In this representation, there is no cross-correlation $r_{12}$ in the 2nd and 4th quadrants, i.e., when $(c_1, c_2)$ take their values with an opposite signature.

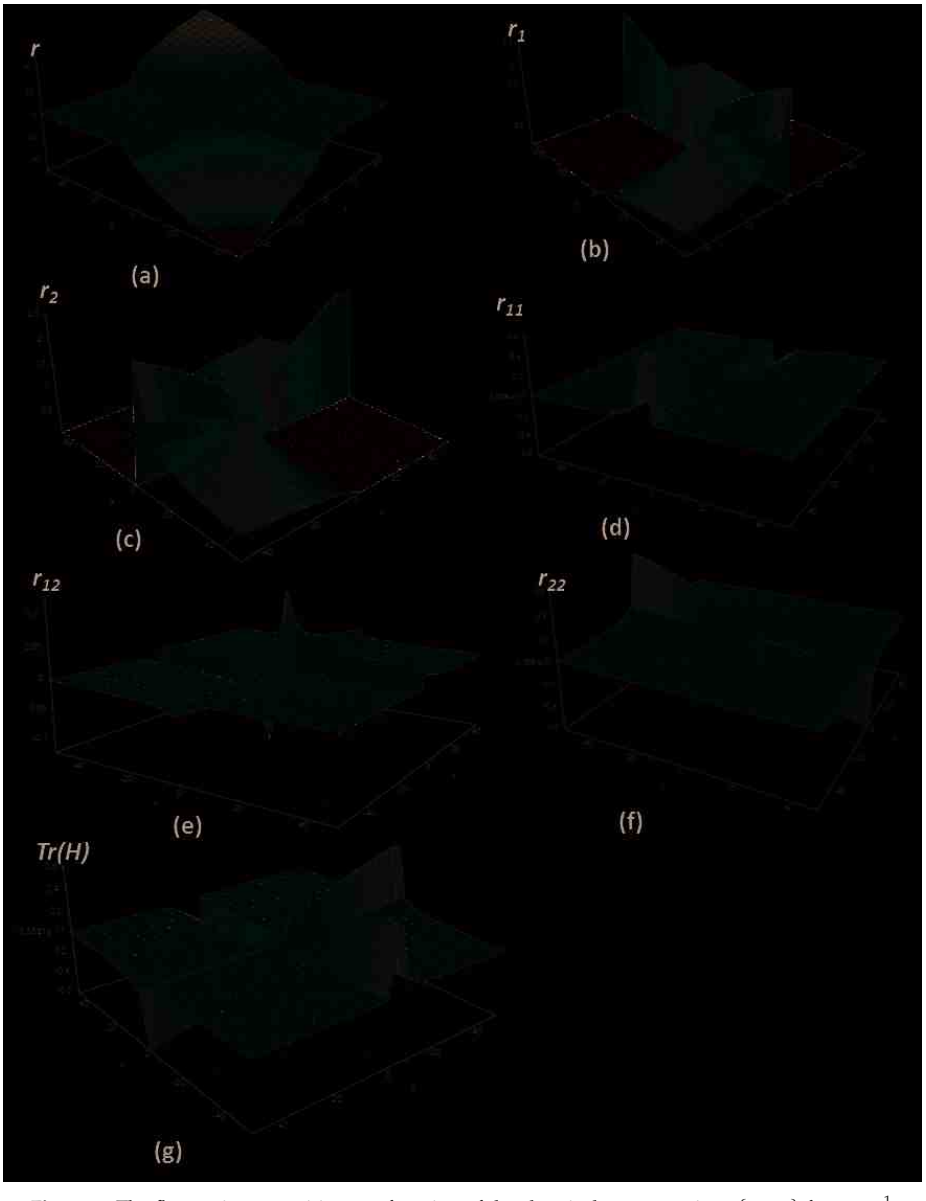


**Figure 4.** The fluctuation quantities as a function of the chemical concentrations $\{c_1, c_2\}$ for $m = \frac{1}{2}$ and $n = \frac{1}{2}$ plotted in the interval $-50 < c_1, c_2 < 50$ against (**a**) the rate $r(c_1, c_2)$, (**b**) flow $r_1(c_1, c_2)$, (**c**) flow $r_2(c_1, c_2)$, (**d**) capacity $r_{11}(c_1, c_2)$, (**e**) correlation $r_{12}(c_1, c_2)$, (**f**) capacity $r_{22}(c_1, c_2)$, and (**g**) trace $tr(H)$. (Note: with $c_1$, $c_2$ measured in mol/L on $X$ and $Y$ axis respectively, the other quantities on $Z$-axis are measured in the units as: $r \rightarrow$ mol/L/s; $r_1, r_2 \rightarrow \text{s}^{-1}$; $r_{11}, r_{12}, r_{22}, tr(H) \rightarrow \text{mol}^{-1}\ \text{L}\ \text{s}^{-1}$; $\Delta \rightarrow \text{mol}^{-2}\ \text{L}^2\ \text{s}^{-2}$).

Figure 4f provides a qualitative behavior of the capacity $r_{22}(c_1, c_2)$. Here, we find that it decreases in the first quadrant to its minimum value of $-0.6$ as $c_1$ approaches to its extreme value along the $c_2 = 0$. As observed in the case of the capacity $r_{11}(c_1, c_2)$, in this case we notice that $r_{22}$ takes its

maximum value 0.6 in 3rd quadrant along the axis $c_2 = 0$ when $c_1$ decreases from the origin to its large negative values. In this case, we also see that $r_{22}$ takes a small negative value in 2nd and 4th quadrants of the concentration plane.

From Figure 4g, the trace $tr(c_1, c_2)$ increases for decreasing value of $c_1$ for $c_2 = 0$ and it again increase for decreasing values of $c_2$ along the axis $c_1 = 0$. Similarly, in the 3rd quadrant, along the axis $c_1 = 0$, it decreases for increasing values of $c_2$. Furthermore, it decreases along the line $c_2 = 0$ for increasing values of $c_1$. Interestingly, the amplitude of the maximum and minimum values of the *tr* takes a constant value of 0.6. In the 2nd and 4th quadrants, there are no fluctuations in the *tr* for all non-zero values of $c_1$ and $c_2$.

### *4.5. Chemical Reactions with Orders* $(\frac{1}{2}, 2)$

In Figure 5a, it is demonstrated that the rate $r(c_1, c_2)$ varies largely for the concentration $c_1 > 0$ away from the axis $c_2 = 0$ for the orders $m = \frac{1}{2}$ and $n = 2$ of the reactants $A$ and $B$ respectively. Namely, as we move away from line $c_2 = 0$, it shows a parabolic behavior for a large $c_1$ with an amplitude of the order 2000. For a small $c_1$, the rate $r$ also shows a semi-parabolic behavior as a function of non-vanishing $c_2$ about the axis $c_1 = 0$. On the other hand, there are no real fluctuations in $r$ for a negative value of $c_1$. Indeed, it follows that $r$ has a symmetric behavior about the line $c_2 = 0$.

In the above Figure 5b, we depict qualitative behavior of the flow component $r_1(c_1, c_2)$ for the order $m = \frac{1}{2}$ and $n = 2$ of the reactants $\{A, B\}$. For large positive or negative values of $c_2$, we find that $r_1$ has a large amplitude of the order 800 about the axis $c_1 = 0$. Notice further that it has a symmetrical behavior along $c_2 = 0$, namely, it is a parabolic function of $c_2$ for a given value of $c_1$. At a large absolute value of $c_2$, it follows that $r_1$ attains a minimum value of 200 as $c_1$ reaches to its extreme positive and negative values. For all values of $c_2$, there are no real fluctuations in $r_1$ for $c_1 < 0$. Furthermore, as we augment the absolute value of the concentration $c_2$, the intensity of $r_1$ increases at any given $c_1 > 0$.

From Figure 5c, we find that the flow component $r_2(c_1, c_2)$ decreases as $c_2$ decreases in the interval $(-50, 50)$ while $c_1$ increases in the interval $(0, 50)$. For a large positive value of $c_1$, the amplitude of $r_2$ takes a maximum value of 600 at $c_2 = 50$, while it takes a minimum value of $-600$ at $c_2 = -50$. For a large positive $c_2$, it worth noticing that $r_2$ displays a semi-parabolic behavior along the line $c_2 = 50$ with a positive $c_1$. However, for all $c_1 > 0$, we have an oppositely vertex parabola along the line $c_2 = -50$. In this case, as a real valued function, $r_2$ remains constant for all negative values of $c_1$.

The variations of capacity $r_{11}(c_1, c_2)$ with various concentrations $\{c_1, c_2\}$ are plotted in Figure 5d for orders $1/2$ and 2 of the reactants $A$ and $B$ respectively. In this case, we see that $r_{11}$ has a symmetric behavior about the line $c_2 = 0$. For the extreme values of $c_2$, $r_{11}$ takes a large negative amplitude of the order 200. Furthermore, it follows that $r_{11}$ vanishes identically along the line $c_2 = 0$ for any values of $c_1$. Moreover, for all values of $c_2$, there are no fluctuations in $r_1$ far away from the concentration axis $c_1 = 0$.

For given orders of $m = 1/2$ and $n = 2$ of the reactants $A$ and $B$, the cross-correlation $r_{12}(c_1, c_2)$ of the chemical rate $r(c_1, c_2)$ is depicted in Figure 5e as a function of the concentrations $c_1$ and $c_2$. Thus, for all $c_1$, we see that $r_{12}$ vanishes identically along the axis $c_2 = 0$. For $c_2 < 0$, we find that $r_{12}$ takes negative values with its amplitude of the order 30 as $c_1$ approaches zero from its positive values. On the other hand, we observe a sudden fall in $r_{12}$ for $c_1, c_2 < 0$. Similarly, in the region $c_2 > 0$, we notice a positive peak of the amplitude 30 in $r_{12}$. Interestingly, we see an amplitude of the order 20 corresponding to the sub-leading fluctuations in $r_{12}(x, y)$. Indeed, from Figure 5e, it is evident that there are no cross correlations far away from the axis $c_1 = 0$.

The capacity $r_{22}(c_1, c_2)$ plotted in Figure 5f for the products $A$ and $B$ of their orders $m = 1/2$ and $n = 2$. Thus, we see that $r_{22}$ solely depends on $c_1$. Here, we have a parabola with its vertex at $c_1 = 0$. As $c_1$ increases, we see that $r_{22}$ indefinitely increases as well. It is clear that there are no possibilities of the occurrence of such a reaction for the concentration $c_1 < 0$ at this order.

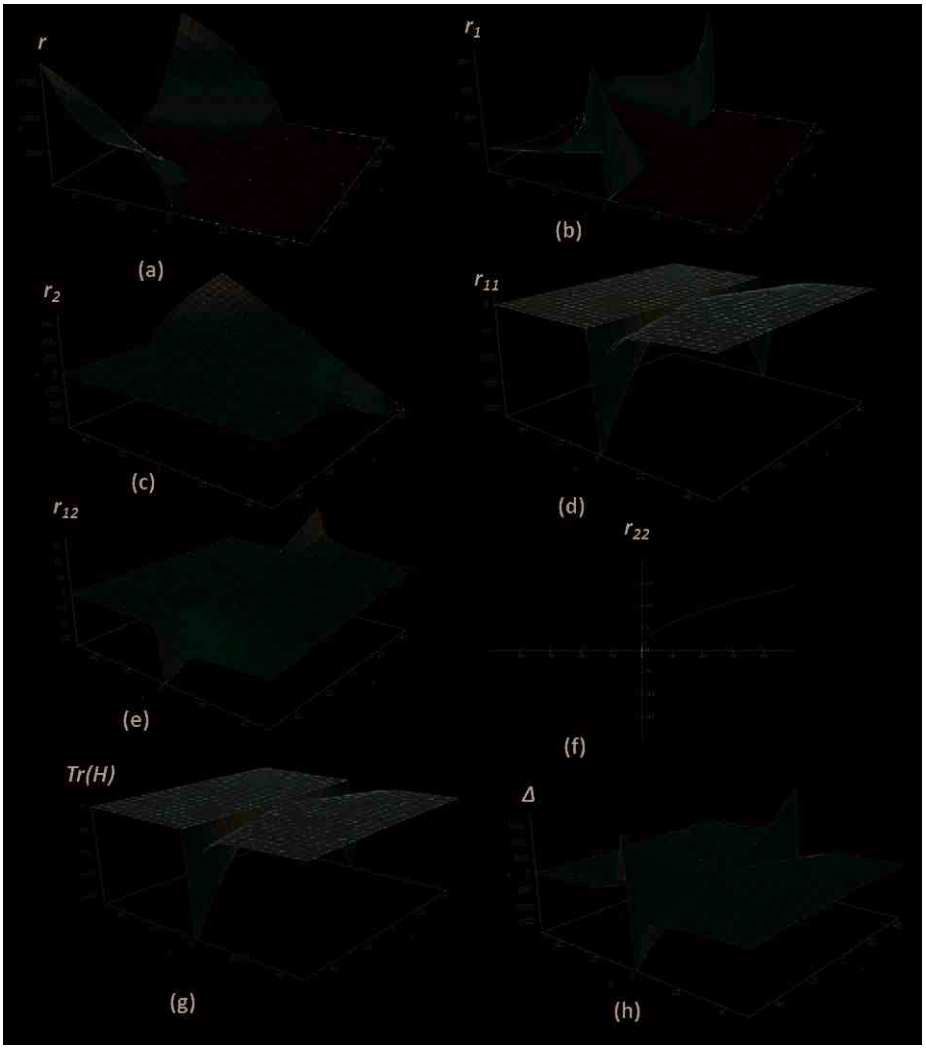


**Figure 5.** The fluctuation quantities as a function of the chemical concentrations $\{c_1, c_2\}$ for $m = \frac{1}{2}$ and $n = 2$ plotted in the interval $-50 < c_1, c_2 < 50$ against (**a**) the rate $r(c_1, c_2)$, (**b**) flow $r_1(c_1, c_2)$, (**c**) flow $r_2(c_1, c_2)$, (**d**) capacity $r_{11}(c_1, c_2)$, (**e**) correlation $r_{12}(c_1, c_2)$, (**f**) capacity $r_{22}(c_1, c_2)$, (**g**) trace $tr(H)$ and (**h**) determinant $\Delta(c_1, c_2)$. (Note: with $c_1$, $c_2$ measured in mol/L on $X$ and $Y$ axis respectively, the other quantities on $Z$-axis are measured in the units as: $r \rightarrow$ mol/L/s; $r_1, r_2 \rightarrow \mathrm{s}^{-1}$; $r_{11}, r_{12}, r_{22}, tr(H) \rightarrow \mathrm{mol}^{-1}\ \mathrm{L}\ \mathrm{s}^{-1}$; $\Delta \rightarrow \mathrm{mol}^{-2}\ \mathrm{L}^2\ \mathrm{s}^{-2}$).

Figure 5g provides a qualitative behavior of the trace $tr(c_1, c_2)$ of the fluctuation matrix $H$ for orders $m = 1/2$ and $n = 2$ of the species as a function of $\{c_1, c_2\}$. The trace appears to possess a similar qualitative behavior to the capacity $r_{11}$. Along the axis $c_1 = 0$, it has fluctuations of a negative amplitude of the order 200 for large positive and negative values of $c_2$. For the all values of $c_1$, $tr(H)$ has a symmetric behavior along the line $c_2 = 0$. There are no real fluctuations in $tr(H)$ for $c_1 < 0$. For all value of $c_2$ as $c_1$ increases, the trace $tr(H)$ increase from its large negative value to the order 200. Finally, it follows that $tr(H)$ vanishes asymptotically as $c_1$ takes a large value.

In Figure 5h, we depict the characteristic feature of the determinant $\Delta(c_1, c_2)$ of the fluctuation matrix with the orders $m = 1/2$ and $n = 2$. As a function of the concentrations $\{c_1, c_2\}$, we see that $\Delta$ takes a large positive amplitude of the order 1500 as we approach the axis $c_2 = 0$ from its negative values. For $c_1 > 0$, we observe a large negative amplitude of the order 1500 in $\Delta$ along $c_1 = 0$. Furthermore, for all values of $c_1$, we find that $\Delta$ remains symmetric along the line $c_2 = 0$. Notice further that at a given value of $c_1 < 0$, the amplitude of $\Delta$ increases as we increase the value of $|c_2|$. In contrast to above, for all values of $c_1 > 0$, it follows that $\Delta$ decreases as we increase $|c_2|$. In addition, for all values of $c_2$, the fluctuations in $\Delta$ of a given chemical reaction remains constant for all concentrations $\{c_1, c_2\}$ far away from the axis $c_1 = 0$.

### *4.6. Chemical Reactions with Orders* $(2, 2)$

The rate $r$ of the chemical reaction of reactants $A$ and $B$ of their orders $m = 2$ and $n = 2$ is shown in Figure 6a over the concentrations $\{c_1, c_2\}$ in the rang $(-50, 50)$. In this case, we find an increasing value of $r$ of the order $6 \times 10^6$ as $c_1$ and $c_2$ increase to large positive or negative values. We find that it remains symmetric about both axes $c_1 = 0$ and $c_2 = 0$ with its vanishing amplitude at the point $(0, 0)$. For a given value of $c_1$ or $c_2$, the rate $r$ emerges as parabola in either $c_1$ or $c_2$ respectively.

In Figure 6b, we demonstrate qualitative behavior of the flow component $r_1(c_1, c_2)$ as a function of the concentrations $\{c_1, c_2\}$ for the given chemical reaction with the reactants of the order 2. In particular, for a given non-zero $c_1$, we find a parabolic behavior of $r_1$ as a function of $c_2$. For a large $c_2$, we observe respective positive and negative amplitudes of fluctuations of their orders $2 \times 10^5$ in $r_1$ for large positive and negative values of $c_1$. For all $c_1 \neq 0$, it follows from Figure 6b that the fluctuations in $r_1$ remain symmetric along the axis $c_2 = 0$.

The characteristic behavior of the component $r_2(c_1, c_2)$ is shown in Figure 6c with respect to $\{c_1, c_2\}$ for the reacting species of the order 2. For all values of $c_2$, we notice that $r_2$ has a symmetric behavior along the axis $c_1 = 0$. The maximum amplitude of $r_2$ is found to be of the order $2.5^5$ as $c_1$ tends to its extreme values $\pm 50$ for the value of $c_2 = 50$. Similarly, its minimum value of the order $-2.5^5$ is achieved at the concentration line $c_2 = -50$. Given any value of $c_1$, it follows that $r_2$ has positive valued fluctuations for $c_2 > 0$ and negative valued fluctuations for $c_2 < 0$.

Figure 6d represent the capacity $r_{11}(c_1, c_2)$ of the reaction with products $\{A, B\}$ of their orders 2. This condition illustrates parabolic variations as the capacity $r_{11}(c_1, c_2) = 2c_2^2$ remain symmetric about the concentration $c_2 = 0$.

The variation of the cross-correlation $r_{12}(c_1, c_2)$ with respect to the concentrations $\{c_1, c_2\}$ of the species $\{A, B\}$ having orders 2 is shown in Figure 6e. In this case, we observe that $r_{12}$ attained a maximum value of the order $10^4$ for large positive values of $\{c_1, c_2\}$ and a minimum value of the order $-10^4$ for a large positive $c_1$ and negative $c_2$, and vice-versa. Moreover, from Figure 6e, it follows that $r_{12}$ has no variations when either $c_1$ or $c_2$ vanishes.

The capacity $r_{22}(c_1, c_2)$ of the products of their orders 2 as a function of the concentrations $\{c_1, c_2\}$ is equally represented by Figure 6d. Namely, the variations in $r_{22}$ are similar to the capacity $r_{11}(c_1, c_2)$ with a replacement of $c_2$ to $c_1$. Thus, we find parabolic variations in the capacity $r_{22}$ with respect to the concentration $c_1$, viz. we have a symmetric capacity $r_{22} = 2c_1^2$. In this case, it follows that $r_{22}$ vanishes identically in the limit of $c_1 = 0$.

Figure 6f represents the qualitative nature of the trace $tr(c_1, c_2)$ over the concentrations $c_1$ and $c_2$ of species of the orders 2. Herewith, we observed that $tr(c_1, c_2)$ takes a maximum positive amplitude of the order $10^4$ for large positive or negative values of $\{c_1, c_2\}$. As a matter of the fact, there are no fluctuations in the $tr(H)$ in the limit of either $c_1 = 0$ or $c_2 = 0$. Furthermore, at a fixed value of $c_1$ or $c_2$, it follows that $tr(H)$ arises as a shifted parabola in $c_2$ or $c_1$ respectively.

In Figure 6g, we depict the determinant $\Delta(c_1, c_2)$ of fluctuations in the rate of the happening of the chemical reaction with products $\{A, B\}$ of their order 2. For given values of $\{c_1, c_2\}$, we find that $\Delta$ arises as an inverted image of the rate $r(c_1, c_2)$ with different values of its amplitude of fluctuations. Namely, as $c_1$ and $c_2$ take large positive or negative values, we notice that $\Delta$ takes a large negative

amplitude of the order $7 \times 10^7$. Thus, there are no fluctuations in $\Delta$ when either of the concentration $c_1$ or $c_2$ vanishes. Finally, from Figure 6g, it follows that $\Delta$ remains symmetric about both the concentration axes $c_1 = 0$ and $c_2 = 0$.

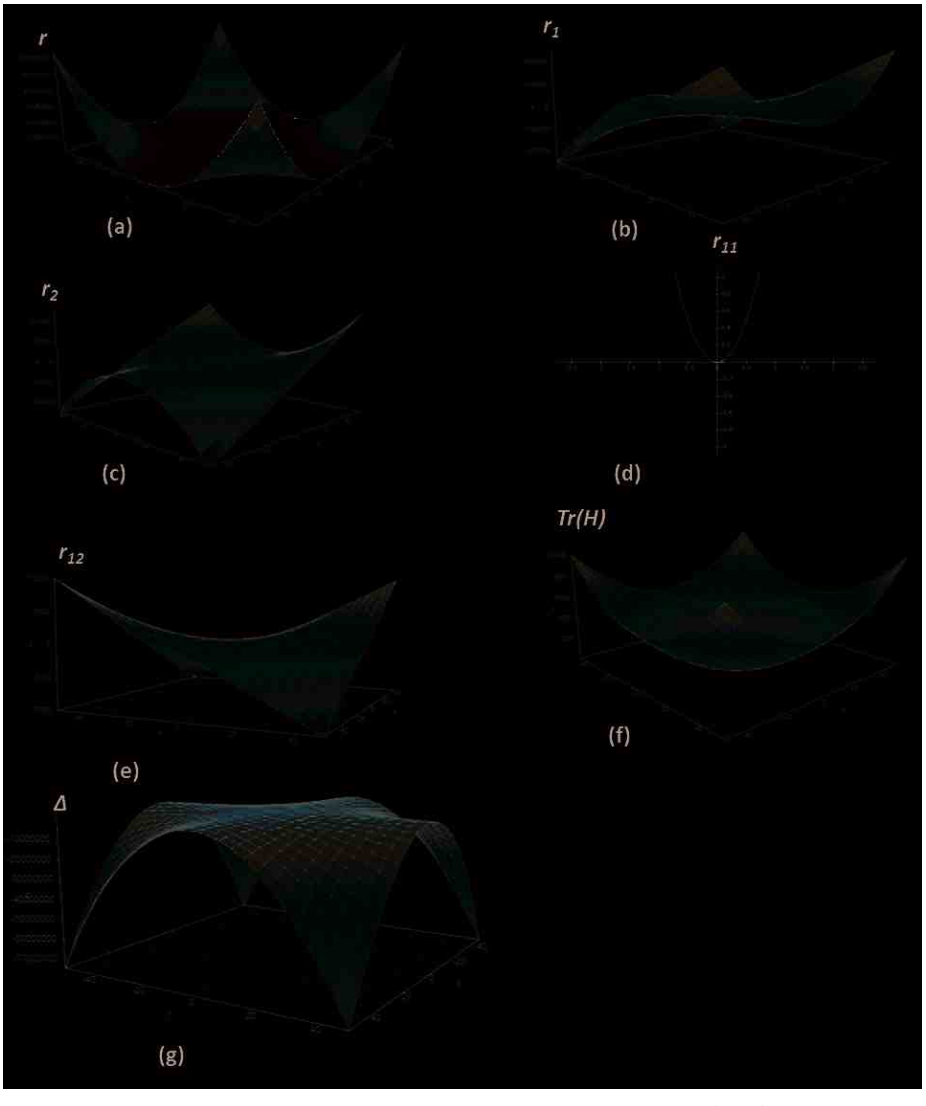


**Figure 6.** The fluctuation quantities as a function of the chemical concentrations $\{c_1, c_2\}$ for $m = 2$ and $n = 2$ plotted in the interval $-50 < c_1, c_2 < 50$ against (**a**) the rate $r(c_1, c_2)$, (**b**) flow $r_1(c_1, c_2)$, (**c**) flow $r_2(c_1, c_2)$, (**d**) capacity $r_{11}(c_1, c_2)$ (remains the same for the capacity $r_{22}(c_1, c_2)$ with the replacement of $c_1$ by $c_2$, (**e**) correlation $r_{12}(c_1, c_2)$, (**f**) trace $tr(H)$ and (**g**) determinant $\Delta(c_1, c_2)$. (Note: with $c_1$, $c_2$ measured in mol/L on $X$ and $Y$ axis respectively, the other quantities on $Z$-axis are measured in the units as: $r \to$ mol/L/s; $r_1, r_2 \to \text{s}^{-1}$; $r_{11}, r_{12}, r_{22}, tr(H) \to \text{mol}^{-1}\ \text{L}\ \text{s}^{-1}$; $\Delta \to \text{mol}^{-2}\ \text{L}^2\ \text{s}^{-2}$).

## 5. Verification of the Model

In this section, following the fact that the rate of a reaction offers valuable guidelines in modeling chemical interactions [23], we provide fluctuation theory analysis of equilibrium formation under variations of the rate and order of reactants. Namely, given an arbitrary chemical rate $r$, we discuss equilibrium formation as the function of the concentrations $\{c_1, c_2\}$ and partial orders $\{m, n\}$ of the reactants $\{A, B\}$ respectively. The formation of the chemical equilibrium can be represented as

$$\begin{array}{ccc} A + B & \rightleftharpoons & \text{Products} \\ c_1 \;\; c_2 & & \\ m \;\; n & & \end{array} \tag{25}$$

As per the analysis as in the previous section, for any positive concentrations $c_1$ and $c_2$ of the reactants $A$ and $B$, we see that the stability of the equilibrium largely depends on the partial orders $m$ and $n$. Namely, we find that the determinant $\Delta$ takes a positive value for all $m$ and $n$ satisfying $mn(1-m-n) > 0$. Similarly, for all $m$ and $n$, the capacity $r_{11}$ takes a positive value wherever we have $m(m-1) > 0$. In this concern, a comparative analysis of the equilibrium with the reaction rate $r$ with respect to variations of the orders $m$ and $n$ is summarized in the Table 1.

**Table 1.** A comparative analysis of the stability of the equilibrium as a function of the rate $r$ with respect to the orders $m$ and $n$ of the reactants.

| SN | $m$ | $n$ | $\mathbb{O} = m + n$ | $\Delta$ | $r_{11}$ |
|---|---|---|---|---|---|
| 1 | 0 | 0 | 0 | 0 | 0 |
| 2 | 1 | 0 | 1 | 0 | 0 |
| 3 | 0 | 1 | 0 | 0 | 0 |
| 4 | 1 | 1 | 2 | - | - |
| 5 | 1 | 2 | 3 | - | - |
| 6 | 2 | 1 | 3 | - | - |
| 7 | 2 | 2 | 4 | - | - |
| ⋮ | ⋮ | ⋮ | ⋮ | ⋮ | ⋮ |

In Table 1, $\mathbb{O}$ is the overall order of the reaction. Thus, for $\Delta > 0$, we find that a stable equilibrium is formed when we have either $r_{11}$ or $r_{22}$ is positive. The equilibrium will be unstable when the rate reaches its maximum, i.e., we have either $r_{11}$ or $r_{22}$ is negative. On the other hand, we need a refined analysis when either $r_{11}$ or $r_{22}$ vanishes identically. As per our analysis, a new matter will be formed when we have $\Delta < 0$. In the case, when $m$ and $n$ are even, the factor $c_1^{2m-2}c_2^{2n-2}$ of $\Delta$ does not change its sign. Therefore, when the total order $m + n < 1$, the reaction capacity $r_{11}$ is positive if we have either $m < 0$ or $m > 1$. However, we anticipate an improved analysis for the either of the partial orders $m, n = 0, 1$ of the reactants $A$ and $B$. It is worth emphasizing that the sign of $\Delta$ depends only on the orders of $A$ and $B$. For the zeroth-order reaction, i.e., $m + n = 0$ the sign of $\Delta$ varies as the product of $m$ and $n$. Further when either of the reactants $A$ or $B$ has order zero, it follows that the determinant $\Delta$ vanishes identically. Similarly, for the first-order reaction i.e., when $m + n = 1$, we have $\Delta = 0$. In such cases, we need an improved analysis. Such an investigation we leave open for a future study.

For a second- or higher-order reaction, i.e., when $m + n \geq 2$, we notice that the sign of $\Delta$ varies as the negative of the product of the partial orders $m$ and $n$ of the reactants $A$ and $B$. Thus, for all $m, n \geq 0$, we have a negative $\Delta$, wherefore new products are formed. On the other hand, when either $m$ or $n$ takes a negative value, we have a different result than the above, i.e., a new product is formed when either $r_{11}$ or $r_{22}$ takes a negative value. In this concern, our analysis takes an account of the fractional- and negative-order reactants and their equilibrium formation. This is because our analysis is valid for any real valued concentrations $c_1$ and $c_2$ and any real values of the partial orders $m$ and $n$ of the reactants $A$ and $B$.

In the sequel, we concentrate on the nitrogen-based reactants, organic reactions, and catalytic oxidation of Co-$H_2$ mixtures.

*5.1. An Inorganic Equilibrium Formation*

In this subsection, we offer an experimental prediction of our analysis for an inorganic reaction, see [31] in the light of the reaction mechanism and chemical kinetics of inorganic reactions towards the experimental and theoretical studies. To do so, let us consider an equilibrium between ammonium and nitrite ions [31,32] as a nitrogen-based reaction with the reactants as $A = NH_4^+$ and $B = NO_2^-$, i.e., the reaction of ammonium and nitrite ions in water at 25 °C as per the equilibrium

$$\begin{array}{ccc} NH_4^+ + NO_2^- & \rightleftharpoons & \text{Products} \\ \quad c_1 \quad c_2 & & \\ m = 1 \quad n = 1 & & \end{array} \tag{26}$$

Thus, the rate of the reaction is given by

$$r = [NH_4^+][NO_2^-] \tag{27}$$

In this case, we see that the overall order of the reaction is $m + n = 2$. Thus, for all $c_1$ and $c_2$, we have $\Delta < 0$, and therefore our analysis predicts formation of new products via the reaction of the reactants $NH_4^+$ and $NO_2^-$.

*5.2. An Organic Equilibrium Formation*

To illustrate our analysis for organic reactions let us consider hydrolysis of the $CH_3CO_2H$ molecules. As per the Bronsted-Lowry theory [33,34], this reaction is mediated by the following equilibrium:

$$\begin{array}{ccc} CH_3CO_2^- + H_3O^+ & \rightleftharpoons & CH_3CO_2H + H_2O \\ \quad c_1 \quad c_2 & & \\ m = 1 \quad n = 1 & & \end{array} \tag{28}$$

Thus, the rate of the above reaction is given by

$$r = [CH_3CO_2^-][H_3O^+] \tag{29}$$

Here, it is known [33,34] that the partial order of the reactants $CH_3CO_2^-$ and $H_3O^+$ are $m = 1$ and $n = 1$ respectively. Thus, the overall order of the reaction is $m + n = 2$. As in the previous case, in this case also for all $c_1$ and $c_2$, we observe that the determinant $\Delta$ takes a negative value, whereby the new products $CH_3CO_2H$ and $H_2O$ are formed. In the sequel, we discuss an oxidation of $CO - H_2$ mixtures in presence of $Pt$ as the catalyst.

*5.3. A Catalytic Oxidation of $CO - H_2$ Mixtures*

In the sequel, we provide verification of our results for the oxidation of $CO - H_2$ mixtures, i.e., an equilibrium with catalyst $Pt$ to make the oxidation of $CO - H_2$ mixtures [35]. Consider the general oxidation of $a$ mole of $CO$ with $b$ mole of $H_2$ as per the equilibrium

$$a\ CO + b\ H_2 \overset{\text{Pt}}{\rightleftharpoons} c\ CO_2 + d\ H_2O \tag{30}$$

forming $c$ mole of $CO_2$ and $d$ mole of $H_2O$. The equilibrium takes place [35] with the following intermediate steps

$$\begin{aligned} CO + \star &\overset{k_1}{\rightleftharpoons} CO^\star \\ O_2 + \star &\overset{k_2}{\rightleftharpoons} O_2^\star \\ O_2^\star &\overset{k_3}{\rightleftharpoons} O^\star + O^\star \\ CO^\star &\overset{k_4}{\rightleftharpoons} CO_2(\uparrow) + 2\star \\ H_2 + 2\star &\overset{k_5}{\rightleftharpoons} 2H^\star \\ H^\star + O^\star &\overset{k_6}{\rightleftharpoons} OH^\star + \star \\ OH^\star + H^\star &\overset{k_7}{\rightleftharpoons} H_2O + 2\star, \end{aligned} \tag{31}$$

where the $k_i, i = 1, 2, \ldots, 7$ are the respective rate constants of the above intermediate reactions. In this case, it is found [35] that the order of the reactants, viz. $CO$ and $H_2$ take their respective values as $m = 1$ and $n = -1/2$ respectively. Thus, the oxidation is described as per the equilibrium

$$\begin{aligned} a\,CO + b\,H_2 &\overset{\text{Pt}}{\rightleftharpoons} c\,CO_2 + d\,H_2O \\ c_1 \quad & \quad c_2 \\ m = 1 \quad & n = -1/2 \end{aligned} \tag{32}$$

Thus, the associated rate of the above oxidation reaction reads as

$$r = [CO][H_2]^{-1/2} \tag{33}$$

Therefore, the overall order of the reaction is $m + n = 1/2$. Herewith, we see that the determinant $\Delta$ takes a negative value. Thus, in this case, new matters are formed, that is, a catalytic oxidation of $CO - H_2$ mixtures in presence of $Pt$ results into the formation of $CO_2$ and $H_2O$.

## 6. Future Scope of the Work

In this section, we offer highlights and applications of the fluctuation theory analysis towards reaction mechanisms, donation of a proton, titration analysis, fall of the proton, Bronsted-Lawry equilibrium, buffer capacity, $pH$ value and the issues of acid raining as below.

### *6.1. Proton Donor-Acceptor Equilibrium*

An optimized formation of the proton donor-acceptor equilibrium plays an important role in various chemical industries, see [36] for molecular interactions and electron donor-acceptor complexes in the light of the proton affinity. Thus, we offer a general method to describe such an acid-base equilibrium of an arbitrary acid $HA$ with its conjugate base $A^-$. Depending on the nature of $A$, the electric charges of the reacting species is decided. However, the base $A^-$ always possesses a negative charge comparison to the acid $HA$. Therefore, an acid-base system consists of at least a pair of species governing the equilibrium of chemical reactions.

To study acid-base equilibrium in a quantitative way, there are two problems that come into picture. Firstly, an inability of the proton to exist independent in a solution is a major issue. Chemically, this makes an inadequate prediction of the acid or base to donate or accept a proton individually. To overcome this situation, the acid-base system must be compared and evaluated up to an extent at which the base and acid compete for combining with the proton. Thus, our proposed fluctuation

theory-based optimization of the chemical rate is anticipated to precisely illustrate the formation of an equilibrium.

The second pitfall is the dual nature of water which exists both as the acid and base, see [37] for the corresponding vibrational spectroscopic evidence. In general, most experiments on the acid-base chemistry involve the presence of aqueous solution. Therefore, for dealing with an acid $HA$ in the aqueous solution, it is necessary to consider an acid with its conjugate base to form an acid-base pair. An optimized formation of such a pair is in the future scope of this work.

### *6.2. Fall of the Proton*

As far as the fall of the proton is concerned, an acid is known as the proton donor with respect to a base that can accept the proton. However, a base accepts a proton, if there exists an acid which can donate a proton in a given aqueous solution. In general, there are energetic conditions that must be fulfilled in order that a base accepts a proton, involves a lowering in its free energy compared to the corresponding acid, see [38]. Thus, a given acid-base reaction takes place, if the proton released from the acid fall to a lower free energy level. Indeed, acids act as a source of the protons, which move to a base acting as a sink.

For the aqueous solutions, the water turns out to be the best sink for an acid, as it normally loses protons to $H_2O$ to form $H_3O^+$ as the strongest acid [39]. This is termed as the leveling effect which plays an important role in connection with the fall of the protons. All strong acids that are said to be 100% dissociated in an aqueous solution, if they possess a large equilibrium constant, therefore they are bound to endure a fall in the respective free energy. In this concern, various strong acids, e.g., $HCl$, $H_2SO_4$ and others encounter $H_2O$ solely via an existence of the $H_3O^+$, see [12] for experimental perspectives. Energetically, this follows because there exists a definite capacity of $H_2O$ to act as a proton sink by maintaining a non-vanishing free energy [38].

On the other hand, a weak acid, e.g., $HCN$ does not undergo dissociation sharply without the presence of an energy source. This happens because $HCN$ has a positive free energy, which the proton must attain for its dissociation. Concerning a titration with such weak acids, we know [40] that the hydroxyl ion $OH^-$ can equally act as a proton sink. Namely, upon the addition of a strong base, e.g., $NaOH$, $KOH$, an acid lowers the free energy of the total configuration as the fall of its protons $H^+$ from a relatively higher energy state into $OH^-$ of the base according to the reaction

$$H^+ + OH^- \longrightarrow H_2O \tag{34}$$

Therefore, a titration could be realized as the mechanism to obtain a lower free energy sink that converts the acid by draining off the protons into their respective conjugate bases. As mentioned before, the $pH$ of an arbitrary solution is generally defined based on the available hydrogen ion concentration on the logarithmic scale. Based on the above energy constraints, the $pH$ scale specifies an accessibility of protons in the solution, which incidentally reflects the capacity of the chosen solution to supply more protons to a base. To illustrate our optimization analysis, we may consider a mixture of weak acid-base systems, e.g., various biological fluids and natural water sources such as ocean, see [41] for the associated protides. In such cases, existing protons jump into the lowest possible free energy state to form a chemical equilibrium.

Initially, this begins by accommodating a lowest energy sink, therefore filling up the succeeding energy levels. This process continues until all the proton vacant sites in a given base are filled with an optimum cutoff energy, which largely depends upon characteristics of the considered acid. This analysis is left open for a future research. Chemically, by various thermal excitations, the highest protonated species donate protons to $H_2O$ to form $H_3O^+$ whose concentration largely depends on concentrations of different species. In short, an optimized amount of $H_3O^+$ concentration enables us in defining the equilibrium $pH$ of the corresponding solution. In other words, a $pH$ measurement points out the relative free energy of protons required to preserve the highest protonated species in

their acid forms [12,38]. Herewith, it is worth emphasizing that our discussion can be applied for the determination of the proton free energy by $pH$ scale measurements.

*6.3. Buffer Capacity*

In the light of quantitative treatments of chemical equilibria, we focus on acid-base phenomena arising from the hydronium ion [39]. In this aspect, a titration can happen in non-aqueous solvents, as well. Such acid-base systems came into the existence by independent investigations of Bronsted and Lowry in 1923, see [39] for related fundamentals and their historical accounts. Subsequently, in both the aqueous and non-aqueous solvents, an acid can be regarded as the species that can donate a proton and the corresponding base as the species that can accept it. Examples of non-aqueous solvents include alcohol, benzene, ether, carbon tetrachloride, acetone, and other organic solvents, while the liquid ammonia, disulfide and sulfuric acid arise in the category of the inorganic solvents. In this regard, for a given acid $HA$ and base $B$, our optimization analysis is explained by the following chemical equilibrium.

$$\begin{aligned} HA &\rightleftharpoons H^+ + A^- \\ H^+B &\rightleftharpoons BH^+ \end{aligned} \tag{35}$$

From the perspective of the Bronsted and Lowry [39], the notion of a chemical equilibrium is based on the proton itself and not on the hydronium ion, whereby one finds a solvent independent of the chemical equilibrium. Specifically, because of an accepting behavior of the proton $H^+$ of $A^-$, it acts as a base as above in the first reaction as in Equation (35). However, in the second reaction as in Equation (35), $BH^+$ behaves as an acid since it donates a proton $H^+$ to the base $B$. This yields the following Bronsted-Lowry acid-base [39] chemical equilibrium.

$$\text{Acid} \rightleftharpoons H^+ + \text{Base} \tag{36}$$

Essentially, as per the above acid-base pair having a deficit of the proton $H^+$ as in Equation (36), an optimized conjugate acid-base pair is anticipated to arise via our fluctuation theory analysis. Indeed, the above-mentioned Bronsted-Lowry definition of the acid-base pair does not state the type of the charges present in either of the acid or base, i.e., the chemical equilibrium formation has nothing to do with electronic charges of the species and it is rather independent of their ionization properties [39]. In short, we may recite the formation of an acid-base equilibrium by stating that an acid has one more positive charge than its corresponding conjugate base. This offers a perspective application of our proposal to pharmaceutical systems and their thermodynamic characterization. In the highlight of the same, it is worth anticipating that an optimized chemical equilibrium is formed by the acid $CH_3CH_2COOH$ with its conjugate base $CH_3CH_2COO^-$ by exchanging a proton $H^+$.

To perform chemical composition analysis [42], the titration offers a conventional laboratory tool to calculate unknown concentration of a set of given chemical species. Thus, among various types of titration methods, we focus on an optimized acid-base titration, which anticipated to emerge as an important topic of current research. Namely, in a given solution, our proposition involves the concept of an optimal neutralization of an acid-base pair. Here, the concentration of the chosen acid or base is calculated by the addition of the respective base or acid with their known concentrations. In this case, we can add a $pH$ indicator to the solution to determine the optimal point of the solution by observing a change in its color.

Therefore, our method support that the buffer capacity arises as the resistance to $pH$ change of a solution. Namely, given an acid with its conjugate base, the buffer capacity plays a vital role in determining the relative dissociation, which follows via Châtelier principle [43,44]. In general, an aqueous solution consists of a weak acid and its conjugate base or vice-versa, therefore the formation of a buffer solution. One of the main characteristics of buffer solutions is to maintain a steady $pH$ value upon an addition of a strong acid or base. Thus, the $pH$ buffers arise as the best alternatives to

maintain a constant $pH$ value of chemical solutions. In the setup of Bronsted and Lowry theory, viz. Equation (36), buffer solutions acquire an optimized resistance to $pH$ change due to the formation of a chemical equilibrium between the weak acid $HA$ and its conjugate base $A^-$. Thus, for a given buffer solution, its buffer capacity yields a quantitative measurement for determining the optimal resistance of $pH$ change [12,38] upon an addition of hydroxide ions. Such issues we leave open for future research and developments.

### *6.4. Acid Raining*

In the sequel, we focus on the nature of an optimized rate via the acid-base chemistry. In general, we are interested in chemical reactions which are optimally formulated in the light of the acid-base chemistry. Acid-base reaction can be described as the reaction between hydrogen ions with other electrically charged species or neutral ones. The reaction between acid and base is considered to be a reversible reaction. This means, the product obtained could react among themselves to give the reactant back. In the light of acid-base chemistry, this idea is the root cause towards an optimized chemical equilibrium formation [26] in the realism of chemical kinetics.

Various environmental problems arise because of the acid raining, see [45] for environmental problems and their existing remedies. Notice that acid rain refers to presence of acid in the rain water due to effects of pollutants exhausted into the atmosphere such as automobiles and factories. In this regard, sulfur dioxide and nitrogen oxides accounts for the main pollutants responsible for the cause. When such gaseous species react with the water and oxygen molecules present in the atmosphere, it results in the formation of acids such as sulfuric acid and nitric acid in rain water. Thus, acid rain creates various damage such as corrosion of metals and their salt hydrates [46], damage to buildings [47], etc. Thus, one finds diverse effects of $CO_2$ water. It is reported that the amount of $CO_2$ in the atmosphere is increasing day by day due to the burning of fossil fuels in the presence of oxygen. The above-mentioned $CO_2$ tend to dissolve in the ocean water by forming carbonic acid. Thus, to safeguard the natural resources, an optimized emission of $CO_2$-based species falls in the domain of the future scope of this research.

## 7. Summary and Conclusions

In the present research, we have thoroughly examined the optimized formation of chemical equilibria via the fluctuation theory. Our consideration was based on the formation of an intermediate state of products whose energy crosses the potential barrier to form the final state. Various concentrations of reacting species in a given chemical reaction can fluctuate. At a constant temperature, fluctuations in the rate are characterized by a weighted product of concentrations of the reacting species with different orders. We observed that the stability of the equilibrium depends mainly on these parameters of the reactants.

As far as the fluctuation theory is concerned, our analysis is based on the statistical and thermodynamic factors that determine the characteristic properties of a given chemical reaction. We have provided fluctuation theory perspective towards the formation of chemical equilibria of arbitrary orders. Here, the progress of a chemical reaction is governed by a step by step infinitesimal modification of the law of mass action. This is realized by varying the reaction rate governing the changes in a given chemical reaction. It is worth mentioning that the above equilibrium is not immediately achieved, but it arises as a collective phenomenon. An apt formation of such equilibria is the subject matter of this research.

Given a binary component chemical reaction, we have computed the flow components, chemical capacities, chemical correlation, and associated fluctuation quantities concerning the global stability of an equilibrium. Under fluctuations of the reactant's concentrations, we find that the equilibrium is formed when either one of the orders of the reactants vanishes or either of their concentrations vanishes. The chemical concentration capacities of the components are calculated to describe the local stabilities of the equilibrium. The correlation between the components is obtained as the mixed

second-order derivative of the rate with respect to the concentrations. To be precise, we find that the local system stability requires the order of the reactants to be either negative or larger than the unity.

On the other hand, for a binary component reaction, the global stability analysis is performed by introducing a symmetric matrix with its diagonal components as the chemical capacities and off-diagonal components as the chemical correlation. The global stability of the system requires the positivity of a factor over the orders of the reactants that we have examined both quantitatively and qualitatively. For reactants of the order less than two, we infer from our observations that the fluctuations are mostly originating at the points where either of the concentration approaches zero value. However, for the reactants of second orders, we find a global instability as the corresponding determinant of the fluctuation matrix takes a large negative value of the order $10^7$. In addition, for a pair of reactants of their orders of the same sign, the reaction is globally stable when the sum of their orders is less than unity. This well coincides with the observations for the reactions of the orders $(-1,-1)$ as in Figure 1. The instability gets introduced as the orders gradually change to their values $(-1,1/2)$, $(-1,2)$, $(1/2,1/2)$, $(1/2,2)$ and $(2,2)$ as depicted in Figures 2–6 respectively.

Subsequently, we have offered verification of our model. Following the above theory, we focus on stability structures of the chemical equilibrium formation of the carbon materials under variations of concentrations of the participating species while the other parameters of the reaction are held fixed. To understand the formation of a chemical equilibrium as a statistical sample, we have introduced simultaneous fluctuations over active masses, i.e., the concentrations of reacting species with the associated rate as an embedding function. This offers the optimization properties of a given chemical equilibrium and thus the formation of products. Thus, we have discussed the stability of chemical equilibria and formation of products involving carbon materials such as an organic reaction and a catalytic oxidation of $CO-H_2$ mixtures in presence of Pt and other inorganic reactions, as well.

Our proposition can be understood based on macroscopic observations governing the forward and reverse reactions. Namely, a chemical equilibrium arises as an average of the microscopic concept that takes place when a given amount of chemical species remains same. The global stability of an equilibrium originates via collisions between the molecules, therefore the dissociation of the reacting species. Furthermore, in the vicinity of equilibrium, the fluctuation analysis can be exploited by varying either the forward rate over the concentration of the reactants, or the backward rate of the products. This is because the equilibrium constant reads as the ratio of the rate constants of the forward reaction to that of the backward reaction. It is evident from our observations that a chemical reaction never proceeds until its end; instead, it attends an equilibrium state when the available amount of participating species in the reaction does not fluctuate. From the above perspectives, we find that all the fluctuation quantities vanish identically for a zeroth-order chemical reaction, except its rate. In addition, we have classified all possibilities concerning the stability of the equilibrium formed by a given pair of reacting species with different orders.

In general, the fluctuation theory-based chemical equilibrium can equally depend on the temperature, pressure, volume, and chemical compositions of the reacting species, as well. This can provide further possibilities for research. Indeed, our proposal can be generalized for arbitrary chemical reactions with finitely many reactants and products, as well. Other directions include unification of the fluctuation theory analysis with the physical state of the reacting species, reaction temperature and use of a catalyst. This depends on the collision frequency, phase of reactants and random thermal motion of molecules to form a new state. Also, the temperature variations enhance the reaction rate, namely, they increase the collision frequency between the molecules of interacting species.

Finally, we anticipate future scope of our work in the light of the acid-base chemistry, fall of the protons, thermal excitations, formation of hydronium ions, buffer capacity as well as industrial implications towards the thermodynamic properties of pharmaceutical configurations, formation of buffer solutions, corrosion of metals, protection of building, environment and ecosystems, and pollutant exhaust management for automobiles and factories. Moreover, it worth mentioning that a

chemical equilibrium requires an understanding of the electron affinity and reactivity of the species, as well. Such investigations we leave open for future research and developments.

**Author Contributions:** Conceptualization, B.N.T. and S.C.K.; Data curation, B.N.T.; Formal analysis, B.N.T.; Investigation, B.N.T., S.C.K., N.M. and S.B.; Methodology, B.N.T. and S.B.; Project administration, N.M.; Resources, S.C.K. and N.M.; Supervision, S.B.; Validation, B.N.T. and S.C.K.; Visualization, B.N.T., S.C.K. and S.B.; Writing—original draft, B.N.T. and S.C.K.; Writing—review & editing, B.N.T., S.C.K., N.M. and S.B.

**Funding:** This research received no external funding.

**Conflicts of Interest:** The authors declare no conflict of interest.

## References

1. Blinder, S.M.; Nordman, C.E. Collision theory of chemical reactions. *J. Chem. Educ.* **1974**, *51*, 790. [CrossRef]
2. Scribed, Kinetics: Rates and Mechanisms of Chemical Reactions. Available online: https://www.scribd.com/document/85038774/Chapter-16 (accessed on 10 January 2017).
3. Miller, W.H. Quantum mechanical transition state theory and a new semiclassical model for reaction rate constants. *J. Chem. Phys.* **1974**, *61*, 1823–1834. [CrossRef]
4. Atkins, P.; de Paula, J. *Physical Chemistry*, 10th ed.; W. H. Freeman: New York, NY, USA, 2014; ISBN 13-978-1429290197.
5. Eyring, H. Quantum Mechanics and Chemical Reactions. *Chem. Rev.* **1932**, *10*, 103–123. [CrossRef]
6. Boudart, M. *Kinetics of Chemical Processes*; Brenner, H., Ed.; Butterworth-Heinemann: Oxford, UK, 1991; pp. 13–16, ISBN 9780750690065.
7. Bransden, B.H.; Joachain, C.J. *Physics of Atoms and Molecules, Pearson*, 2nd ed.; Pearson Education: Delhi, India, 2003.
8. Karplus, M.; Porter, R.N. *Atoms and Molecules: An Introduction for Students of Physical Chemistry*; Benjamin Cummings: San Francisco, CA, USA, 1970; ISBN 0-8053-5218-8.
9. Haas, E.; Katchalski-Katzir, E.; Steinberg, I.Z. Effect of the orientation of donor and acceptor on the probability of energy transfer involving electronic transitions of mixed polarization. *Biochemistry* **1978**, *17*, 5064–5070. [CrossRef] [PubMed]
10. Espenson, J.H. *Chemical Kinetics and Reaction Mechanisms*, 2nd ed.; McGraw-Hill Education: New York, NY, USA, 2002; ISBN 13-978-0072883626.
11. DeCoursey, W.J.; Thring, R.W. Effects of unequal diffusivities on enhancement factors for reversible and irreversible reaction. *Chem. Eng. Sci.* **1989**, *44*, 1715–1721. [CrossRef]
12. Pokrovsky, O.S.; Schott, J. Experimental study of brucite dissolution and precipitation in aqueous solutions: Surface speciation and chemical affinity control. *Geochim. Cosmochim. Acta* **2004**, *68*, 31–45. [CrossRef]
13. Califano, S. *Pathways to Modern Chemical Physics*; Springer: Berlin/Heidelberg, Germany, 2012; ISBN 978-3-642-28180-8.
14. Huang, K. *Statistical Mechanics*, 2nd ed.; Wiley: Hoboken, NJ, USA, 1987; ISBN 13-978-0471815181.
15. Pathria, R.K. *Statistical Mechanics*, 2nd ed.; Butterworth-Heinemann: Oxford, UK, 1996; ISBN 13-978-0750624695.
16. Bigeleisen, J.; Wolfsberg, M. Theoretical and experimental aspects of isotope effects in chemical kinetics. *Adv. Chem. Phys.* **2007**, *1*, 15–76.
17. Ruppeiner, G. Reimannian geometry in thermodynamic fluctuation theory. *Rev. Mod. Phys.* **1995**, *67*, 605. [CrossRef]
18. Bellucci, S.; Tiwari, B.N. On the microscopic perspective of black brans thermodynamic geometry. *Entropy* **2010**, *12*, 2097–2143. [CrossRef]
19. Weinhold, F. Metric geometry of equilibrium thermodynamics. *J. Chem. Phys.* **1975**, *63*, 2479. [CrossRef]
20. Weinhold, F. Metric geometry of equilibrium thermodynamics: Scaling, homogeneity and generalized Gibbs-Duhem relations. *J. Chem. Phys.* **1975**, *63*, 2484. [CrossRef]
21. Tiwari, B.N. *Geometric Perspective of Entropy Function: Embedding, Spectrum and Convexity*; LAMBERT Academic Publishing: Riga, Latvia, 2011; ISBN 13-978-3845431789.
22. Tiwari, B.N.; Kuipo, J.K.; Bellucci, S.; Marina, N. On Extensions of the Optical Optimization. *Am. Sci. Res. J. Eng. Technol. Sci.* **2016**, *26*, 302–313.
23. Diercks, C.S.; Yaghi, O.M. The atom, the molecule, and the covalent organic framework. *Science* **2017**, *355*, eaal1585. [CrossRef] [PubMed]

24. Espenson, J.H. *Chemical Kinetics and Reaction Mechanisms*; McGraw-Hill: New York, NY, USA, 1995; Volume 102.
25. Laidler, K.J. *Chemical Kinetics*, 3rd ed.; Harper & Row: Manhattan, NY, USA, 1987; ISBN 9780060438623.
26. Denbigh, K.G. *The Principles of Chemical Equilibrium: With Applications in Chemistry and Chemical Engineering*; Cambridge University Press: Cambridge, UK, 1981; ISBN 13-978-0521281508.
27. Sandler, S.I. *Chemical, Biochemical, and Engineering Thermodynamics*, 4th ed.; John Wiley & Sons: Hoboken, NJ, USA, 2006; ISBN 13-978-0471661740.
28. Voit, E.O.; Martens, H.A.; Omholt, S.W. 150 years of the mass action law. *PLoS Comput. Biol.* **2015**, *11*, e1004012. [CrossRef] [PubMed]
29. Alberto, M.E.; Russo, N.; Grand, A.; Galano, A. A physicochemical examination of the free radical scavenging activity of Trolox: Mechanism, kinetics and influence of the environment. *Phys. Chem. Chem. Phys.* **2013**, *15*, 4642–4650. [CrossRef] [PubMed]
30. IUPAC. Compendium of Chemical Terminology—The Gold Book. Available online: https://goldbook.iupac.org/ (accessed on 24 June 2017).
31. Nguyen, D.A.; Iwaniw, M.A.; Fogler, H.S. Kinetics and mechanism of the reaction between ammonium and nitrite ions: Experimental and theoretical studies. *Chem. Eng. Sci.* **2003**, *58*, 4351–4362. [CrossRef]
32. Chemical Kinetics. Chapter 14. Available online: https://www.sas.upenn.edu/~mcnemar/apchem/ch14.pdf (accessed on 21 October 2018).
33. Petrucci, R.H.; Herring, F.G.; Madura, J.D.; Bissonnette, C.; *General Chemistry: Principles and Modern Applications*; Pearson: London, UK, 2017.
34. Freeman, S.; Sharp, J.C.; Harrington, M. *Biological Science*; Prentice Hall: Upper Saddle River, NJ, USA, 2002; Volume 1.
35. Pedrero, C.; Waku, T.; Iglesia, E. Oxidation of CO in H2-CO mixtures catalyzed by platinum: Alkali effects on rates and selectivity. *J. Catal.* **2005**, *233*, 242–255. [CrossRef]
36. Morokuma, K. Why do molecules interact? The origin of electron donor-acceptor complexes, hydrogen bonding and proton affinity. *Acc. Chem. Res.* **1977**, *10*, 294–300. [CrossRef]
37. Musto, P.; Ragosta, G.; Mascia, L. Vibrational spectroscopy evidence for the dual nature of water sorbed into epoxy resins. *Chem. Mater.* **2000**, *12*, 1331–1341. [CrossRef]
38. Lower, S.K. Acid-Base Equilibria and Calculations. Available online: http://www.chem1.com/acad/pdf/c1xacid2.pdf (accessed on 14 December 2018).
39. Connors, K.A. *Thermodynamics of Pharmaceutical Systems: An Introduction for Students of Pharmacy*; John Wiley & Sons Inc.: Hoboken, NJ, USA, 2002; Chapter 12, pp. 157–158.
40. Agmon, N.; Bakker, H.J.; Campen, R.K.; Henchman, R.H.; Pohl, P.; Roke, S.; Thamer, M.; Hassanali, A. Protons and hydroxide ions in aqueous systems. *Chem. Rev.* **2016**, *116*, 7642–7672. [CrossRef]
41. Peeters, H. (Ed.) *Protides of the Biological Fluids: Proceedings of the Twentieth Colloquium, Brugge, 1976*; Elsevier: Amsterdam, The Netherlands, 2014.
42. Harris, D.C. *Quantitative Chemical Analysis*, 7th ed.; Freeman and Company: New York, NY, USA, 2007.
43. Butler, J.N. *Ionic Equilibrium: A Mathematical Approach*; Addison-Wesley: Boston, MA, USA, 1964; p. 151, ISBN 13-978-0201007305.
44. Hulanicki, A. *Reactions of Acids and Bases in Analytical Chemistry*; Translated by Masson, Translated by Masson, M.R.H.; Halsted Press: Ultimo, Australia, 1987.
45. Rajagopalan, R. *Environmental Studies: From Crisis to Cure*, 3rd ed.; Oxford University Press: Oxford, UK, 2015.
46. Solé, A.; Miró, L.; Barreneche, C.; Martorell, I.; Cabeza, L.F. Corrosion of metals and salt hydrates used for thermochemical energy storage. *Renew. Energy* **2015**, *75*, 519–523.
47. Dillmann, P.; Beranger, G.; Piccardo, P.; Matthiessen, H. *Corrosion of Metallic Heritage Artefacts: Investigation, Conservation and Prediction of Long Term Behaviour*; Elsevier: Amsterdam, The Netherlands, 2014.


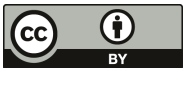

condensed matter

MDPI

*Article*

# Effect of High-Temperature Annealing on Graphene with Nickel Contacts

**Tommi Kaplas [1,*], Vytautas Jakstas [1], Andrius Biciunas [1], Algimantas Luksa [2], Arunas Setkus [2], Gediminas Niaura [3] and Irmantas Kasalynas [1]**

1 Department of Optoelectronics, Center for Physical Sciences and Technology, Sauletekio Ave. 3, LT-10257 Vilnius, Lithuania; vytautas.jakstas@ftmc.lt (V.J.); andrius.biciunas@ftmc.lt (A.B.); irmantas.kasalynas@ftmc.lt (I.K.)

2 Department of Physical Technologies, Center for Physical Sciences and Technology, Sauletekio Ave. 3, LT-10257 Vilnius, Lithuania; algimantas.luksa@ftmc.lt (A.L.); arunas.setkus@ftmc.lt (A.S.)

3 Department of Organic Chemistry, Center for Physical Sciences and Technology, Sauletekio Ave. 3, LT-10257 Vilnius, Lithuania; gediminas.niaura@ftmc.lt

* Correspondence: tommi.kaplas@ftmc.lt

Received: 9 January 2019; Accepted: 1 February 2019; Published: 6 February 2019

**Abstract:** Graphene has shown great potential for ultra-high frequency electronics. However, using graphene in electronic devices creates a requirement for electrodes with low contact resistance. Thermal annealing is sometimes used to improve the performance of contact electrodes. However, high-temperature annealing may introduce additional doping or defects to graphene. Moreover, an extensive increase in temperature may damage electrodes by destroying the metal–graphene contact. In this work, we studied the effect of high-temperature annealing on graphene and nickel–graphene contacts. Annealing was done in the temperature range of 200–800 °C and the effect of the annealing temperature was observed by two and four-point probe resistance measurements and by Raman spectroscopy. We observed that the annealing of a graphene sample above 300 °C increased the level of doping, but did not always improve electrical contacts. Above 600 °C, the nickel–graphene contact started to degrade, while graphene survived even higher process temperatures.

**Keywords:** graphene; annealing; doping; electric contacts

## 1. Introduction

In the past 15 years, graphene has attracted an enormous amount of interest from the scientific community. Unique properties like ballistic, high-mobility charge carriers at room temperature have made this monoatomic layer of graphite a material with high potential for futuristic, high-speed electronic applications. However, in order to implement graphene for electronic devices, there is a requirement to introduce low-resistance ohmic contacts to the graphene–metal interface.

A lot of work has been dedicated to finding good electrical contacts for graphene and other 2D materials [1–4]. For this purpose, many metals (e.g., Ag, Al, Au, Co, Cr, Cu, Fe, Ni, Pd, Pt, and Ti) have been tested [2–7]. Among these metals, nickel has especially proven to have great potential, since it creates a good contact with graphene due to the chemisorption mechanism [8]. Furthermore, the thermal annealing of samples has been shown to enhance the electric contact between nickel and graphene [9–12].

In addition, to enhance electrical contacts, high-temperature annealing is frequently used for cleaning graphene after depositing it on a dielectric surface [13]. More specifically, graphene is conventionally synthetized on a transition metal substrate by chemical vapor deposition and then transferred by a polymer support onto a dielectric substrate. The transfer process usually contaminates the surface of graphene with residual polymer particles, but it is possible to remove

the polymer contaminants from the graphene surface by thermal annealing in order to improve its performance [13,14].

Graphene cleaning and contact annealing at elevated temperatures poses the question of what annealing does to the properties of graphene and at what temperature annealing should be performed. A precise understanding of what happens to graphene during annealing is crucially important, and therefore, this topic has been widely investigated [10,12–16]. For instance, Lin et al. observed that rather low-temperature (200–300 °C) thermal annealing is a simple technique to clean polymer particles from the surface of graphene [13]. However, thermal cleaning leaves a fair amount of polymer residuals on the surface of graphene, and more importantly, it also increases its doping level after exposure to air and humidity [13,15,16]. Moreover, Cheng et al. reported that an optimized annealing process might increase electron mobility in graphene [12]. They found that annealing graphene at 200 °C almost doubled electron mobility. In addition, they observed that, when the annealing temperature increases above 200 °C, the electron/hole mobility starts to decrease. Furthermore, Leong et al. explained the mechanism of how annealing affects Ni–graphene contacts at 300 °C [10]. They found that annealing graphene with a nickel contact causes some carbon atoms from graphene to be dissolved into Ni, resulting in small holes in the graphene lattice. Eventually, this creates strong chemical bonding between nickel and graphene, which in turn improves the performance of the electrode [10]. Therefore, based on these earlier studies, one may conclude that the most beneficial thermal annealing temperature range is 200–300 °C.

While there have been several studies focusing on graphene annealing with and without contacts below 400 °C, only a small number of studies indicate what happens to graphene above 400 °C [15]. Moreover, there is still no clear understanding of what happens to graphene in contacts at very high temperatures. In this work, we extend previous works by systematically studying the effect of extreme annealing temperature on graphene and nickel–graphene contacts. In our experiment, we annealed a graphene sample with nickel contacts in the temperature range of 200−800 °C. Changes in graphene properties were observed by measuring its electrical resistivity and Raman spectra.

## 2. Results

### *2.1. Sample Preparation*

Graphene was grown on a copper foil by a conventional hot wall chemical vapor deposition (CVD) technique [17]. The synthetized graphene film was transferred by the wet transfer method on an oxidized (280 nm) silicon substrate [18,19]. Briefly, the graphene sample was spin-coated with a poly(methyl methacrylate) (PMMA) film of 100 nm thickness. The underlying copper was etched in a mild ferric chloride solution (~5 g FeCl + 100 mL $H_2O$) overnight. After etching of the copper substrate, the graphene+PMMA was cleaned with an RCA-SC2 solution (10 mL HCl + 10 mL $H_2O_2$ + 150 mL $H_2O$) for 10 min. Thereafter, the graphene+PMMA sample was rinsed twice in water for 20 min and deposited onto the silicon substrate. The sample was dried at room temperature overnight, and finally, the PMMA support was removed by using an acetone bath (2 h), followed by rinsing in isopropanol and water for 5 and 10 min, respectively.

Nickel contacts were fabricated by an electron beam evaporator through a shadow mask. Figure 1 schematically illustrates the geometry of the sample. Disk-shaped contacts were 500, 600, and 750 µm in diameter (d1, d2, and d3, respectively). The contact spacing was 2 mm, and the thickness of the evaporated Ni layer was 50 nm. Ni–graphene contact was expected to be ohmic [7], which we confirmed by measuring a linear I–V curve.

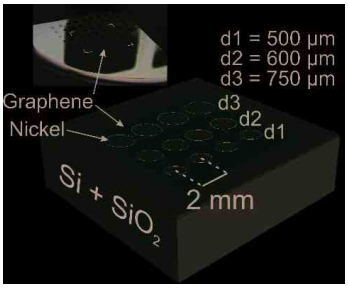


**Figure 1.** A schematic illustration of the graphene with nickel contacts on the oxidized silicon substrate. The thickness of the contact nickel film was 50 nm, and the spacing between contacts was 2 mm. The inset shows a photograph of the actual sample.

The sample was annealed using a rapid thermal annealing device (Unitemp RTV-100HV) under an argon atmosphere (in 2000 sccm flow at atmospheric pressure). Before the contact annealing, the sample was pre-annealed at 200 °C for 3 min to remove moisture from the sample surface. Thereafter, the process temperature was increased up to the actual annealing temperature at a ramp-up rate of 10 °C/s. The sample was annealed for 3 min at the actual annealing temperature and then cooled down to 200 °C in Ar atmosphere. To increase the cooling rate, the rest of the cooling from 200 to 100 °C was done under nitrogen atmosphere. At 100 °C, the sample was removed from the chamber to room temperature.

### *2.2. Electrical Characterization*

Before and after annealing, the resistance of the sample was measured by the two and four-point probe techniques (by Keithley 2400 SMU Source Measure Unit connected to the probe station). The four-point-probe technique diminishes the effect of the contact resistance, and the resistance of graphene (Rg) was obtained directly from the experimental data [20]. The two-point-probe technique measures the total resistance (Rtot) [20], including the resistance of the two contact points (Rc) and Rg (see Figure 2a). When two contacts are identical, Rc can be estimated by subtracting Rg from Rtot and dividing this value by two (see Figure 2c).

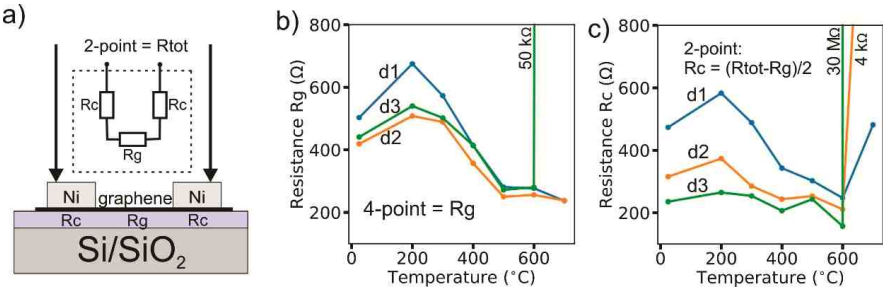


**Figure 2.** Electrical characterization of the sample. (**a**) A schematic drawing of the two-point measurement with an equivalent circuit of the sample. The equivalent circuit has two equal resistors for contacts (Rc) and one resistor for graphene (Rg). (**b**) Dependence of graphene resistance on the annealing temperature. Rg decreased significantly when the annealing temperature increased above 300 °C. (**c**) Dependence of contact resistance on the annealing temperature. For the smallest contacts (d1), the annealing decreased the contact resistance before it broke down above 600 °C. However, the contact resistance became less dependent on the annealing temperature in the case of a larger contact size (d2 and d3) due to limitations of the setup used for contact resistance measurements. Rtot: total resistance.

Figure 2b,c shows the resistance of graphene and contacts, respectively, after annealing. Figure 2b shows that the Rg value of the sample annealed in the temperature range of 200–300 °C was comparable to that of the un-annealed sample. However, annealing of the sample at temperatures above 300 °C decreased Rg significantly. When the annealing temperature was increased up to 500 °C, Rg saturated to 260 ± 20 Ω.

Moreover, Figure 2c shows that the contact between graphene and nickel started to degrade at above 600 °C and thus Rc increased rapidly. Moreover, the size of the contact seems to play an important role. For the smallest contact (d1), the annealing improved the electrical contact, which was seen as a decrease in the Rc value. However, the annealing procedure seemed to have only minor effects on the middle and largest size contacts (d2 and d3, respectively).

### *2.3. Raman Characterization*

Raman spectroscopy is a powerful tool to probe the properties of graphene. In our experiment, we measured the Raman spectra of the annealed graphene sample using the 532 nm excitation wavelength in a Renishaw inVia Raman microscope. Spectra were measured by using a 20x/0.40NA objective lens. The probe beam power was kept sufficiently low (0.6 mW) to avoid self-heating effects in graphene.

Graphene has fundamental D ("disorder") and G ("graphite") peaks located at ~1350 $cm^{-1}$ and 1582 $cm^{-1}$, respectively [21]. In addition, the 2D mode is located at ~2680 $cm^{-1}$ in the case of a pristine monolayer graphene. In the presence of doping or strain, G and 2D peaks are shifted towards 1600 and 2700 $cm^{-1}$, respectively [21,22].

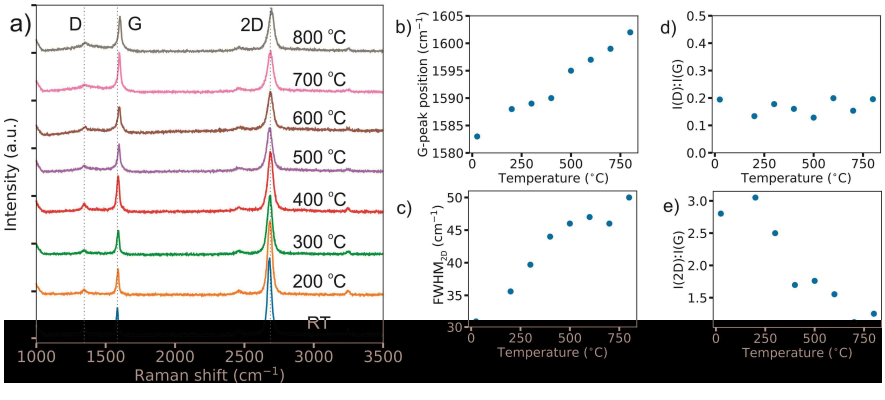


**Figure 3.** Raman characterization. (**a**) Raman spectra of the graphene sample before and after annealing at different temperatures. (**b**) The G-peak position and (**c**) 2D peak width increased linearly. (**d**) The ratio of I(D):I(G) did not depend on the annealing temperature, while (**e**) I(2D):I(G) rapidly decreased when the sample was annealed at temperatures above 300 °C.

Figure 3a shows the Raman spectra of the graphene sample before and after annealing. Even though the temperature increased from room temperature (RT) to 800 °C, there were only minor changes in the spectra. By analyzing the temperature dependence of the position of the G peak, the full width at half maximum of peak 2D ($FWHM_{2D}$), and from the intensity relations of peaks D, G, and 2D, one can observe details that indicate changes in graphene.

We made a Lorentzian fitting for peaks D, G, and 2D, and observed that the position of peak G was located at 1583 $cm^{-1}$ before annealing. Figure 3b shows that the G peak shifted linearly toward 1600 $cm^{-1}$ when the annealing temperature increased. For the sample annealed at 800 °C, the G peak appeared at 1602 $cm^{-1}$. Moreover, Figure 3c shows a linear increase in $FWHM_{2D}$ from 30 to 50 $cm^{-1}$, which was directly proportional to the annealing temperature.

Peak D only went through minor changes, despite high annealing temperatures. This indicates that only a very minor amount of PMMA remained on the graphene after the transfer process [15]. The intensity ratio of D and G peaks remained constant at all annealing temperatures, as is shown in Figure 3d. However, the intensity ratio of the 2D and G peaks decreased from three to one. The decrease in I(2D):I(G) was especially noteworthy in the range of 300−400 °C. Moreover, we observed a shift in the position of the 2D mode from 2680 $cm^{-1}$ at room temperature to 2694 $cm^{-1}$ after annealing in 800 °C.

## 3. Discussion

The sizes of the Ni contacts in this study were relatively large in comparison to those that are commonly used for the contact resistance measurement [2–6,9–11]. However, it is worth noting that, in our experiment, we measured the same position several times. Since the measurement probe consumed a thin Ni layer by scratching, the surface area of the contact was chosen to be large enough to enable several repetitive measurements. As can be seen in Figure 2c, the annealing of the largest (d2 and d3) contacts had only a minor effect on Rc. However, the importance of the annealing procedure is pronounced when the contact area is small, as has been shown in earlier studies [8,10,12] and in Figure 2c (d1 contact).

Due to the relatively large size of contacts, it is difficult to make a precise estimation of the contact resistance behavior. However, the results clearly show that the annealing of a graphene sample with nickel contacts at temperatures above 600 °C severely damaged the sample by destroying the electrical contact between graphene and nickel. The mechanism behind the damage may originate from high carbon solubility in nickel at elevated temperatures [23]. More precisely, nickel absorbs carbon atoms, and when the graphene layer is fully absorbed, the nickel–graphene contact disappears. This conclusion is supported by an earlier experiment which demonstrated that, at elevated temperatures, Ni can easily break down $sp^3$ hybridization, which has an even higher bonding energy in comparison to that of $sp^2$ hybridized graphene [24–26].

Moreover, it is worth noting that, despite a comparatively high melting temperature of the bulk Ni equal to 1455 °C, the surface melting temperature—the so-called Tamman temperature—is approximately half of this bulk melting temperature [27,28]. At this temperature, nickel atoms acquire enough energy to become mobile [27–30]. For low-dimensional systems (e.g., for contacts that are a few tens of nanometers thick), this temperature is sufficient to cause physical changes [29,30]. For instance, in Reference [30], a 10-nm-thick Ni film was melted at 700−800 °C, and one may therefore expect that thin Ni contacts will undergo major changes at temperatures above 700 °C.

Figure 2b shows that the un-annealed sample had lower Rg compared to that after annealing at 200 °C. This indicates that the sample surface was affected by moisture in the surrounding air that landed on the sample. We confirmed this by the sample that was first annealed at 300 °C and left for 12 h in air (the relative humidity was ~40%). After waiting, the Rg decreased by almost 40% (the average Rg after the annealing and after 12 h was 521 ± 45 Ω and 327 ± 24 Ω, respectively). This was caused by $H_2O$ and $O_2$ doping, which is pronounced after a graphene sample is annealed at high temperatures [16]. However, we also observed that the moisture decreased the Rc value, which suggests that the moisture at the contact point improves the electrical contact between nickel and graphene. Therefore, in Figure 2c one can observe an increase in Rc value before and after the annealing of the sample at 200 °C. When the contacts are deposited on graphene, the effect of the moisture on graphene may have an impact on the resistance between the graphene film and the metal contact. Understanding how moisture affects the contact electrodes will be part of our future work.

The position of peak G shifts toward 1600 $cm^{-1}$ when graphene becomes p-doped or when it is strained [22,31,32]. In addition, a drastic decrease in I(2D):I(G) ratio (Figure 3e) points to the dominant doping effect [31,32]. By measuring the resistance of graphene, we observed that the annealing led to a decrease in Rg, while the strain in the sample should increase the resistivity of graphene [33]. Therefore, one may expect that the shift of the G peak mainly originated from the doping effect in

graphene. However, Figure 2b shows that the resistance of graphene saturated at temperatures above 500 °C to approximately 250 Ω, which suggests simultaneous doping and straining of the graphene.

## 4. Conclusions

We observed that annealing of a graphene sample at temperatures above 200−300 °C may cause an unintentional p-type doping. When the annealing was performed at temperatures above 600 °C, the annealing process became harmful to nickel–graphene contacts. Moreover, in these cases, when the size of the electrical contacts are on the order of millimeters, annealing of a graphene sample with Ni contacts may provide no significant benefits, but in contrast, may increase the doping level in graphene. However, if the doping of a graphene sample is required, then high-temperature annealing provides a simple route for this purpose.

**Author Contributions:** Conceptualization, T.K. and I.K.; methodology, T.K., V.J., A.B., A.L. and G.N.; formal analysis, T.K., G.N. and I.K.; investigation, T.K.; resources, I.K.; writing—original draft preparation, T.K.; writing—review and editing, T.K., V.J., A.S. and I.K.; visualization, T.K.; supervision, I.K.; project administration, I.K.; and funding acquisition, I.K.

**Funding:** This work was supported by the Research Council of Lithuania under the KOTERA-PLAZA project (grant no. DOTSUT-247).

**Acknowledgments:** The authors acknowledge Irena Mirviene for language editing of the manuscript.

**Conflicts of Interest:** The authors declare no conflict of interest.

## References

1. Allain, A.; Kang, J.; Banerjee, K.; Kis, A. Electrical contacts to two-dimensional semiconductors. *Nat. Mater.* **2015**, *14*, 1195–1205. [CrossRef] [PubMed]
2. Gahoi, A.; Wagner, S.; Bablich, A.; Kataria, S.; Passi, V.; Lemme, M.C. Contact resistance study of various metal electrodes with CVD graphene. *Solid-State Electron.* **2016**, *125*, 234–239. [CrossRef]
3. Robinson, J.A.; LaBella, M.; Zhu, M.; Hollander, M.; Kasarda, R.; Hughes, Z.; Trumbull, K.; Cavalero, R.; Snyder, D. Contacting graphene. *Appl. Phys. Lett.* **2011**, *98*, 053103. [CrossRef]
4. Watanabe, E.; Conwill, A.; Tsuya, D.; Koide, Y. Low contact resistance metals for graphene based devices. *Diam. Relat. Mater.* **2012**, *24*, 171–174. [CrossRef]
5. Malec, C.E.; Elkus, B.; Davidovic, D. Vacuum-annealed Cu contacts for graphene electronics. *Solid State Commun.* **2011**, *151*, 1791–1793. [CrossRef]
6. Zhong, H.; Zhang, Z.; Chen, B.; Xu, H.; Yu, D.; Huang, L.; Peng, L. Realization of low contact resistance close to theoretical limit in graphene transistors. *Nano Res.* **2015**, *8*, 1669–1679. [CrossRef]
7. Liu, W.; Wei, J.; Sun, X.; Yu, H. A Study on Graphene—Metal Contact. *Crystals* **2013**, *3*, 257–274. [CrossRef]
8. Khomyakov, P.A.; Giovannetti, G.; Rusu, P.C.; Brocks, G.; van den Brink, J.; Kelly, P.J. First-principles study of the interaction and charge transfer between graphene and metals. *Phys. Rev. B* **2009**, *79*, 195425. [CrossRef]
9. Sakavicius, A.; Astromskas, G.; Lukša, A.; Bukauskas, V.; Nargeliene, V.; Matulaitiene, I.; Šetkus, A. Annealing Time Effect on Metal Graphene Contact Properties. *ECS J. Solid State Sci. Technol.* **2018**, *7*, M77–M81. [CrossRef]
10. Leong, W.S.; Nai, C.T.; Thong, J.T.L. What Does Annealing Do to Metal-Graphene Contacts? *Nano Lett.* **2014**, *14*, 3840–3847. [CrossRef] [PubMed]
11. Leong, W.S.; Gong, H.; Thong, J.T.L. Low-Contact-Resistance Graphene Devices with Nickel-Etched-Graphene Contacts. *ACS Nano* **2014**, *8*, 994–1001. [CrossRef] [PubMed]
12. Cheng, Z.; Zhou, Q.; Wang, C.; Li, Q.; Wang, C.; Fang, Y. Toward Intrinsic Graphene Surfaces: A Systematic Study on Thermal Annealing and Wet-Chemical Treatment of $SiO_2$-Supported Graphene Devices. *Nano Lett.* **2011**, *11*, 767–771. [CrossRef] [PubMed]
13. Lin, Y.-C.; Lu, C.-C.; Yeh, C.-H.; Jin, C.; Suenaga, K.; Chiu, P.-W. Graphene Annealing: How Clean Can It Be? *Nano Lett.* **2012**, *12*, 414–419. [CrossRef] [PubMed]
14. Chan, J.; Venugopal, A.; Pirkle, A.; McDonnell, S.; Hinojos, D.; Magnuson, C.W.; Ruoff, R.S.; Colombo, L.; Wallace, R.M.; Vogel, E.M. Reducing Extrinsic Performance-Limiting Factors in Graphene Grown by Chemical Vapor Deposition. *ACS Nano* **2012**, *6*, 3224–3229. [CrossRef] [PubMed]

15. Hong, J.; Park, M.K.; Lee, E.J.; Lee, D.; Hwang, D.S.; Ryu, S. Origin of New Broad Raman D and G Peaks in Annealed Graphene. *Sci. Rep.* **2013**, *3*, 2700. [CrossRef] [PubMed]
16. Ni, Z.H.; Wang, H.M.; Luo, Z.Q.; Wang, Y.Y.; Yu, T.; Wu, Y.H.; Shen, Z.X. The effect of vacuum annealing on graphene. *J. Raman Spectrosc.* **2010**, *41*, 479–483. [CrossRef]
17. Li, X.; Cai, W.; An, J.; Kim, S.; Nah, J.; Yang, D.; Piner, R.; Velamakanni, A.; Jung, I.; Tutuc, E.; et al. Large-Area Synthesis of High-Quality and Uniform Graphene Films on Copper Foils. *Science* **2009**, *324*, 1312–1314. [CrossRef] [PubMed]
18. Liang, X.; Sperling, B.A.; Calizo, I.; Cheng, G.; Hacker, C.A.; Zhang, Q.; Obeng, Y.; Yan, K.; Peng, H.; Li, Q.; et al. Toward Clean and Crackless Transfer of Graphene. *ACS Nano* **2011**, *5*, 9144–9153. [CrossRef] [PubMed]
19. Kaplas, T.; Bera, A.; Matikainen, A.; Pääkkönen, P.; Lipsanen, H. Transfer and patterning of chemical vapor deposited graphene by a multifunctional polymer film. *Appl. Phys. Lett.* **2018**, *112*, 073107. [CrossRef]
20. Schroder, D.K. *Semiconductor Material and Device Characterization*, 3rd ed.; John Wiley & Sons: Hoboken, NJ, USA, 2006; Chapter 1.2.
21. Ferrari, A.C.; Basko, D.M. Raman spectroscopy as a versatile tool for studying the properties of graphene. *Nat. Nanotechnol.* **2013**, *8*, 235–246. [CrossRef] [PubMed]
22. Lee, J.E.; Ahn, G.; Shim, J.; Lee, Y.S.; Ryu, S. Optical separation of mechanical strain from charge doping in graphene. *Nat. Commun.* **2012**, *3*, 1024. [CrossRef] [PubMed]
23. Li, X.; Cai, W.; Colombo, L.; Ruoff, R.S. Evolution of Graphene Growth on Ni and Cu by Carbon Isotope Labeling. *Nano Lett.* **2009**, *9*, 4268–4272. [CrossRef] [PubMed]
24. Garcia, J.M.; He, R.; Jiang, M.P.; Kim, P.; Pfeiffer, L.N.; Pinczuk, A. Multilayer graphene grown by precipitation upon cooling of nickel on diamond. *Carbon* **2011**, *49*, 1006–1012. [CrossRef]
25. Berman, D.; Deshmukh, S.A.; Narayanan, B.; Sankaranarayanan, S.K.R.S.; Yan, Z.; Balandin, A.A.; Zinovev, A.; Rosenmann, D.; Sumant, A.V. Metal-induced rapid transformation of diamond into single and multilayer graphene on wafer scale. *Nat. Commun.* **2016**, *7*, 12099. [CrossRef] [PubMed]
26. Pierson, H.O. *Handbook of Carbon, Graphite, Diamonds and Fullerenes*, 1st ed.; Noyes Publications: Park Ridge, NJ, USA, 1994; Chapter 3.
27. Baker, R.T.K. The relationship between particle motion on a graphite surface and Tammann temperature. *J. Catal.* **1982**, *78*, 473–476. [CrossRef]
28. Gromov, D.G.; Gavrilov, S.A. Manifestation of the heterogeneous mechanism upon melting of low-dimensional systems. *Phys. Solid State* **2009**, *51*, 2135. [CrossRef]
29. Kaplas, T.; Sharma, D.; Svirko, Y. Few-layer graphene synthesis on a dielectric substrate. *Carbon* **2012**, *50*, 1503–1509. [CrossRef]
30. Kaplas, T.; Matikainen, A.; Nuutinen, T.; Suvanto, S.; Vahimaa, P.; Svirko, Y. Scalable fabrication of the graphitic substrates for graphene-enhanced Raman spectroscopy. *Sci. Rep.* **2017**, *7*, 8561. [CrossRef] [PubMed]
31. Kalbac, M.; Reina-Cecco, A.; Farhat, H.; Kong, J.; Kavan, L.; Dresselhaus, M.S. The influence of strong electron and hole doping on the Raman intensity of chemical vapor-deposition graphene. *ACS Nano* **2010**, *10*, 6055–6063. [CrossRef] [PubMed]
32. Das, A.; Pisana, S.; Chakraborty, B.; Piscanec, S.; Saha, S.K.; Waghmare, U.V.; Novoselov, K.S.; Krishnamurthy, H.R.; Geim, A.K.; Ferrari, A.C.; et al. Monitoring dopants by Raman scattering in an electrochemically top-gated graphene transistor. *Nat. Nanotechnol.* **2008**, *3*, 210–215. [CrossRef] [PubMed]
33. Fu, X.-W.; Liao, Z.-M.; Zhou, J.-X.; Zhou, Y.-B.; Wu, H.-C.; Zhang, R.; Jing, G.; Xu, J.; Wu, X.; Guo, W.; et al. Strain dependent resistance in chemical vapor deposition grown graphene. *Appl. Phys. Lett.* **2011**, *99*, 213107. [CrossRef]


condensed matter

MDPI

*Article*

# Temperature Effects on the HOPG Intercalation Process

**Gianlorenzo Bussetti [1,*], Rossella Yivlialin [2], Claudio Goletti [3], Maurizio Zani [1] and Lamberto Duò [1]**

[1] Department of Physics, Politecnico di Milano, p.za Leonardo da Vinci 32, I-20133 Milano, Italy; maurizio.zani@polimi.it (M.Z.); lamberto.duo@polimi.it (L.D.)
[2] Department of Materials Science, Università Milano-Bicocca, v. R. Cozzi 55, I-20125 Milano, Italy; rossella.yivlialin@unimib.it
[3] Department of Physics, Università di Roma Tor Vergata, v. della Ricerca Scientifica 1, I-00133 Roma, Italy; goletti@roma2.infn.it
* Correspondence: gianlorenzo.bussetti@polimi.it

Received: 15 December 2018; Accepted: 10 February 2019; Published: 14 February 2019

**Abstract:** Graphite intercalation via chemical strategies is a common procedure to delaminate stratified crystals and obtain a suspension of graphene flakes. The intercalation mechanism at the molecular level is still under investigation in view of enhancing graphene production and reducing damage to the original pristine crystal. The latter, in particular, can undergo surface detriment due to both blister evolution and carbon dissolution. The role of the electrolyte temperature in this process has never been investigated. Here, by using an in-situ atomic force microscopy (AFM) apparatus, we explore surface morphology changes after the application of fast cyclic-voltammetries at 343 K, in view of de-coupling the crystal swelling phenomenon from the other electrochemical processes. We find that blisters do not evolve as a consequence of the increasing temperature, while the quality of the graphite surface becomes significantly worse, due to the formation of some adsorbates on possible defect sites of the electrode surface. Our results suggest that the chemical baths used in graphite delamination must be carefully monitored in temperature for avoiding undesired electrode detriment.

**Keywords:** temperature dependence; HOPG; anion intercalation; blister; in-situ AFM

## 1. Introduction

Graphene production requires efficient methods and procedures that can ensure a large number of high-quality flakes [1–4]. One of these methods prescribes diluted acid media [5]. Despite being more environmentally friendly than pure acids, using diluted acids results in important drawbacks, for the maintenance of the electrode, due to their water content. At potentials higher than the oxygen evolution reaction value, the anions carry water molecules inside the stratified structure of graphite [6]. As a consequence, gas evolution, which usually occurs at the electrode/electrolyte interface, also starts inside the layers underneath. The entrapped gas swells the surface and creates blisters [7,8]. Additionally, as recently observed by the authors, a carbon dissolution process affects the graphite terraces, [9]. The overall picture of the blistering process was described for the first time by Hathcock and co-workers at the middle of the 1990s [10]. Nonetheless, the intercalation mechanism at the molecular-scale level is still under investigation. The target of this new research effort lies in the possibility of driving anion intercalation by preventing the crystal detriment described above. In particular, blister evolution timing has been recently measured [9] and the electrochemical (EC) parameters that influence the graphite surface swelling have been summarized in a new blister evolution-diagram [11]. In these works, the role of both electrolyte pH and cyclic-voltammetry (CV) scan speed in promoting the graphite surface blistering at room temperature is discussed. It is worth

noting that, to the best of our knowledge, the possible effects of temperature on anion graphite intercalation and blister growth have never been considered. Some studies regarding electrodes in the cathodic regime [3], Li-batteries applications [12], Li diffusion rate in graphite [13] and intercalation [14], aging of electrodes [15], and the role of organic solvents [16] have been performed (refer to the review reported in [17] for a brief history on thermoelectrochemistry), but the role of temperature within the Hathcock model is still missing.

In this work, we apply an in-situ atomic force microscopy (AFM) apparatus to explore the highly oriented pyrolite graphite (HOPG) morphology after the application of an increasing EC potential (CV) when immersed inside a hot (namely, 343 K) acid electrolyte. The temperature value is chosen according to the maximum operation parameters of batteries that exploit graphite as electrodes [18]. We find that blister growth is not influenced by the explored temperature interval, while the graphite surface quality is significantly compromised. This result suggests that the EC bath temperature must be controlled in order to avoid chemical reactions between carbon atoms and electrolyte anions during the intercalation process.

## 2. Results and Discussion

The carbon Pourbaix diagram as a function of both pH and applied EC potential [19] is reported in Figure 1.

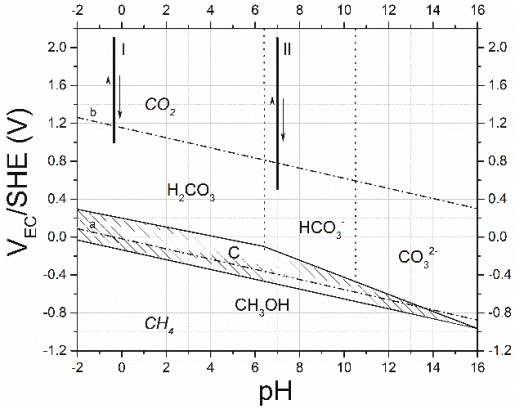


**Figure 1.** Pourbaix diagram of carbon (see text for details). The vertical black thick lines represent the scanned regions by cyclic-voltammetries (see arrows) during the preparation of the samples.

The shaded area indicates the HOPG stability region, while areas where carbon coordinates in solution with both oxygen and hydrogen (e.g., $H_2CO_3$ or $CH_3OH$, etc.), demonstrating a partial dissolution of the electrode surface, are labeled with capital letters. $CO_2$ and $CH_4$ are reported in italics, showing regions where these gases are developed. Dash-dot lines [(a) and (b)] enclose the water stability region; (a) corresponds to the lower limit (hydrogen evolution reaction, HER), while (b) indicates the upper limit (oxygen evolution reaction, OER). In the figure, we add the CV paths (vertical black lines) exploited here to prepare the samples and study the blister evolution at different conditions. The CV ($v_{scan}$ = 25 mV/s) acquired at pH = −0.3 (I) starts at a traditional value of 1.0 V and reaches the massive intercalation region at about 2.1 V [7], while the CV at pH = 7 (II), being acquired in an area where bicarbonate ions are present, starts from the open circuit value (OCP) and ends at 2.1 V. The I-CV reaches a region where, due to the solvated anion intercalation [6,10], $CO_2$ evolves both on the surface and on the graphite layers underneath. The pristine HOPG surface morphology (see Figure 2a) is then damaged by blisters that swell the uppermost graphite layers (Figure 2b).

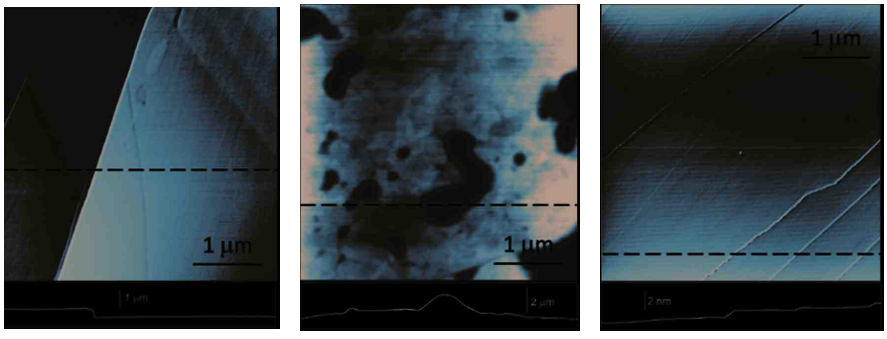


**Figure 2.** In-situ atomic force microscopy (AFM) images (**a**) of the pristine graphite, (**b**) after the I-CV and (**c**) after the II-CV.

Conversely, the surface morphology acquired in-situ after the II-CV ($v_{scan}$ = 25 mV/s) is almost unaffected (Figure 2c), despite the relatively high EC potential applied to the electrode. Apart from panel (b), where blisters damage the surface with big structures, the comparable morphology between panels (a) and (c) is also confirmed by a roughness estimation. If the latter is defined as the hill-to-valley mean distance in morphology profiles, the pristine HOPG (Figure 2a) shows a roughness of about 2 Å, like the graphite surface studied in panel (c) after the II-CV. The blister formation and growth mechanism have been widely studied and discussed [6–10]. Quite recently, the authors succeeded in describing the EC conditions required to develop blisters (evolution-diagram) at room temperature [11]. In view of observing blisters on the HOPG surface, the electrode must be kept at an EC potential above the OER value within a minimum time interval of about $\Delta t$ = 4 s [9]. As a countercheck, we have already seen that if the CV scan rate is set to $v_0$ = 600 mV/s, the I-CV is able to intercalate anions while preserving the graphite morphology [20]. In the blister-evolution diagram reported in reference 11, we observe that the CV scan rate, set at $v_0$, represents a critical condition; a slight rate reduction implies the evolution of blisters on the electrode surface. Being a border parameter, I-CV at 600 mV/s allows an analysis of the effect of temperature on the surface blistering. Generally speaking, a change in the electrolyte temperature also modifies the equilibrium conditions of the Pourbaix diagram. In particular, the oxygen reduction frontier (b-line in Figure 1) follows the Nernst equation:

$$E_{O_2/H_2O} = 1.3 - 0.06 \times \frac{T}{298} \times \text{pH} \quad (1)$$

The slope of the b-line changes as a function of the temperature, reducing (expanding) the $CO_2$ region at lower (higher) pH values with respect to 0. When the pH is (close to) zero, as in our I-CV case, the water stability upper limit is almost unaffected by temperature variations, opening the possibility to explore the role of T only in the blister chemical reactions.

With this aim, a new sample was prepared and immersed inside the electrolyte solution, whose temperature was increased up to 343 K, where the HOPG underwent a single CV scan ($v_0$ = 600 mV/s). The surface morphology, acquired in-situ, is reported in Figure 3a.

Here, sharp step edges are easily observed in close agreement with the pristine graphite (Figure 2a). No evidence of any blister is found by exploring different areas of the electrode surface. This result confirms that the key parameter in blister evolution is the time persistence of the electrode at high EC potentials. Nonetheless, a closer inspection of the HOPG surface reveals something new with respect to the analysis performed at room temperature (RT) [9] and at the same high scan rate [11]. In that case, in fact, the application of high voltages for less than $\Delta t$ = 4 s induces a carbon dissolution reaction, where graphite terraces are peeled off layer-by-layer. Here, after the CV at 343 K, terraces appear affected by adsorbates, which probably sit on defect sites, such as hollows and cracks, of the surface electrode. Adsorbates are better highlighted by the phase-contrast image reported in Figure 3b (see the

darker regions, which correspond to a drop of the phase value with respect to that one of the pristine highly oriented pyrolytic graphite) [21]. In fact, as the phase contrast is sensitive to the local chemical properties of the surface [22], we are able to highlight many discontinuities, not easily discernible in the morphology image (Figure 3a). The surface roughness is also increased with respect to the pristine HOPG by a factor of 2/2.5. We think that chemical reactions between the carbon atoms and the electrolyte anions can preferentially occur in surface hollows and cracks, where different graphite edge-planes are exposed to the hot liquid environment.

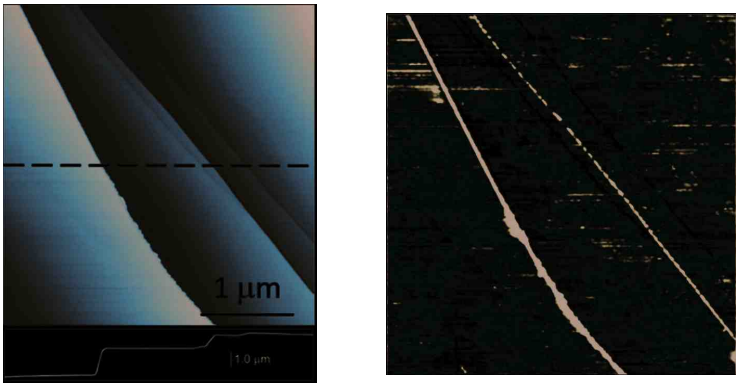


(**a**) (**b**)

**Figure 3.** (**a**) In-situ AFM image of the HOPG surface morphology after a CV at $v_0$ = 600 mV/s inside a hot (343 K) electrolyte. (**b**) Phase-contrast image of a graphite terrace. Darker regions correspond to adsorbates, which probably sit in defect sites of the electrode surface.

The overall picture that arises from data reported in Figure 3 is confirmed in each experiment performed on HOPG immersed inside a hot acid electrolyte. Nonetheless, the AFM scan is not easy in these experimental conditions; the high temperature induces a mechanical drift of the sample whose surface, due to the presence of adsorbates, can get the tip dirty, leading to a decrease in contrast decreasing and the presence of scrapes in the image. In Figure 4, for example, we report other sample scans where the phase-contrast panels always confirm the presence of adsorbates.

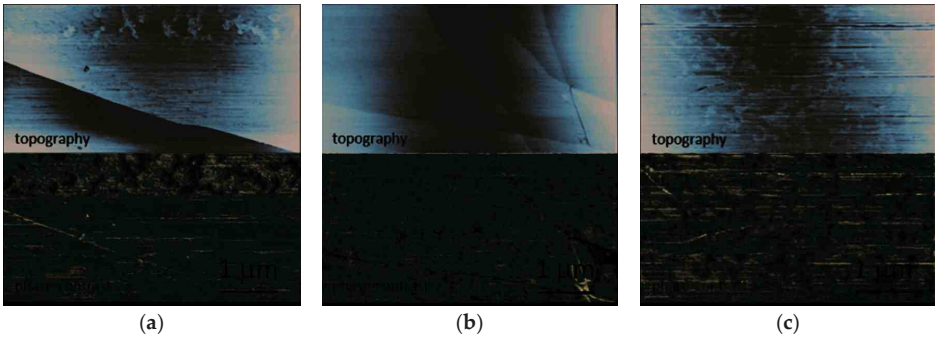


(**a**) (**b**) (**c**)

**Figure 4.** In-situ AFM images (topography and phase-contrast) of three different sample (panels **a**–**c**) scans (after a CV at $v_0$ = 600 mV/s, electrolyte at 343 K). The presence of adsorbates is enhanced by the phase-contrast images.

## 3. Materials and Methods

A z-grade HOPG (Optigraph) sample was used as the working electrode (WE). The specimen was exfoliated by an adhesive tape before each experiment. The three-electrode electrochemical cell exploits a Pt wire as both counter (CE) and reference (RE) electrode. The latter is not properly considered a reference electrode, but its stability (within few tens of millivolt) and potential shift (about 0.7 V) with respect to a standard hydrogen electrode (SHE) has been checked. All the reported EC potential values both in the text and in the figures are always referred to the SHE. The acid electrochemical solution was prepared by diluting sulfuric acid with type 1 water (Merck–Millipore). The 1 M electrochemical solutions (pH = −0.3) were purified by bubbling pure Ar gas for several hours. To change the electrolyte temperature, the WE was placed on a Peltier junction driven by a current generator. A thermocouple was immersed inside the electrolyte to monitor, in real time, the temperature changes. A Keysight 5500 in-situ AFM system was exploited in these experiments. All the images were collected in tapping mode.

## 4. Conclusions

An in-situ AFM was used to study morphological changes occurring at the graphite surface when the electrode is kept at high anodic potentials inside a hot (343 K) diluted (1 M) acid solution. Generally, when graphite reaches a potential above the oxygen evolution reaction (OER) at RT, gases are developed that swell the stratified crystal and form blisters. The role of temperature in this process has never been considered. Interestingly, we find that blistering is not affected by the temperature variation within the explored interval. Conversely, we observe many adsorbates on the graphite terraces (never reported during analysis at RT) as enhanced by the phase-contrast image, which is sensitive to local chemical changes. An explanation of the chemical origin of these compounds is desired in the future. Nonetheless, the collected results suggest to adopt a strict control of the EC cell temperature during solvated anion intercalation, in order to avoid a wide chemical detriment of the electrode surface.

**Author Contributions:** Conceptualization, G.B. and R.Y.; methodology, G.B.; investigation, R.Y.; data curation, C.G., M.Z. and L.D.; writing—original draft preparation, G.B.; writing—review and editing, C.G., M.Z. and L.D. The authors are grateful to C. Hogan (Istituto di Struttura della Materia-CNR; ISM-CNR) for useful discussions.

**Funding:** This research received no external funding.

**Conflicts of Interest:** The authors declare no conflict of interest.

## References

1. Shi, P.C.; Guo, J.P.; Liang, X.; Cheng, S.; Zheng, H.; Wang, Y.; Chen, C.H.; Xiang, H.F. Large-scale production of high-quality graphene sheets by a non-electrified electrochemical exfoliation method. *Carbon* **2018**, *126*, 507–513. [CrossRef]
2. Hofmann, M.; Chiang, W.-Y.; Nguyễn, T.D.; Hsieh, Y.-P. Controlling the properties of graphene produced by electrochemical exfoliation. *Nanotechnology* **2015**, *26*, 335607. [CrossRef] [PubMed]
3. Kamali, A.R.; Fray, D.J. Large-scale preparation of graphene by high temperature insertion of hydrogen into graphite. *Nanoscale* **2015**, *7*, 11310–11320. [CrossRef] [PubMed]
4. Nuvoli, D.; Valentini, L.; Alzari, V.; Scognamillo, S.; Bon, S.B.; Piccinini, M.; Illescas, J.; Mariani, A. High concentration few-layer graphene sheets obtained by liquid phase exfoliation of graphite in ionic liquid. *J. Mater. Chem.* **2011**, *21*, 3428–3431. [CrossRef]
5. Yang, S.; Ricciardulli, A.G.; Liu, S.; Dong, R.; Lohe, M.R.; Becker, A.; Squillaci, M.A.; Samorì, P.; Müllen, K.; Feng, X. Ultrafast Delamination of Graphite into High-Quality Graphene Using Alternating Currents. *Angewandte Chem.* **2017**, *56*, 6669–6675. [CrossRef] [PubMed]
6. Goss, C.A.; Brumfield, J.C.; Irene, E.A.; Murray, R.W. Imaging the incipient electrochemical oxidation of highly oriented pyrolytic graphite. *Anal. Chem.* **1993**, *65*, 1378–1389. [CrossRef]

7. Bussetti, G.; Yivlialin, R.; Alliata, D.; Li Bassi, A.; Castiglioni, C.; Tommasini, M.; Casari, C.S.; Passoni, M.; Biagioni, P.; Ciccacci, F.; et al. Disclosing the Early Stages of Electrochemical Anion Intercalation in Graphite by a Combined Atomic Force Microscopy/Scanning Tunneling Microscopy Approach. *J. Phys. Chem. C* **2016**, *120*, 6088–6093. [CrossRef]
8. Alliata, D.; Kötz, R.; Haas, O.; Siegenthaler, H. In Situ AFM Study of Interlayer Spacing during Anion Intercalation into HOPG in Aqueous Electrolyte. *Langmuir* **1999**, *15*, 8483–8489. [CrossRef]
9. Yivlialin, R.; Bussetti, G.; Magagnin, L.; Ciccacci, F.; Duò, L. Temporal analysis of blister evolution during anion intercalation in graphite. *Phys. Chem. Chem. Phys.* **2017**, *19*, 13855–13859. [PubMed]
10. Hathcock, K.W.; Brumfield, J.C.; Goss, C.A.; Irene, E.A.; Murray, R.W. Incipient Electrochemical Oxidation of Highly Oriented Pyrolitic Graphite: Correlation between Surface Blistering and Electrolyte Anion Intercalation. *Anal. Chem.* **1995**, *67*, 2201–2206. [CrossRef]
11. Yivlialin, R.; Magagnin, L.; Duò, L.; Bussetti, G. Blister evolution time invariance at very low electrolyte pH: $H_2SO_4$/graphite system investigated by electrochemical atomic force microscopy. *Electrochim. Acta* **2018**, *276*, 352–361. [CrossRef]
12. Rodrigues, M.-T.F.; Sayed, F.N.; Gullapalli, H.; Ajayan, P.M. High-temperature solid electrolyte interphases (SEI) in graphite electrodes. *J. Power Sources* **2018**, *381*, 107–115. [CrossRef]
13. Kulova, T.L.; Skundin, A.M.; Nizhnikovskii, E.A.; Fesenko, A.V. Temperature effect on the lithium diffusion rate in graphite. *Russ. J. Electrochem.* **2006**, *42*, 259–262. [CrossRef]
14. Levi, M.D.; Wang, C.; Aurbach, D.; Chvoj, Z. Effect of temperature on the kinetics and thermodynamics of electrochemical insertion of Li-ions into a graphite electrode. *J. Electroanal. Chem.* **2004**, *562*, 187–203. [CrossRef]
15. Leng, F.; Tan, C.M.; Pecht, M. Effect of Temperature on the Aging rate of Li Ion Battery Operation above Room Temperature. *Sci. Rep.* **2015**, *5*, 12967. [CrossRef] [PubMed]
16. Pereira-Ramos, J.-P.; Messina, R.; Piolet, C.; Devynck, J. Investigation of lithium intercalation materials with organic solvent and molten salts as electrolytes at temperatures between 60 and 175 °C. *J. Power Sources* **1987**, *20*, 221–230. [CrossRef]
17. Gründler, P. History of Modern Thermoelectrochemistry. In *In-Situ Thermoelectrochemistry. Monographs in Electrochemistry*; Springer: Berlin/Heidelberg, Germany, 2015.
18. Khateeb, S.A.; Farid, M.M.; Selman, J.R.; Al-Hallaj, S. Design and simulation of a lithium-ion battery with a phase change material thermal management system for an electric scooter. *J. Power Sources* **2004**, *128*, 292–307. [CrossRef]
19. Varcoe, J.R.; Atanassov, P.; Dekel, D.R.; Herring, A.M.; Hickner, M.A.; Kohl, P.A.; Kucernak, A.R.; Mustain, W.E.; Nijmeijer, K.; Scott, K.; et al. Anion-exchange membranes in electrochemical energy systems. *Energy Environ. Sci.* **2014**, *7*, 3135–3191. [CrossRef]
20. Jagadeesh, M.S.; Calloni, A.; Denti, I.; Goletti, C.; Ciccacci, F.; Duò, L.; Bussetti, G. The effect of cyclic voltammetry speed on anion intercalation in HOPG. *Surf. Sci.* **2019**, *681*, 111–115. [CrossRef]
21. Jagadeesh, M.S.; Bussetti, G.; Calloni, A.; Yivlialin, R.; Brambilla, L.; Accogli, A.; Gibertini, E.; Alliata, D.; Goletti, C.; Ciccacci, F.; et al. Incipient Anion Intercalation of Highly Oriented Pyrolitic Graphite Close to the Oxygen Evolution Potential: A Combined X-ray Photoemission and Raman Spectroscopy Study. *J. Phys. Chem. C* **2019**, *123*, 1790–1797. [CrossRef]
22. Bussetti, G.; Campione, M.; Riva, M.; Picone, A.; Raimondo, L.; Ferraro, L.; Hogan, C.; Palummo, M.; Brambilla, A.; Finazzi, M.; et al. Stable Alignment of Tautomers at Room Temperature in Porphyrin 2D Layers. *Adv. Funct. Mater.* **2014**, *24*, 958–963. [CrossRef]


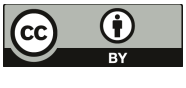

condensed matter

MDPI

*Article*

# Model of Nano-Metal Electroplating Process in Trapezoid Profile Groove

**Oksana Yu. Egorova [1,*], Victor G. Kosushkin [2,*] and Leo V. Kozhitov [2,*]**

[1] Kaluga Branch of Bauman Moscow State Technical University, Bazhenov St., 248001 Kaluga, Russia
[2] Moscow Institute of Steel and Alloys, Leninsky Prospect 2, 196036, Russia
* Correspondence: oksana.egorova95@yandex.ru (O.Y.E.); kosushkin@gmail.com (V.G.K.); kozitov@rambler.ru (L.V.K.)

Received: 26 December 2018; Accepted: 19 February 2019; Published: 21 February 2019

**Abstract:** The principle of the electrodeposition method is to immerse the coated products in a water electrolyte solution, the main components of which are salts or other soluble compounds—metal coatings. The software COMSOL Multiphysics was allowed to perform a simulation of the processes of electrodeposition of the metals copper and silver in the groove of the trapezoidal profile.

**Keywords:** electrodeposition process; group 1 metals; modeling; COMSOL Multiphysics

## 1. Introduction

The process of electrodeposition of metals is important in micro- and nano-electronics, as it is used in the production of multilayer printed circuit boards (MPC). MPCs consist of many layers, most of which are complex electrical circuits. The formation of interlayer compounds is an important technological task and, as a rule, is carried out with the help of through metallized holes [1]. The manufacture of transition holes with diameters of less than 300 microns with the help of various metallized pastes is complicated by the difficulties of free penetration of the paste into the hole and the air out of it. The simplicity, availability, and technological capabilities of the electrodeposition process make it possible to use it for local electrochemical deposition, especially with an unchanged decrease in topological dimensions. Electrodeposition is a complex process occurring at the interface of type 1 and 2 conductors and depends on various factors such as temperature, mixing rate, and electrolyte composition, as well as ion solvation processes, adsorption at the phase boundary, the state of the double electric layer, the phenomena of electrode polarization, diffusion, and convection flows near the deposition surface. However, the process of local metallization is affected by a complex surface relief.

In some cases, mathematical modeling methods can replace a full-scale experiment, saving material and time costs. In this article, we consider the possibility of mathematical modeling of electrochemical deposition of copper and silver under local metallization in a hollow trapezoidal profile groove using the basic package of COMSOL Multiphysics.

## 2. The Process of Electrodeposition

The principle of the electrodeposition method is to immerse the coated products in an aqueous electrolyte solution. The main components are salts or other soluble compounds called metal plating. The coated products are in contact with the negative pole of the direct current source, i.e., the cathode. A plate made of a deposited metal or an inert electrically conductive material, such as graphite, is used as the anode. It is in contact with the positive pole of the direct current source and dissolves when the flow of electric current, compensating for the decrease of ions, is discharged on the coated products [2]. The reduction of cations on the cathode leads to the release of a metal layer on the negative surface of the cathode. As a result, a metal film with a fine-crystalline, coarse-crystalline, shiny, or matte surface

structure can be formed on the cathode. The deposition of metal atoms begins at the crystallization centers, the number of which is determined by the amount of overvoltage at the cathode. Defects in the structure of the substrate influence the nucleation process, and then they move along the surface to the fractures, forming a film. Thus, the film develops into islands that grow in all directions until they merge [3].

## 3. Modeling the Process of Electroplating Metals of the 1st Group in a Trapezoid Profile Groove Using the Software COMSOL Multiphysics

The deposition of metals in the trapezoid profile groove is an example of the modeling of the electrodeposition process in the COMSOL Multiphysics program. The standard model Copper Deposit in a Trench was taken as a basis [4].

In this paper, we used a trapezoidal profile groove to show how the electrodeposition process proceeds depending on the change in form and composition.

The geometry of the model is shown in Figure 1. The upper horizontal boundary is the anode, and the trapezoidal cathode is located at the bottom.

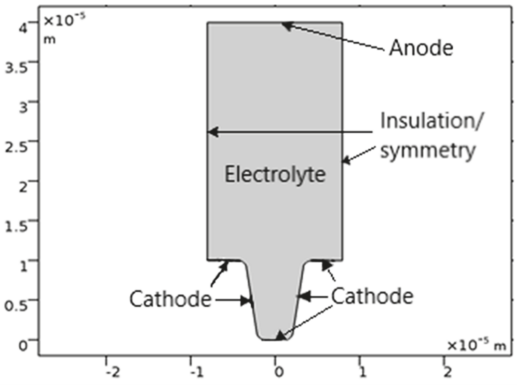


**Figure 1.** The geometry of the model.

The vertical walls on the main electrode are considered isolated:

$$N_i \times n = 0 \tag{1}$$

The flow for each of the ions in the electrolyte is determined by the Nernst–Planck equation:

$$N_i = -D_i \nabla c_i - z_i u_i F c_i \nabla \varphi_i \tag{2}$$

where $N_i$ is the ion flow (mol/m$^2$·s), $c_i$ is the ion concentration in the electrolyte (mol/m$^3$), $z_i$ is the charge of the ion particles, $u_i$ is themobility of charged particles (m$^3$/s·J·mol), $F$ is theFaraday constant (As/mol) is the potential in the electrolyte (V).

This equation allows us to calculate the distribution of copper ion concentrations, isopotential lines, current density lines, and displacements of the cathode and anode surfaces after 12, 14, 16, and 20 s of operation, which are shown in Figure 2.

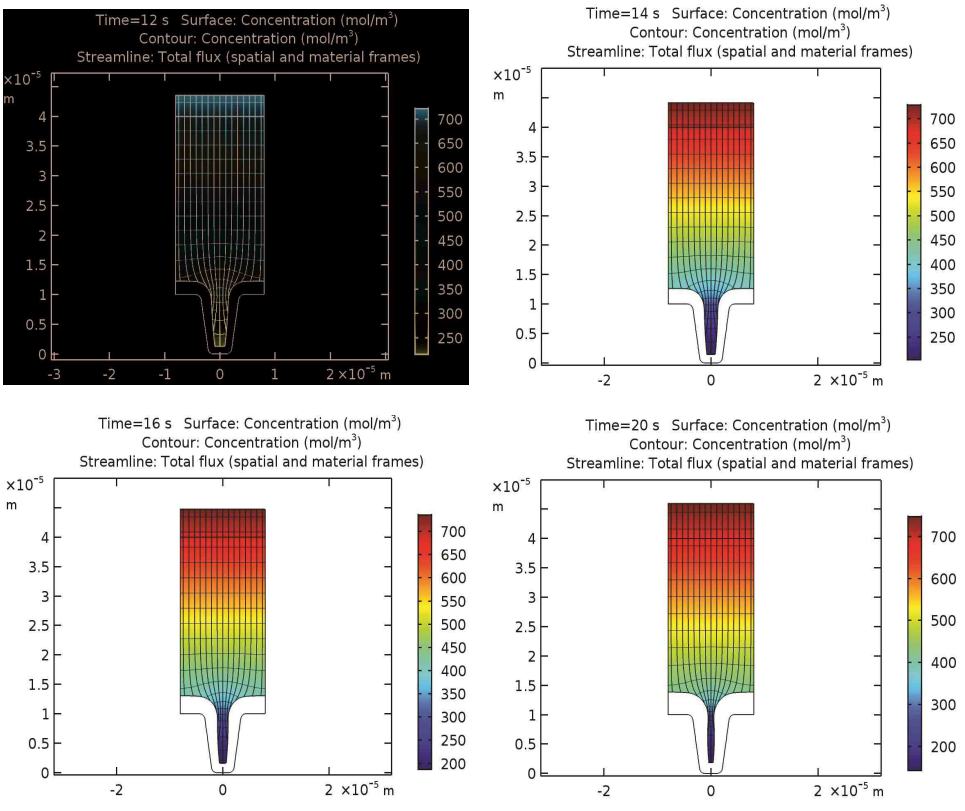


**Figure 2.** Concentrations of copper ions (mol/m$^3$), isopotential lines, current density lines, and electrode displacement in the cell after 12, 14, 16, and 20 s of work.

Lines of layer thickness show the development of non-uniform deposition of a copper layer due to the non-uniform distribution of current density from the bottom to the upper edge of the groove. This effect is directly related to the decrease in the concentration of copper ions in the depth of the cavity.

From this, it can be concluded that with an increase in the duration of the process, the groove hole on the upper edge begins to taper, and its overgrowth is possible due to the non-uniform deposition thickness. Therefore, for copper deposition, the optimal process duration is 14 s.

An analogical modeling was performed for the silver deposition on the surface of the trapezoidal profile.

Figure 3 shows the distribution of the concentration of silver ions, isopotential lines, current density lines, and the displacement of the cathode and anode surface after 12, 14, 16, and 20 s of operation.

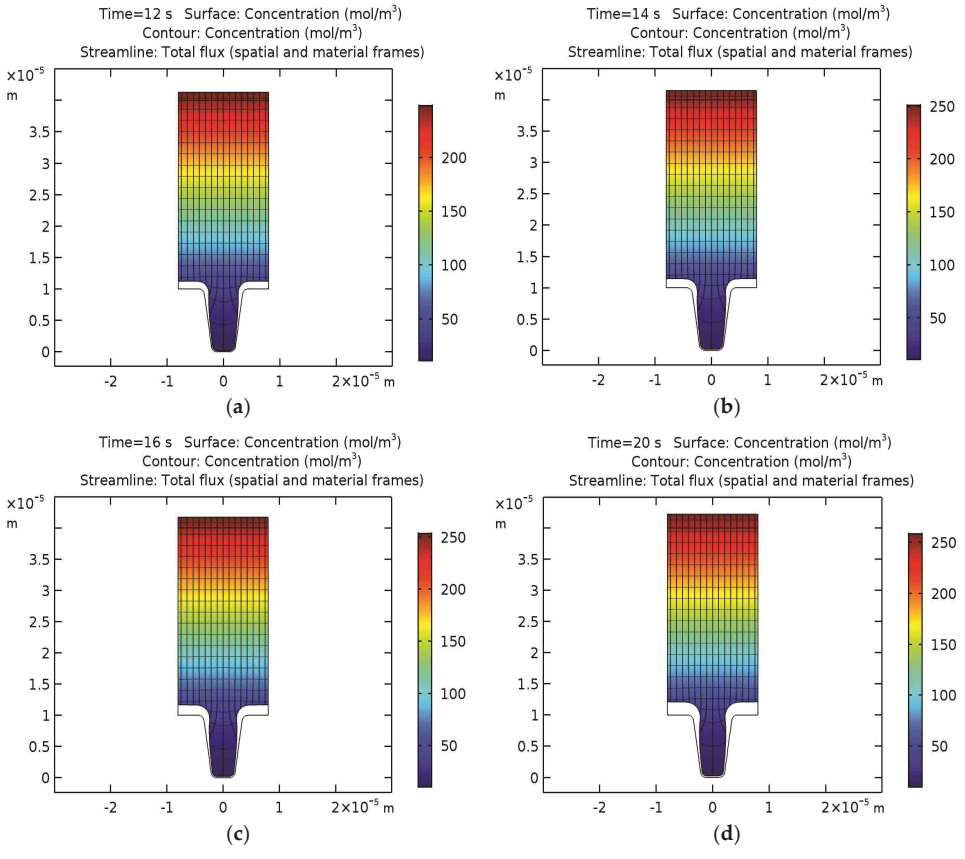


**Figure 3.** Concentrations of silver ions (mol/m$^3$), isopotential lines, current density lines, and electrode displacement in the cell after 12, 14, 16, and 20 s of operation.

It can be concluded that with an increase in the duration of the process, the cavity hole begins to narrow gradually due to the non-uniform thickness of the deposited layer, but differs significantly compared to the results for copper. The process of narrowing is slower, which may be associated with a lower initial concentration of silver. In this case, the optimal duration of the silver deposition process is 20 s.

Thus, the modeling of copper and silver deposition processes allows us to obtain preliminary data on the formation of the topology of contacts at the local metallization on the surface of printed circuit boards and other electronics products, without resorting to full-scale experiments.

## 4. Conclusion

The software COMSOL Multiphysics allowed us to perform the modeling of the processes of copper and silver electrodeposition in the trapezoidal profile groove.

The results obtained for the thicknesses of the deposited layers of copper and silver can optimize the deposition regimes. For example, it is advisable to carry out metal deposition in a periodic mode, changing the polarity of the electrode to the opposite. This should ensure the alignment of the concentration of metal ions in the depth of the groove, and thus reduce the thickness variation of the layers on the vertical walls.

**Author Contributions:** V.G.K. and L.V.K. provided the necessary theoretical materials, O.Y.E. performed experiments and analyzed data.

**Funding:** This research received no external funding.

**Conflicts of Interest:** The authors declare no conflict of interest.

## References

1. Tyulkova, A.A. Electrolytes for the electroplating of 3D micro-transitions. In Proceedings of the All-Russian Scientific and Technical Conference, Moscow, Russia, 7–10 April 2015; Available online: http://studvesna.ru/?go=articles&id=1270 (accessed on 28 September 2018).
2. Dzidziguri, E.; Ryzhonkov, D.I.; Levina, V.V. *Nanomaterials Tutorial Nanomaterialy Uchebnoe Posobie*; BINOM Knowledge Laboratory: Moscow, Russia, 2010.
3. Belenky, M.A.; Ivanov, A.F. *Electrodeposition of Metallic Coatings*; Metallurgy: Moscow, Russia, 1985; p. 288.
4. The COMSOL® Software Product Suite. Available online: https://www.comsol.com/products (accessed on 17 September 2018).

condensed matter

MDPI

*Article*

# Electronic Structure of Boron Flat Holeless Sheet

**Levan Chkhartishvili [1,2,3,*], Ivane Murusidze [4] and Rick Becker [3]**

1 Engineering Physics Department, Georgian Technical University, 77 Kostava Ave., Tbilisi 0175, Georgia
2 Boron and Composite Materials Laboratory, Ferdinand Tavadze Institute of Metallurgy and Materials Science, 10 Mindeli Str., Tbilisi 0186, Georgia
3 Boron Metamaterials, Cluster Sciences Research Institute, 39 Topsfield Rd., Ipswich, MA 01938, USA; rbecker@clustersciences.com
4 Institute of Applied Physics, Ilia State University, 3/5 Cholokashvili Ave., Tbilisi 0162, Georgia; miv@iliauni.edu.ge
* Correspondence: levanchkhartishvili@gtu.ge or chkharti2003@yahoo.com

Received: 30 January 2019; Accepted: 26 February 2019; Published: 3 March 2019

**Abstract:** The electronic band structure, namely energy band surfaces and densities-of-states (DoS), of a hypothetical flat and ideally perfect, i.e., without any type of holes, boron sheet with a triangular network is calculated within a quasi-classical approach. It is shown to have metallic properties as is expected for most of the possible structural modifications of boron sheets. The Fermi curve of the boron flat sheet is found to be consisted of 6 parts of 3 closed curves, which can be approximated by ellipses representing the quadric energy-dispersion of the conduction electrons. The effective mass of electrons at the Fermi level in a boron flat sheet is found to be too small compared with the free electron mass $m_0$ and to be highly anisotropic. Its values distinctly differ in directions Γ–K and Γ–M: $m_{\Gamma-K}/m_0 \approx 0.480$ and $m_{\Gamma-M}/m_0 \approx 0.052$, respectively. The low effective mass of conduction electrons, $m_\sigma/m_0 \approx 0.094$, indicates their high mobility and, hence, high conductivity of the boron sheet. The effects of buckling/puckering and the presence of hexagonal or other type of holes expected in real boron sheets can be considered as perturbations of the obtained electronic structure and theoretically taken into account as effects of higher order.

**Keywords:** boron sheet; electronic structure; density-of-states (DoS); Fermi curve; effective mass

## 1. Introduction

Borophene—a one-atom-thick sheet of boron—is one of the most promising nanomaterials [1]. Most all-boron quasi-planar clusters and nanosurfaces, including nanosheets, constructed of triangular atomic rings, which Ihsan Boustani et al. predicted theoretically in 1994 and the following years (quasi-planar clusters [2], nanotubes [2–5], nanotube-to-sheet transitions [6], and sheets [5,7]), are now experimentally confirmed (quasi-planar clusters [8–10], nanotubes [11–13], nanotube-to-sheet transitions [14,15], and sheets [16,17]).

### *1.1. Why should Boron Sheets be Formed?*

There are different reasons in favor of the formation of stable 2-D all-boron structures. They can be divided into several groups. Let's consider them separately.

#### 1.1.1. 3-D All-Boron Structures

Boron, the fifth element of the Periodic Table, is located at the intersection of semiconductors and metals. Due to a small covalent radius (only 0.84 Å) and number (only 3) of valence electrons, boron does not form simple three-dimensional structures but crystals with icosahedral clusters with many atoms in the unit cell. At least three all-boron allotropes are known—α- and β-rhombohedral and

high-pressure γ-orthorhombic phases—for the experimental phase diagram of boron see Reference [18]. In addition, α- and β-tetragonal and a number of other boron structures, probably stabilized by the presence of impurities/defects, were reported. Theoretical studies of the five boron crystal structures (α, dhcp, sc, fcc, and bcc) were carried out using the LAPW (linearized plane wave) method in Reference [19]. The current state of research on the phase diagram of boron from a theoretical point of view is given in Reference [20]. It should be noted that, in the last decade, several new structures of boron allotropes were discovered and some have been disproved. Currently, even the number of allotropes of boron is uncertain. The reason for this is that there are many such structures, all of them complex, and some of them are minimally different from others. A pseudo-cubic tetragonal boron recently discovered under high-pressure and high-temperature conditions may also be another form of boron allotropes; however, its structure, studied in Reference [21] using a DFT (density functional theory) calculation, is abnormal compared to other allotropes of boron in many ways.

The almost regular icosahedron $B_{12}$ with B-atoms at the vertices (Figure 1) serves as the main structural motif not only of boron allotropes but also of all known boron-rich compounds. In the boron icosahedron, each atom is surrounded by 5 neighboring atoms and, as usual, with one more atom from the rest of the crystal. For this reason, the average coordination number of a boron-rich lattice ranges from 5 to 5+1=6.

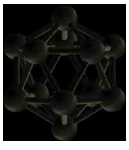

**Figure 1.** A regular icosahedron $B_{12}$ with B-atoms at the vertices.

However, an isolated regular boron icosahedron is an electron-deficient structure—the total number of valence electrons of 12 boron atoms is not sufficient to fill all the covalent bonding orbitals corresponding to such a cage-molecule. Thus, if it were a stable structure, then intra-icosahedral bonds would be only partially covalent but also to some extent metallic. As for boron icosahedra constituting real crystals, it was clearly demonstrated, for example, for β-rhombohedral boron [22–27], that they are stabilized by the presence of point structural defects—vacancies and interstitials, in other words, both partially filled regular or irregular boron sites—at very high concentrations. For example, in the case of β-rhombohedral boron, the total effect of such a stabilization is to increase the average number of boron atoms inside the unit cell from the ideal value 105 (Figure 2) to 106.7 [28], which leads to the saturation of the electron-deficient orbitals and a 5- or 6-coordination number for the majority of constituent boron atoms.

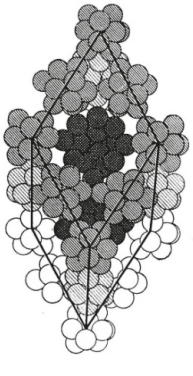

**Figure 2.** An idealized unit cell of a β-rhombohedral boron crystal.

Thus, all-boron 5- and 6-coordinated regular 3-D lattices cannot exist, but one can naturally imagine 2-D flat or buckled/puckered structures with a triangular arrangement of atoms with and without periodically spaced hexagonal (rarely quadric, pentagonal, or heptagonal) holes. Obviously, most of them are expected to be (semi)metallic. At the moment, a number of different atomic geometries for quasi-planar boron sheets are theoretically proposed [4–7,29–51].

Using the ab initio evolutionary structure prediction approach, a novel reconstruction of the $\alpha$-boron (111) surface with the lowest energy was discovered [52]. In this reconstruction, all single interstitial boron atoms bridge neighboring icosahedra by polar covalent bonds, and this satisfies the electron counting rule, leading to the reconstruction-induced semiconductor–metal transition. The new stable boron sheet, called H-borophene, proposed in Reference [53] and constructed by tiling 7-membered rings side by side, should be especially noted.

As for the irregularly distributed holes, they have to be considered as defects. The research [54] is focused on the formation of local vacancy defects and pinholes in a 2-D boron structure—the so-called $\gamma_3$-type boron monolayer.

#### 1.1.2. Boron Quasi-Planar Clusters

Indirectly, the reality of boron sheets can be proved by the presence of various quasi-planar boron clusters, i.e., finite fragments of sheets, in gaseous state and also boron nanotubes, which are the fragments of boron sheets wrapped into cylinders (see for example, the review from Reference [55] and the references therein). Experimental and theoretical evidences that small boron clusters prefer planar structures were reported in Reference [8].

In addition, recently, a highly stable quasi-planar boron cluster $B_{36}$ of hexagonal shape with a central hexagonal hole [9], which is viewed as a potential basis for an extended 2-D boron sheet, and boron fullerene $B_{40}$ [10], which can be imagined as the fragment of a boron sheet wrapped into the sphere, were discovered experimentally. Photoelectron spectroscopy in combination with ab initio calculations have been carried out to probe the structure and chemical bonding of the $B_{27}^-$ cluster [56]. A comparison between the experimental spectrum and the theoretical results reveals a 2-D global minimum with a triangular lattice containing a tetragonal defect and two low-lying 2-D isomers, each with a hexagonal vacancy.

#### 1.1.3. Liquid Boron Structure

There are also evidences [57–59] that liquid boron does not consist of icosahedra but mainly of quasi-planar clusters. Ab initio MD (molecular-dynamics) simulations of the liquid boron structure yields that at short length scales, $B_{12}$ icosahedra, a main structural motif of boron crystals and boron-rich solid compounds, are destroyed upon melting. Although atoms form an open packing, they maintain the 6-coordination.

According to measurements of the structure factor and the pair distribution function, the melting process is associated with relatively small changes in both the volume and the short-range order of the system. Results of a comprehensive study of liquid boron with X-ray measurements of the atomic structure and dynamics coupled with ab initio MD simulations also show that there is no evidence of survival of the icosahedral arrangements into the liquid, but many atoms appear to adopt a geometry corresponding to the quasi-planar pyramids.

#### 1.1.4. Growing of Boron Sheets

Currently, some of the 2-D materials beyond graphene also are used [60]. But for non-layer structured 3-D materials such as boron, it is a real challenge to fabricate the corresponding 2-D nanosheets due to the absence of the driving force of anisotropic growth. There are rare examples of some 2-D metal nanosheets; see for example, the recent report [61] on single-crystalline Rh nanosheets with a 3–5 atomic layers thickness. Boron sheets are expected to be metallic as well. Thus, this should increase the chances of their actual formation.

In this regard, we have to mention the recent report [62] in which large-scale single-crystalline ultrathin boron nanosheets have been fabricated via the thermal decomposition of diborane.

It is obvious that an infinite boron sheet does not exist in nature and that its finite pieces are not stable compared to bulk and/or nanotubular structures of boron. To grow boron sheets, one needs a substrate which binds boron atoms strongly to avoid bulk phases while, at the same time, provides sufficient mobility of boron atoms on the substrate. Possible candidates for substrates are surfaces of (close-packed transition) metals. The feasibility of different synthetic methods for 2-D boron sheets was assessed [47,63–66] using ab initio calculations, i.e., "synthesis in theory" approach. A large-scale boron monolayer has been predicted with mixed hexagonal-triangular geometry obtained via either depositing boron atoms directly on the surface or soft landing of small planar B-clusters.

Recently, a series of planar boron allotropes with honeycomb topology has been proposed [67]. Although the free-standing honeycomb B allotropes are higher in energy than α-sheets, these calculations show that a metal substrate can greatly stabilize these new allotropes.

The atomically thin, crystalline 2-D boron sheets, i.e., borophene, were actually synthesized [16] on silver surfaces under ultrahigh-vacuum conditions (Figure 3). An atomic-scale characterization, supported by theoretical calculations, revealed structures reminiscent of fused boron clusters with multiple scales of anisotropic, out-of-plane buckling. Unlike bulk boron allotropes, borophene shows metallic characteristics that are consistent with predictions of a highly anisotropic 2-D metal.

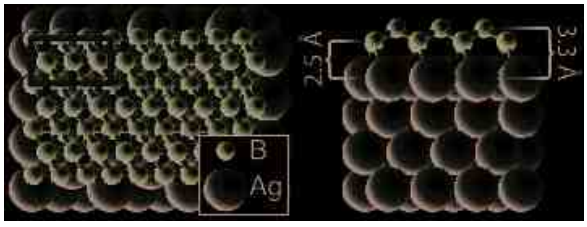


**Figure 3.** The borophene structure on a silver substrate: the top and side views of the monolayer structure (unit cell indicated by the box) [16].

The experimental work in Reference [17] shows that 2-D boron sheets can be grown epitaxially on a Ag(111) substrate. Two types of boron sheets, $\beta_{12}$ and $\chi_3$, both exhibiting a triangular lattice but with different arrangements of periodic holes, were observed by scanning tunneling microscopy. DFT simulations indicate that both sheets are planar without obvious vertical undulations.

According to the ab initio calculations [68], the periodic nanoscale 1-D undulations can be preferred in borophenes on concertedly reconstructed Ag(111). This "wavy" configuration is more stable than its planar form on flat Ag(111) due to an anisotropic high bending flexibility of borophene. An atomic-scale ultrahigh vacuum scanning tunneling microscopy characterization of a borophene grown on Ag(111) reveals such undulations, which agree with the theory. Although the lattice is coherent within a borophene island, the undulations nucleated from different sides of the island form a distinctive domain boundary when they are laterally misaligned.

Recently, borophene synthesis monitored in situ by low-energy electron microscopy, diffraction, and scanning tunneling microscopy and modeled using ab initio theories has been reported in Reference [69]. By resolving the crystal structure and phase diagram of borophene on Ag(111), the domains are found to remain nanoscale for all growth conditions. However, by growing borophene on Cu(111) surfaces, large single-crystal domains (up to 100 μm) are obtained. The crystal structure is a novel triangular network with a concentration of hexagonal vacancies of $\eta = 1/5$. These experimental data together with ab initio calculations indicate a charge-transfer coupling to the substrate without significant covalent bonding.

Boron on a Pb(110) surface was simulated [70] by using ab initio evolutionary methodology and found that 2-D *Pmmn* structures can be formed because of a good lattice matching. By increasing the

thickness of 2-D boron, the three-bonded graphene-like $P2_1/a$ boron was revealed to possess lower molar energy, indicating the more stable 2-D boron.

The influence of the excess negative charge on the stability of borophenes—2-D boron crystals—was examined in Reference [71] using an analysis of the decomposition of the binding energy of a given boron layer into contributions coming from boron atoms that have different coordination numbers to understand how the local neighborhood of an atom influences the overall stability of the monolayer structure. The decomposition is done for the $\alpha$-sheet related family of structures. It was found a preference for 2-D boron crystals with very small or very high charges per atom. Structures with intermediate charges are not energetically favorable. It has been also found a clear preference in terms of binding energy for the experimentally observed $\gamma$-sheet and $\delta$-sheet structures that is almost independent on the considered excess of negative charge of the structures.

Two-dimensional boron monolayers have been extensively investigated using ab initio calculations [72]. A series of boron bilayer sheets with pillars and hexagonal holes have been constructed. Many of them have a lower formation energy than an $\alpha$-sheet boron monolayer. However, the distribution and arrangement of hexagonal holes can cause a negligible effect on the stability of these structures.

Recently, an ab initio study [73] of the effect of electron doping on the bonding character and stability of borophene for the neutral system has revealed previously unknown stable 2-D structures: $\varepsilon$-B and $\omega$-B. The chemical bonding characteristic in this and other boron structures is found to be strongly affected by an extra charge. Beyond a critical degree of electron doping, the most stable allotrope changes from $\varepsilon$-B to a buckled honeycomb structure. Additional electron doping, mimicking a transformation of boron to carbon, causes a gradual decrease in the degree of buckling of the honeycomb lattice.

### *1.2. Applications*

In general, the formation of a boron sheet would have wide applications in techniques because the boronizing of metal surfaces is known as an effective method of formation of protective coatings [74]. In particular, quasi-planar bare boron surfaces can serve as lightweight protective armor.

Boron sheets are expected to be very good conductors with potential applications in nanoelectronics, e.g., in high-temperature nanodevices. Boron sheets could have potential as metallic interconnects and wiring in electronic devices and IC (integrated circuits) [41].

A theoretical investigation [32] of both the molecular physisorption and dissociative atomic chemisorption of hydrogen by boron sheets predicts physisorption as the leading mechanism at moderate temperatures and pressures. Further calculations performed on hydrogen-storage properties showed that the decoration of pristine sheets with the right metal elements provide additional absorption sites for hydrogen [47]. Thus, boron sheets can serve for good nanoreservoirs of fuel hydrogen used in green-energy production.

Due to the high neutron-capture cross section of $^{10}$B nuclei, solid-state boron allotropies, as well as boron-rich compounds and composites, are good candidates to be used as neutron-protectors. Boron sheets will be especially useful as an absorbing component in composite neutron shields [75]. Materials with the high bulk concentration of B-atoms usually are nonmetals and, therefore, not suitable for electromagnetic shielding purposes. However, frequently, the simultaneous protection against both the neutron irradiation and electromagnetic waves is needed, in particular, because neutron absorption by $^{10}$B nuclei is accompanied by a gamma-radiation. For this reason, in the boron-containing nanocomposites designed for neutron-protection, it is necessary to introduce some foreign components with metallic conductivity. Utilizing of the metallic boron sheet as a component may resolve this problem [76].

Recently, the mechanical properties of 2-D boron—borophene—have been studied by ab initio calculations [77]. The borophene with a 1/6 concentration of hollow hexagons is shown to have the Föppl–von Kármán number per unit area over twofold higher than graphene's value. The record high

flexibility combined with excellent elasticity in boron sheets can be utilized for designing advanced composites and flexible devices. The transfer of undulated borophene onto an elastomeric substrate would allow for high levels of stretchability and compressibility with potential applications for emerging stretchable and foldable devices [68].

The boron sheets are quite inert to oxidization and interact only weakly with their substrate. For this reason, they may find applications in electronic devices in the future [17].

In large-scale single-crystalline ultrathin boron nanosheets fabricated [62] via the thermal decomposition of diborane, the strong combination performances of low turn-on field-of-field emissions, favorable electron transport characteristics, high sensitivity, and fast response time to illumination reveal that the nanosheets have high potential as applications in field-emitters, interconnects, IC, and optoelectronic devices.

Some other applications of borophene are described in recent reviews [78,79].

### *1.3. Available Electron Structure Calculations*

Because boron sheets are of great academic and practical interests, their electronic structure is studied intensively. Most of them are found to be metallic.

Let us note that there are some indirect evidences for metallic conduction in boron sheets. The absence of icosahedra in liquid boron affects its properties including electrical conductivity [57,59], and it behaves like a metal.

The very stable quasi-planar clusters of boron $B_n$ for $n$ up to 46, considered to be fragments of bare boron quasi-planar surfaces, have to possess a singly occupied bonding orbital [29]. Assuming that conduction band of the infinite surface is generated from the HOMO (highest-occupied-molecular-orbital) of a finite fragment, it means the partial filling of the conduction band, i.e., the metallic mechanism of conductance.

Diamond-like, metallic boron crystal structures were predicted in Reference [80] employing so-called decoration schemes of calculations, in which the normal and hexagonal diamond-like frameworks are decorated with extra atoms across the basal plane. They should have an overly high DoS near the Fermi level. This result may provide a plausible explanation for not only the anomalous superconductivity of boron under high pressure but also the nonmetal–metal transition in boron structures.

In Reference [45], it was presented the results of a theoretical study of the phase diagram of elemental boron showing that, at high pressures, boron crystallizes in quasi-layered bulk phases characterized by in-plane multicenter bonds and out-of-plane bonds. All these structures are metallic.

Usually, direct ab initio calculations performed for boron sheets of different structures reveal the pronounced metallic-like total DoSs [4,5,7,30,31,35,38,40,41,44,46,64], and therefore, boron sheets show a strongly conducting character.

Band structures of a series of planar boron allotropes with honeycomb topologies recently proposed in Reference [67], exhibit Dirac cones at the K-point, the same as in graphene. In particular, the Dirac point of honeycomb boron sheet locates precisely on the Fermi level, rendering it as a topologically equivalent material to graphene. Its Fermi velocity is of $6{\cdot}10^5$ m/s, close to that of graphene. However, in H-borophene [53] constructed by tiling 7-membered rings side by side, a Dirac point appeared at about 0.33 eV below the Fermi level.

According to some theoretical results [36,37,47,48], boron sheets can be not only metal but in some cases also an almost zero band-gap semiconductor depending on its atomistic configuration. Probably, the semiconducting character is related to the nonzero thickness of buckled/puckered 2-D boron sheets or double-layered structures.

Some of borophenes can be magnetic. Based on a tight-binding model of 8-*Pmmn* borophene developed in Reference [81], it is confirmed that the crystal hosts massless Dirac fermions and the Dirac points are protected by symmetry. Strain is introduced into the model, and it is shown to induce a pseudomagnetic field vector potential and a scalar potential. The 2-D antiferromagnetic boron,

designated as M-boron, has been predicted [82] using an ab initio evolutionary methodology. M-boron is entirely composed of $B_{20}$ clusters in a hexagonal arrangement. Most strikingly, the highest valence band of M-boron is isolated, strongly localized, and quite flat, which induces spin polarization on either cap of the $B_{20}$ cluster. This flat band originates from the unpaired electrons of the capping atoms and is responsible for magnetism. M-boron is thermodynamically metastable.

Boron sheets grown on metal surfaces are predicted [63] to be strongly doped with electrons from the substrate, showing that a boron sheet is an electron-deficient material. As mentioned, by simulating [70] boron on Pb(110) surface using ab initio evolutionary methodology, it was found that the 2-D Dirac *Pmmn* boron can be formed. Unexpectedly, by increasing the thickness of 2-D boron, the three-bonded graphene-like structure $P2_1/a$ was revealed to possess double anisotropic Dirac cones. It is the most stable 2-D boron with particular Dirac cones. The puckered structure of $P2_1/a$ boron results in the peculiar Dirac cones.

This present work aims to provide more detailed calculations on the electronic structure of boron sheet including not only DoS but also band structure, electron effective mass, Fermi curve, etc.

## 2. Theoretical Approach

We use an original theoretical method of the quasi-classical type [83] based on the proof that the electronic system of any substance is a quasi-classical system; that is, its exact and quasi-classical energy spectra are close to each other.

This approach successfully was applied to all-boron structures to determine their structural parameters, binding energy, vibrational frequencies, and isotopic effects as well; see for example, References [84–88].

As for the determination of the materials' electron structure, the quasi-classical method is reduced to the LCAO (linear combination of atomic orbitals) method with a basis set of quasi-classical atomic orbitals. Within the initial quasi-classical approximation, the solution of the corresponding mathematical problem consists of two main stages:

1. The construction of matrix elements for secular equation, which, within the initial quasi-classical approximation, reduces to a geometric task of determining the volume of the intersection of three spheres [89], and
2. The solving of the secular equation, which determines the crystalline electronic energy spectrum [90].

This method has been successfully applied to electronic structure calculations performed for various modifications of boron nitride, BN, one of the most important boron compounds [91–94], as well as metal-doped β-rhombohedral boron [95].

The maximal relative error of a quasi-classical calculation itself, i.e., without errors arisen from input data, is estimated as approx. 4%.

As for the input data, the quasi-classical method of band structure calculations requires them to be in the form of quasi-classical parameters of constituent atoms: the inner and outer radii of the classical turning points for electron states in atoms, the radii of layers of the quasi-classical averaging of potential in atoms, and the averaged values of the potential within corresponding radial layers of atoms. These quantities for an isolated boron atom (as well as for other atoms) in the ground state were pre-calculated in Reference [96] on the basis of ab initio theoretical, namely Hartree–Fock (HF), values of electron levels [97]. Thus, in our case, the accuracy of the quasi-classical parameters is determined by that of the HF approach.

As is known, the electronic structure of any atomic system is influenced by its geometric structure and vice versa. Often, one starts with the question of how to find the most stable idealized atomic configuration. Despite this, here, we will directly begin with the electron band structure of a flat triangular boron sheet, neglecting the buckling/puckering effects and hexagonal holes (see references above), assuming that in real sheets (e.g., grown on metal surfaces), their buckled/puckered or vacant

parts would not be arranged in a periodic manner, and thus, they should be regarded as perturbations which can be taken into account within a higher-order perturbation theory.

Multi-layered (buckled) boron sheets can be imagined by substituting metal Me atoms again with boron B atoms in the layered structure of a metal boride $MeB_2$. Analyses of the isolated layer instead of multilayered structure also seems to be quite sufficient for the initial approximation because, in such structures, only intra-layer conductivity is metallic, while interlayer conductivity is nonmetallic due to larger interlayer bond lengths if compared with those in layers.

The 2-D unit cell of the perfectly flat boron sheet without hexagonal holes (Figure 4) is a rhomb with an acute angle of $\beta = \pi/3$, i.e., with a single lattice constant $a$ (Figure 5). Let $\vec{a}_1$ and $\vec{a}_2$ be lattice vectors, $a_1 = a_2 = a$. Then, the radius-vectors of the lattice sites are $n_1\vec{a}_1 + n_2\vec{a}_2$ with $n_1, n_2 = \ldots, -3, -2, -1, 0, +1, +2, +3, \ldots$. Vectors $\vec{k}_1$ and $\vec{k}_2$ of a reciprocal lattice (Figure 6) have to be determined from the relations $\vec{k}_1 \perp \vec{a}_2$, $\vec{k}_2 \perp \vec{a}_1$, and $k_1 = k_2 = 4\pi/\sqrt{3}a$. There is a number of different values for the lattice constant of a boron sheet suggested theoretically. For the self-consistency of calculations, we use $a = 3.37$ a.u. of length, i.e., 1.78 Å, which corresponds to the B–B pair interatomic potential in the same quasi-classical approximation [91].

**Figure 4.** A boron perfect flat sheet without hexagonal holes.

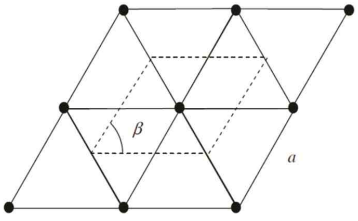


**Figure 5.** A 2-D rhombic unit cell of a boron flat sheet.

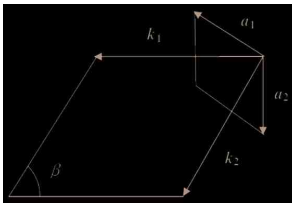


**Figure 6.** The vectors of a reciprocal lattice of a boron flat sheet.

Into the basis set of a simple LCAO formalism, it has been included core (1*s*), fully (2*s*), and partially filled (2*p*) valence and empty excited (2*p*) atomic orbitals.

Experimentally, there are 10 detected different existing states in the boron atom. To minimize the calculation errors related to the approximation of the crystalline potential by the superposition of atomic potentials, we choose orbitals with the same symmetry as the partially filled valence orbital, i.e., 2*p*, with the closest energy level and, consequently, with the closest classical turning point radii of electrons.

Taking into account the degeneracy of atomic energy levels by magnetic and spin quantum numbers of 2, 2, 6, and 6, respectively, we can state that this set of 4 orientation-averaged orbitals replaces 16 angularly dependent atomic orbitals.

The secular equation takes the form

$$\det(H(\alpha_1, \alpha_2) - E(\alpha_1, \alpha_2)S(\alpha_1, \alpha_2)) = 0 \quad (1)$$

where $S(\alpha_1, \alpha_2)$ and $H(\alpha_1, \alpha_2)$ are $16 \times 16$ matrices of overlapping integrals and single-electron Hamiltonian, respectively, reducible to $4 \times 4$ matrices. $E(\alpha_1, \alpha_2)$ is a required electron energy band. About the parameters $\alpha_1$ and $\alpha_2$, see below.

This equation has 4 different real and negative roots $E_m(\alpha_1, \alpha_2)$, $m = 1, 2, 3, 4$. It can be demonstrated that they exhibit all the different solutions of the corresponding secular equation with $16 \times 16$ matrices. Within the initial quasi-classical approximation, these matrix elements can be found from the relations shown in the Appendix A.

Formally, these expressions contain infinite series. However, within the initial quasi-classical approximation, due to the finiteness of quasi-classical atomic radii, only a finite number of summands differs from zero. Thus, the series are terminated unambiguously.

The input data in a.u. in the form of quasi-classical parameters of boron atoms are shown in Tables 1 and 2. As it was mentioned above, the parameters of electron states fully or partially filled with electrons in the ground state were calculated on the basis of the theoretical, namely HF, values of electron levels, while for the excited state, we use the experimental value [98], which, however, is modulated by the multiplier of order of 1, 0.984151, leading to the coincidence between experimental and HF-theoretical first ionization potentials for an isolated boron atom: 0.304945 and 0.309856 a.u., respectively. Note that for the ground state, the $1s^2 2s^2 2p$ configuration is considered, not the $1s^2 2s 2p^2$ configuration, from which the ground state and first excited states of some boron-like ions arise [99].

**Table 1.** The inner and outer classical turning point radii $r'_i$ and $r''_i$ of electrons in boron atom.

| Orbital | State | $-E_i$ (a.u.) | $r'_i$ (a.u.) | $r''_i$ (a.u.) |
|---|---|---|---|---|
| 1 | 1*s* | 7.695335 | 0 | 0.509802 |
| 2 | 2*s* | 0.494706 | 0 | 4.021346 |
| 3 | 2*p* | 0.309856 | 0.744122 | 4.337060 |
| 4 | 2*p* | 0.214595 | 0.894159 | 5.211538 |

**Table 2.** The radii $r_\lambda$ of radial layers of quasi-classical averaging of potential in boron atoms and the averaged values of potential $\varphi_\lambda$.

| $\lambda$ | $r_\lambda$ (a.u.) | $\varphi_\lambda$ (a.u.) |
|---|---|---|
| 0 | 0 | – |
| 1 | 0.027585 | 210.5468 |
| 2 | 0.509802 | 8.882329 |
| 3 | 0.744122 | 3.65292 |
| 4 | 4.021346 | 0.206072 |
| 5 | 4.33706 | 0.000614 |

All the matrix elements and electron energies are calculated in points $\alpha_1 \vec{k}_1 + \alpha_2 \vec{k}_2$ of the reciprocal space with parameters $-1/2 \leq \alpha_1, \alpha_2 \leq +1/2$, i.e., within a rhombic unit cell of the reciprocal lattice (Figure 7). The first Brillouin zone for a boron flat sheet has a hexagonal shape. Of course, the areas of hexagonal and rhombic unit cells are equal (Figure 8).

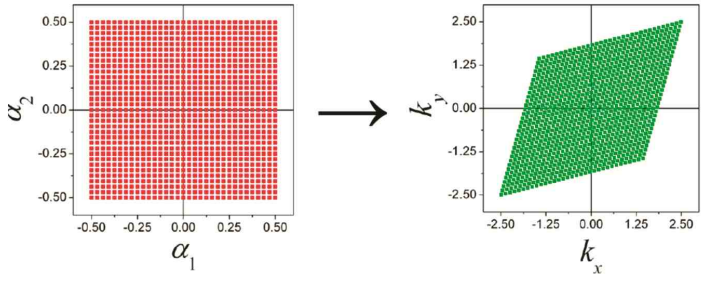


**Figure 7.** The transform from the $(\alpha_1, \alpha_2)$ domain to the $(k_x, k_y)$ domain of reciprocal space.

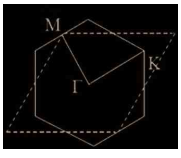


**Figure 8.** The hexagonal (first Brillouin zone) and rhombic unit cells of a reciprocal lattice of a flat boron sheet.

The unit cell is covered evenly by 1,002,001 points, at which the energy is found as a solution to the generalized eigenvalue problem.

The calculation has been performed in atomic units, a.u. Then, the results have been converted according to the relations: 1 a.u. of energy = 27.212 eV and 1 a.u. of length = 0.52918 Å.

Based on the resulting data set, we have constructed the electron band surfaces, the distribution of DoS in the bands, and the Fermi curve, emphasizing that, instead of the Fermi surface, the characteristics of 3-D crystals, 2-D crystals are characterized by Fermi curves.

## 3. Results and Discussion

In the quasi-classically calculated electronic structure of the flat boron sheet, we resolve four bands of energy. We have to emphasize that for simplicity, the band surfaces below are shown over a rhombic (not hexagonal) domain.

The lowest energy band $E_1$ surface is found to be almost a plane placed at the level of $E_{1\min} = E_{1\max} = -276.21$ eV. Thus, the chemical shift against the core 1$s$ atomic level $E_{1s} = -209.41$ eV equals to $\delta E_1 = E_{1s} - E_1 = 66.80$ eV. Dispute the shift of the B 1$s$ atomic level, it retains an order of magnitude after transforming in an electronic band of the boron flat sheet. The lowest-lying band $E_1$ is fully filled with electrons.

The band $E_2$ is the highest fully filled band (Figure 9) with bottom at $E_{2\min} = -37.21$ eV and top at $E_{2\max} = -19.85$ eV, i.e., with a width of $\Delta E_2 = E_{2\max} - E_{2\min} = 17.36$ eV. Note that, this range of energies is comparable in order of magnitude with a valence 2$s$ atomic level of $E_{2s} = -13.46$ eV.

The band $E_3$ (Figure 10) is partially filled, i.e., partially empty, with a bottom at $E_{3\min} = -23.08$ eV and top at $E_{3\max} = -17.16$ eV, i.e., with a width of $\Delta E_3 = E_{3\max} - E_{3\min} = 5.92$ eV. Note that this range of energies is comparable in order of magnitude with a valence 2$p$ atomic level $E_{2p} = -8.43$ eV.

The band $E_4$ (Figure 11) is empty, with a bottom at $E_{4\min} = -17.65$ eV and top at $E_{4\max} = -8.08$ eV, i.e., with a width of $\Delta E_4 = E_{4\max} - E_{4\min} = 9.57$ eV. Note that this range of energies is comparable in order of magnitude with the modulated value of the excited 2$p$ level $E'_{2p} = -5.84$ eV.

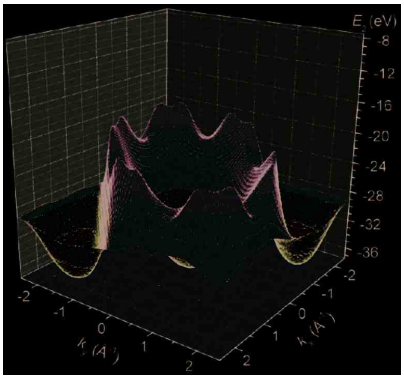


(**a**)

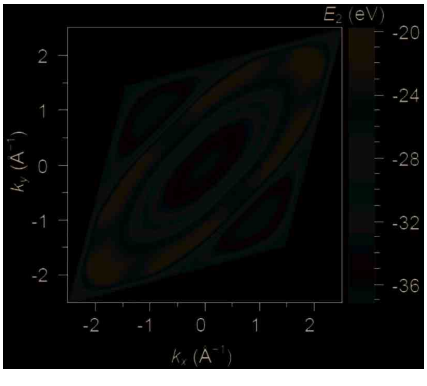


(**b**)

**Figure 9.** The band $E_2$ energy surface (**a**) and contour plots (**b**) over a rhombic unit cell.

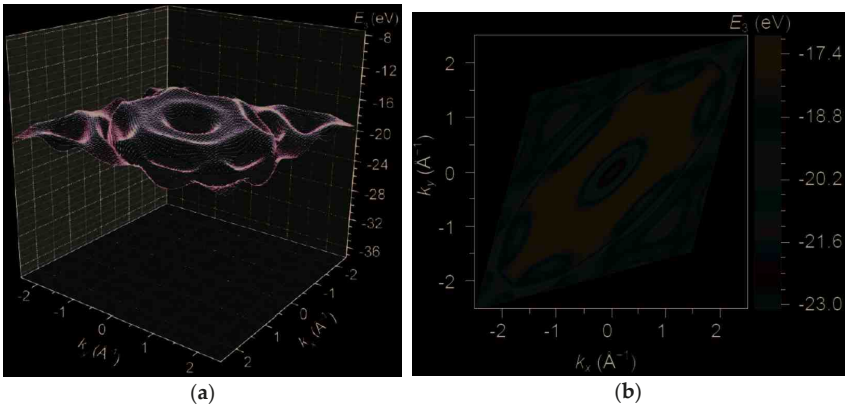


(**a**) (**b**)

**Figure 10.** The band $E_3$ energy surface (**a**) and contour plots (**b**) over a rhombic unit cell.

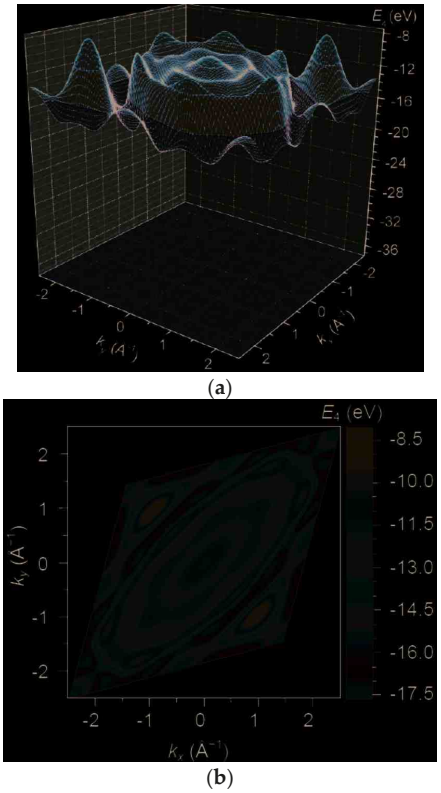


(**a**)

(**b**)

**Figure 11.** The band $E_4$ energy surface (**a**) and contour plots (**b**) over a rhombic unit cell.

Between bands $E_1$ and $E_2$, there is a very wide energy gap of $\Delta E_{12} = E_{2\min} - E_{1\max} = 239.00$ eV, while pairs of bands $E_2$ and $E_3$, and $E_3$ and $E_4$ overlap each with other, i.e. there are obtained pseudo-gaps of $\Delta E_{23} = E_{3\min} - E_{2\max} = -3.23$ eV and $\Delta E_{34} = E_{4\min} - E_{3\max} = -0.49$ eV.

The Fermi level is found at $E_{\text{Fermi}} = -19.42$ eV, within the part of the band $E_3$ without overlapping with other bands. This result confirms the metallicity of the boron sheet.

Thus, all the electron energies are found to be negative. It means that all electrons, including conduction electrons at the Fermi level, are bounded inside the 2-D crystal. This result once more evidences the correctness of the calculations performed in this work. The total width of valence and conduction bands equal to $\Delta E_V = E_{\text{Fermi}} - E_{2\min} = 17.79$ eV and $\Delta E_C = E_{4\max} - E_{\text{Fermi}} = 11.34$ eV, respectively. The upper valence band width is $\Delta E_{\text{VU}} = E_{\text{Fermi}} - E_{2\max} = 0.43$ eV. As expected, it is negligible if compared with that of a conduction band.

To compare easily our results with the literature data, in addition to the presentation of the band structure using the contour plots of the whole Brillouin zone in Figures 12 and 13, we plot the band energies (as well as their second derivatives and corresponding parabolic approximations) along the main lines of symmetry.

Our quasi-classical calculation of the crystalline band structure, like any other approach also utilizing HF parameters of constituting atoms, cannot determine the absolute values of energy parameters with a high accuracy. By this reason, the above mentioned value $E_{\text{Fermi}}$ cannot be used directly to determine the electron work function of the boron sheet. This goal can be achieved only after corrections are made to include the electron-correlation and to exclude the electron-self-interacting effects, which have to allow an accurate determination of the position for the vacuum level of energy

$E = 0$. However, the shifting of the reference point at the energy axis does not affect the energy differences, which are credible as are determined with quite an acceptable accuracy. They are collected in Table 3.

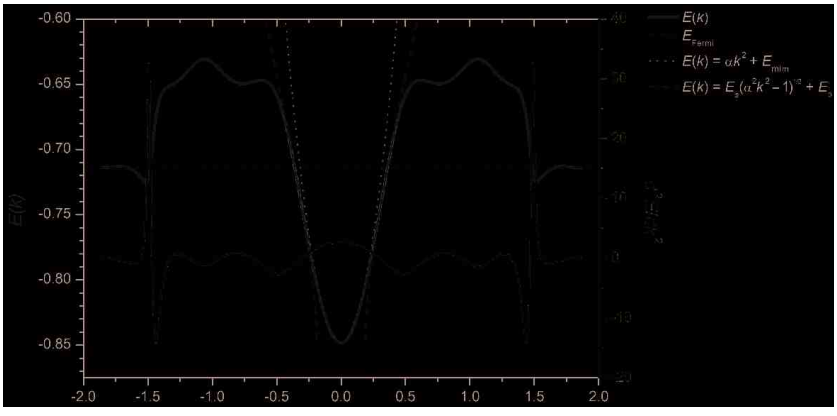


**Figure 12.** The section of the conduction band surface along the main diagonal of a rhombic unit cell (direction Γ–K) of reciprocal space (in atomic units).

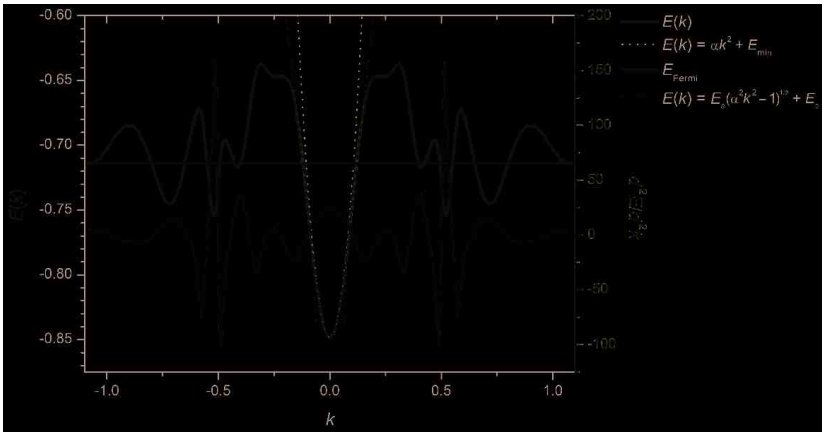


**Figure 13.** The section of the conduction band surface along a small diagonal of a rhombic unit cell (direction Γ–M) of reciprocal space (in atomic units).

**Table 3.** The band widths and (pseudo)gaps between bands.

| Band | $\Delta E_i$, eV | $\Delta E_{ij}$, eV |
|---|---|---|
| 1 | 0 | |
| 2 | 17.36 | 239 |
| 3 | 5.92 | −3.23 |
| 4 | 9.57 | −0.49 |

The Fermi curve of a boron flat sheet is found to be consisting of parts of a number of closed curves including concentric ones, the centre of which can be approximated by ellipse with long and short axes along the Γ–K and Γ–M directions, respectively (Figure 14).

**Figure 14.** Curves of the intersection of the band surface with the Fermi plane in neighboring rhombic unit cells of reciprocal space.

As it is known, for semiconductors, the effective mass conception referring to band zone curvatures is used to approximate the wave-vector dependence of electron energies near the band gap. As for metals, the Fermi surface curvature can be used to estimate the effective mass of conduction electrons and hence their mobility.

The ellipse representing a branch of intersection between the $E_3$-band surface with the $E_{\text{Fermi}}$-plane can be described by the equation

$$\frac{\hbar^2 k_{\Gamma\text{–K}}^2}{2m_{\Gamma\text{–K}}} + \frac{\hbar^2 k_{\Gamma\text{–M}}^2}{2m_{\Gamma\text{–M}}} = F \tag{2}$$

where $k_{\Gamma\text{–K}}$ and $k_{\Gamma\text{–M}}$ are wave-number components along perpendicular axes Γ–K and Γ–M and $F = E_{\text{Fermi}} - E_{3\text{min}} = 3.66$ eV is the Fermi energy. The effective masses $m_{\Gamma\text{–K}}$ and $m_{\Gamma\text{–M}}$ can be estimated from this equation if it is rewritten in the form of a normalized ellipse equation

$$\frac{k_{\Gamma\text{–K}}^2}{k_{\Gamma\text{–K}\ \ 0}^2} + \frac{k_{\Gamma\text{–M}}^2}{k_{\Gamma\text{–M}\ \ 0}^2} = 1 \tag{3}$$

where $k_{\Gamma\text{–K}\ \ 0}$ and $k_{\Gamma\text{–M}\ \ 0}$ are half-axes in the directions Γ–K and Γ–M, respectively:

$$k_{\Gamma\text{–K}\ \ 0} = \frac{\sqrt{2m_{\Gamma\text{–K}}F}}{\hbar} \approx 0.679/A$$

and

$$k_{\Gamma\text{–M}\ \ 0} = \frac{\sqrt{2m_{\Gamma\text{–M}}F}}{\hbar} \approx 0.224/A.$$

Then, one can calculate the effective mass of the conduction electrons $m_\sigma$, i.e., electrons placed at the Fermi level, from the relation

$$\frac{2}{m_\sigma} = \frac{1}{m_{\Gamma\text{–K}}} + \frac{1}{m_{\Gamma\text{–M}}} \tag{4}$$

The effective electron mass at the Fermi level reveals a significant anisotropy. For the central ellipse, the effective masses are $m_{\Gamma\text{–K}}/m_0 \approx 0.480$ and $m_{\Gamma\text{–M}}/m_0 \approx 0.052$, with $m_\sigma/m_0 \approx 0.094$, where $m_0$ is the free electron mass.

The Fermi curve of a boron flat sheet is found to consist of 6 parts of 3 ellipses representing the quadric energy-dispersion of the conduction electrons; see Figure 15.

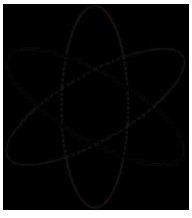

**Figure 15.** The Fermi curve of a boron flat sheet.

DoS within the bands $E_2$, $E_3$, and $E_4$ against electron energy renormalized to the Fermi level $E \to E - E_{\text{Fermi}}$ are presented in Figure 16 in two different scales for the convenient consideration. As for the band $E_1$, DoS within this band is proportional to the Dirac function, $\sim \delta(E + 256.42\ [\text{eV}])$, with the accordingly renormalized argument $-276.21\ \text{eV} \to -276.21\ \text{eV} - (-19.42\ \text{eV}) = 256.79\ \text{eV}$.

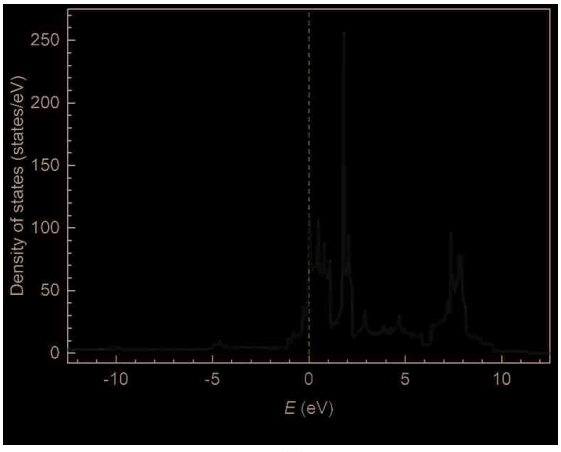


(**a**)

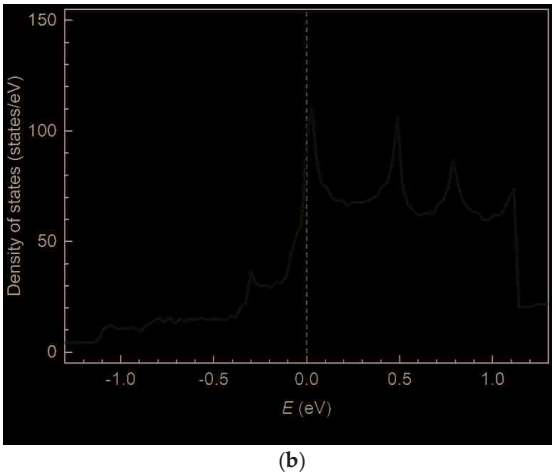


(**b**)

**Figure 16.** The density-of-electron-states renormalized to the Fermi level in a valence band and the lower and upper conduction bands of a boron flat sheet in two different scales: general view (**a**) and in Fermi level vicinity (**b**).

The overall shapes of DoSs obtained by us and previously by others, especially, in References [31,33,47] are rather similar but with some differences. It is understandable as these structures are buckled/puckered or flat variants of the same triangular lattice with or without hexagonal holes (Figure 17). The discrepancies may be attributed with the perturbations related to the mentioned structural changes and differences between the computing methods utilized, as well as the difference between projected onto in-plane or out-of-plane orbitals' densities-of-states (PDoSs) from the total DoS of the sheet.

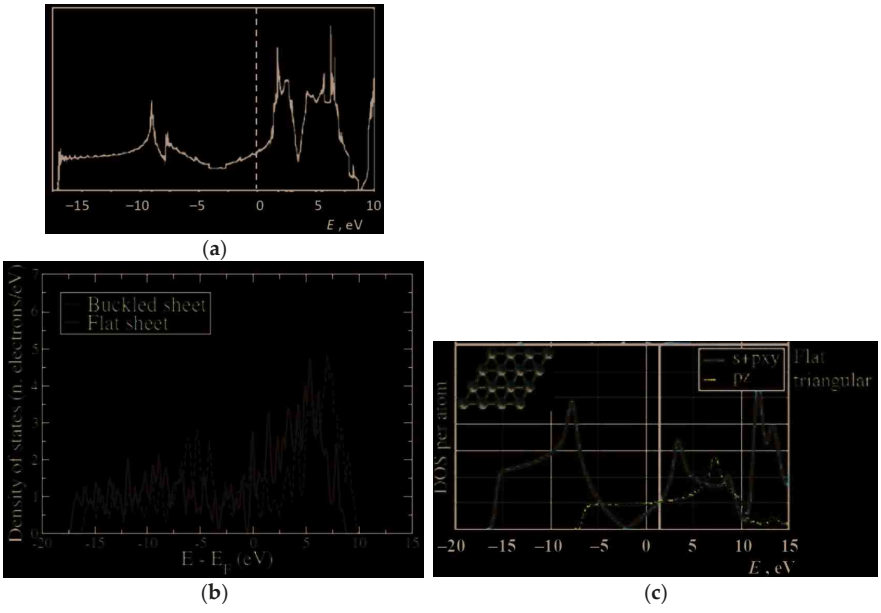


**Figure 17.** The densities-of-electron-states of boron sheets calculated by different methods: (**a**) modified from Reference [31], (**b**) from Reference [33], and (**c**) modified from Reference [37].

The Fermi curve of the monolayer flat boron sheet approximated by parts of concentric closed ellipse-like curves could be considered as a certain kind of topological analog of the Fermi surface (Figure 18) in the form of a half-torus and distorted cylinder of magnesium diboride $MgB_2$ [100], which is believed to be a structural analog of the hypothetical multilayered boron sheet, where metal Me atoms in a metal diboride $MeB_2$ structure are replaced by B-atoms themselves.

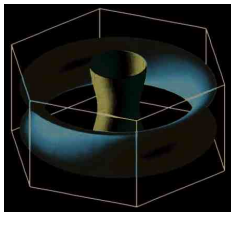

**Figure 18.** The Fermi surface of magnesium diboride $MgB_2$ [100].

The low effective mass of conduction electrons at the Fermi level indicates a high mobility of electrons and, hence, a high conductivity of the flat boron sheet.

## 4. Conclusions

In summary, we can conclude that the electronic band structure of a boron flat triangular sheet has been calculated within a quasi-classical approach for the quasi-classical structural parameter (B–B bond length) of $a = 1.78$Å. It is shown to have metallic properties like most of other modifications of boron sheets.

There are resolved four electronic bands: $E_1$, $E_2$, $E_3$, and $E_4$. The bands' widths are $\Delta E_1 = 0.00$, $\Delta E_2 = 17.36$, $\Delta E_3 = 5.92$, and $\Delta E_4 = 9.57$ eV, respectively. The (pseudo)gaps between the bands are $\Delta E_{12} = 239.00$, $\Delta E_{23} = -3.23$, and $\Delta E_{34} = -0.49$ eV. The Fermi level $E_{\text{Fermi}}$ is located within the filled band $E_3$, confirming the metallicity of the boron flat sheet.

The Fermi curve of a boron flat sheet consists of parts of 3 ellipses with semimajor and semiminor axes along the Γ–K and Γ–M directions, respectively. The effective electron mass at the Fermi level reveals a distinct anisotropy: $m_{\Gamma-\text{K}}/m_0 \approx 0.480$ and $m_{\Gamma-\text{M}}/m_0 \approx 0.052$, with $m_\sigma/m_0 \approx 0.094$ for conduction mass. The low effective mass of conduction electrons indicates a high mobility of electrons and, hence, a high conductivity of flat boron sheets.

The shapes of density-of-states obtained here for flat holeless boron sheets and previously calculated ones are rather similar, which is understandable as these structures are buckled/puckered or flat but with hexagonal holes, variants of the same triangular lattice. The remaining discrepancies may be attributed to the perturbations associated with the mentioned structural changes and differences in the used models.

**Author Contributions:** Conceptualization, L.C. and R.B.; methodology, L.C.; software, I.M.; validation, L.C., I.M., and R.B.; formal analysis, I.M.; investigation, L.C., I.M., and R.B.; resources, L.C. and R.B.; data curation, I.M.; writing—original draft preparation, L.C.; writing—review and editing, I.M.; visualization, L.C. and I.M.; project administration, L.C.

**Funding:** This research was funded by Shota Rustaveli National Science Foundation of Georgia (SRNSFG), Grant AR–18–1045: "Obtaining of boron carbide-based nanostructured heterophase ceramic materials and products with improved performance characteristics".

**Conflicts of Interest:** The authors declare no conflict of interest. The funder had no role in the design of the study; in the collection, analyses, or interpretation of data; in the writing of the manuscript; or in the decision to publish the results.

## Appendix A

Within the initial quasi-classical approximation, the matrix elements of overlapping integrals $S(\alpha_1, \alpha_2)$ and single-electron Hamiltonian $H(\alpha_1, \alpha_2)$ can be respectively found from following explicit relations:

$$S_{jl}(\alpha_1, \alpha_2) = \frac{3}{4\pi} \sum_{n_1=-\infty}^{n_1=+\infty} \sum_{n_2=-\infty}^{n_2=+\infty} \frac{V_{jl}(n_1, n_2)}{\sqrt{(r''^3_j - r'^3_j)(r''^3_l - r'^3_l)}} \cos 2\pi(n_1\alpha_1 + n_2\alpha_2)$$

$$V_{jl}(n_1, n_2) =$$
$$= V(r''_j, r''_l, a\sqrt{n_1^2 + n_1 n_2 + n_2^2}) +$$
$$+ V(r'_j, r'_l, a\sqrt{n_1^2 + n_1 n_2 + n_2^2}) -$$
$$- V(r''_j, r'_l, a\sqrt{n_1^2 + n_1 n_2 + n_2^2}) -$$
$$- V(r'_j, r''_l, a\sqrt{n_1^2 + n_1 n_2 + n_2^2})$$

and

$$H_{jl}(\alpha_1,\alpha_2)=\frac{3}{4\pi}\sum_{n_1=-\infty}^{n_1=+\infty}\sum_{n_2=-\infty}^{n_2=+\infty}\sum_{\nu_1=-\infty}^{\nu_1=+\infty}\sum_{\nu_2=-\infty}^{\nu_2=+\infty}\sum_{\lambda=1}^{\lambda=5}\frac{\varphi_\lambda V_{jl\lambda}(n_1,n_2,\nu_1,\nu_2)}{\sqrt{({r''}_j^3-{r'}_j^3)({r''}_l^3-{r'}_l^3)}}\cos 2\pi(n_1\alpha_1+n_2\alpha_2)$$

$$V_{jl\lambda}(n_1,n_2,\nu_1,\nu_2)=$$

$$=V({r''}_j,{r''}_l,r_\lambda,a\sqrt{n_1^2+n_1n_2+n_2^2},a\sqrt{\nu_1^2+\nu_1\nu_2+\nu_2^2},a\sqrt{(n_1-\nu_1)^2+(n_1-\nu_1)(n_2-\nu_2)+(n_2-\nu_2)^2})+$$
$$+V({r''}_j,{r'}_l,r_{\lambda-1},a\sqrt{n_1^2+n_1n_2+n_2^2},a\sqrt{\nu_1^2+\nu_1\nu_2+\nu_2^2},a\sqrt{(n_1-\nu_1)^2+(n_1-\nu_1)(n_2-\nu_2)+(n_2-\nu_2)^2})+$$
$$+V({r'}_j,{r''}_l,r_{\lambda-1},a\sqrt{n_1^2+n_1n_2+n_2^2},a\sqrt{\nu_1^2+\nu_1\nu_2+\nu_2^2},a\sqrt{(n_1-\nu_1)^2+(n_1-\nu_1)(n_2-\nu_2)+(n_2-\nu_2)^2})+$$
$$+V({r'}_j,{r'}_l,r_\lambda,a\sqrt{n_1^2+n_1n_2+n_2^2},a\sqrt{\nu_1^2+\nu_1\nu_2+\nu_2^2},a\sqrt{(n_1-\nu_1)^2+(n_1-\nu_1)(n_2-\nu_2)+(n_2-\nu_2)^2})-$$
$$-V({r'}_j,{r''}_l,r_\lambda,a\sqrt{n_1^2+n_1n_2+n_2^2},a\sqrt{\nu_1^2+\nu_1\nu_2+\nu_2^2},a\sqrt{(n_1-\nu_1)^2+(n_1-\nu_1)(n_2-\nu_2)+(n_2-\nu_2)^2})-$$
$$-V({r''}_j,{r'}_l,r_\lambda,a\sqrt{n_1^2+n_1n_2+n_2^2},a\sqrt{\nu_1^2+\nu_1\nu_2+\nu_2^2},a\sqrt{(n_1-\nu_1)^2+(n_1-\nu_1)(n_2-\nu_2)+(n_2-\nu_2)^2})-$$
$$-V({r''}_j,{r''}_l,r_{\lambda-1},a\sqrt{n_1^2+n_1n_2+n_2^2},a\sqrt{\nu_1^2+\nu_1\nu_2+\nu_2^2},a\sqrt{(n_1-\nu_1)^2+(n_1-\nu_1)(n_2-\nu_2)+(n_2-\nu_2)^2})-$$
$$-V({r'}_j,{r'}_l,r_{\lambda-1},a\sqrt{n_1^2+n_1n_2+n_2^2},a\sqrt{\nu_1^2+\nu_1\nu_2+\nu_2^2},a\sqrt{(n_1-\nu_1)^2+(n_1-\nu_1)(n_2-\nu_2)+(n_2-\nu_2)^2}),$$

where $V(R_1,R_2,D_{12})$ and $V(R_1,R_2,R_3,D_{12},D_{13},D_{23})$ are intersection volumes of two and three spheres, respectively, with radii $R_1$, $R_2$, and $R_3$ and intercentral distances $D_{12}$, $D_{13}$, and $D_{23}$.

## References


1. Becker, R.; Chkhartishvili, L.; Martin, P. Boron, the new graphene? *Vac. Technol. Coat.* **2015**, *16*, 38–44.
2. Boustani, I. Systematic ab initio investigation of bare boron clusters: Determination of the geometry and electronic structures of $B_n$ ($n$=12–14). *Phys. Rev. B* **1997**, *55*, 16426–16438. [CrossRef]
3. Boustani, I.; Rubio, A.; Alonso, J.A. Ab initio study of $B_{32}$ clusters: Competition between spherical, quasiplanar and tubular isomers. *Chem. Phys. Lett.* **1999**, *311*, 21–28. [CrossRef]
4. Boustani, I.; Quandt, A.; Hernandez, E.; Rubio, A. New boron based nanostructured materials. *J. Chem. Phys.* **1999**, *110*, 3176–3185. [CrossRef]
5. Boustani, I.; Quandt, A.; Rubio, A. Boron quasicrystals and boron nanotubes: Ab initio study of various $B_{96}$ isomers. *J. Solid State Chem.* **2000**, *154*, 269–274. [CrossRef]
6. Mukhopadhyay, S.; He, H.; Pandey, R.; Yap, Y.K.; Boustani, I. Novel spherical boron clusters and structural transition from 2D quasi-planar structures to 3D double-rings. *J. Phys. Conf. Ser.* **2009**, *176*, 012028. [CrossRef]
7. Ozdogan, C.; Mukhopadhyay, S.; Hayami, W.; Guvenc, Z.B.; Pandey, R.; Boustani, I. The unusually stable $B_{100}$ fullerene, structural transitions in boron nanostructures, and a comparative study of $\alpha$- and $\gamma$-boron and sheets. *J. Phys. Chem. C* **2010**, *114*, 4362–4375. [CrossRef]
8. Zhai, H.-J.; Kiran, B.; Li, J.; Wang, L.-S. Hydrocarbon analogues of boron clusters – Planarity, aromaticity and antiaromaticity. *Nat. Mater.* **2003**, *2*, 827–833. [CrossRef] [PubMed]
9. Piazza, Z.A.; Hu, H.-S.; Li, W.-L.; Zhao, Y.-F.; Li, J.; Wang, L.-S. Planar hexagonal $B_{36}$ as a potential basis for extended single-atom layer boron sheets. *Nat. Commun.* **2014**, *5*, 3113–3118. [CrossRef] [PubMed]
10. Zhai, H.-J.; Zhao, Y.-F.; Li, W.-L.; Chen, Q.; Bai, H.; Hu, H.-S.; Piazza, Z.A.; Tian, W.-J.; Lu, H.-G.; Wu, Y.-B.; et al. Observation of an all-boron fullerene. *Nat. Chem.* **2014**, *6*, 727–731. [CrossRef] [PubMed]
11. Ciuparu, D.; Klie, R.F.; Zhu, Y.; Pfefferle, L. Synthesis of pure boron single-wall nanotubes. *J. Phys. Chem. B* **2004**, *108*, 3967–3969. [CrossRef]
12. Kiran, B.; Bulusu, S.; Zhai, H.-J.; Yoo, S.; Zeng, X.C.; Wang, L.-S. Planar-to-tubular structural transition in boron clusters: $B_{20}$ as the embryo of single-walled boron nanotubes. *Proc. Natl. Acad. Sci. USA* **2005**, *102*, 961–964. [CrossRef] [PubMed]
13. Liu, F.; Shen, C.; Su, Z.; Ding, X.; Deng, S.; Chen, J.; Xu, N.; Gao, H. Metal-like single crystalline boron nanotubes: Synthesis and in situ study on electric transport and field emission properties. *J. Mater. Chem.* **2010**, *20*, 2197–2205. [CrossRef]
14. Oger, E.; Crawford, N.R.M.; Kelting, R.; Weis, P.; Kappes, M.M.; Ahlrichs, R. Boron cluster cations: Transition from planar to cylindrical structures. *Angew. Chem. Int. Ed.* **2007**, *46*, 8503–8506. [CrossRef] [PubMed]
15. Oger, E. Strukturaufklärung durch Mobilitätsmessungen an massenselektierten Clusterionen in der Gasphase. Ph.D. Thesis, University of Karlsruhe—Karlsruher Institute of Technology, Karlsruher, Germany, 2010.

16. Mannix, A.J.; Zhou, X.-F.; Kiraly, B.; Wood, J.D.; Alducin, D.; Myers, B.D.; Liu, X.; Fisher, B.L.; Santiago, U.; Guest, J.R.; et al. Synthesis of borophenes: Anisotropic, two-dimensional boron polymorphs. *Science* **2015**, *350*, 1513–1516. [CrossRef] [PubMed]
17. Feng, B.; Zhang, J.; Zhong, Q.; Li, W.; Li, S.; Li, H.; Cheng, P.; Meng, S.; Chen, L.; Wu, K. Experimental realization of two-dimensional boron sheets. *Nat. Chem.* **2016**, *8*, 563–568. [CrossRef] [PubMed]
18. Parakhonskiy, G.; Dubrovinskaia, N.; Bykova, E.; Wirth, R.; Dubrovinsky, L. Experimental pressure-temperature phase diagram of boron: Resolving the long-standing enigma. *Sci. Rep.* **2011**, *1*, 96. [CrossRef] [PubMed]
19. McGrady, J.W.; Papaconstantopoulos, D.A.; Mehl, M.J. Tight-binding study of boron structures. *J. Phys. Chem. Solids* **2014**, *75*, 1106–1112. [CrossRef]
20. Shirai, K. Phase diagram of boron crystals. *Jpn. J. Appl. Phys.* **2017**, *56*, 05FA06. [CrossRef]
21. Shirai, K.; Uemura, N.; Dekura, H. Structure and stability of pseudo-cubic tetragonal boron. *Jpn. J. Appl. Phys.* **2017**, *56*, 05FB05. [CrossRef]
22. Imai, Y.; Mukaida, M.; Ueda, M.; Watanabe, A. Band-calculation of the electronic densities of states and the total energies of boron–silicon system. *J. Alloys Comp.* **2002**, *347*, 244–251. [CrossRef]
23. Masago, A.; Shirai, K.; Katayama–Yoshida, H. Crystal stability of α- and β-boron. *Phys. Rev. B* **2006**, *73*, 104102. [CrossRef]
24. Jemmis, E.D.; Prasad, D.L.V.K. Icosahedral $B_{12}$, macropolyhedral boranes, β-rhombohedral boron and boron-rich solids. *J. Solid State Chem.* **2006**, *179*, 2768–2774. [CrossRef]
25. Van Setten, M.J.; Uijttewaal, M.A.; DeWijs, G.A.; DeGroot, R.A. Thermodynamic stability of boron: The role of defects and zero point motion. *J. Am. Chem. Soc.* **2007**, *129*, 2458–2465. [CrossRef] [PubMed]
26. Ogitsu, T.; Gygi, F.; Reed, J.; Motome, Y.; Schwegler, E.; Galli, G. Imperfect crystal and unusual semiconductor: Boron, a frustrated element. *J. Am. Chem. Soc.* **2009**, *131*, 1903–1909. [CrossRef] [PubMed]
27. Widom, M.; Mihalkovic, M. Relative stability of α and β boron. *J. Phys. Conf. Ser.* **2009**, *176*, 012024. [CrossRef]
28. Slack, G.A.; Hejna, C.I.; Garbauskas, M.F.; Kasper, J.S. The crystal structure and density of β-rhombohedral boron. *J. Solid State Chem.* **1988**, *76*, 52–63. [CrossRef]
29. Boustani, I. New quasi-planar surfaces o fbare boron. *Surf. Sci.* **1997**, *377*, 355–363. [CrossRef]
30. Boustani, I.; Quandt, A. Boronin ab initio calculations. *Comput. Mater. Sci.* **1998**, *11*, 132–137. [CrossRef]
31. Evans, M.H.; Joannopoulos, J.D.; Pantelides, S.T. Electronic and mechanical properties of planar and tubular boron structures. *Phys. Rev. B* **2005**, *72*, 045434. [CrossRef]
32. Cabria, I.; Lopez, M.J.; Alonso, J.A. Density functional calculations of hydrogen adsorption on boron nanotubes and boron sheets. *Nanotechnology* **2006**, *17*, 778–785. [CrossRef]
33. Cabria, I.; Alonso, J.A.; Lopez, M.J. Buckling in boron sheets and nanotubes. *Phys. Status Solidi A* **2006**, *203*, 1105–1110. [CrossRef]
34. Kunstmann, J.; Quandt, A. Broad boron sheets and boron nanotubes: An ab initio study of structural, electronic, and mechanical properties. *Phys. Rev. B* **2006**, *74*, 035413. [CrossRef]
35. Lau, K.C.; Pati, R.; Pandey, R.; Pineda, A.C. First-principles study of the stability and electronic properties of sheets and nanotubes of elemental boron. *Chem. Phys. Lett.* **2006**, *418*, 549–554. [CrossRef]
36. Lau, K.C.; Pandey, R. Stability and electronic properties of atomistically-engineered 2D boron sheets. *J. Phys. Chem. C* **2007**, *111*, 2906–2912. [CrossRef]
37. Tang, H.; Ismail–Beigi, S. Novel precursors for boron nanotubes: The competition of two-center and three-center bonding in boron sheets. *Phys. Rev. Lett.* **2007**, *99*, 115501. [CrossRef] [PubMed]
38. Yang, X.; Ding, Y.; Ni, J. Ab initio prediction of stable boron sheets and boron nanotubes: Structure, stability, and electronic properties. *Phys. Rev. B* **2008**, *77*, 041402(R). [CrossRef]
39. Sebetci, A.; Mete, E.; Boustani, I. Freestanding double walled boron nanotubes. *J. Phys. Chem. Solids* **2008**, *69*, 2004–2012. [CrossRef]
40. Singh, A.K.; Sadrzadeh, A.; Yakobson, B.I. Probing properties of boron α-tubes by ab initio calculations. *Nano Lett.* **2008**, *8*, 1314–1317. [CrossRef] [PubMed]
41. Wang, J.; Liu, Y.; Li, Y.-C. A new class of boron nanotubes. *Chem. Phys. Chem.* **2009**, *10*, 3119–3121. [CrossRef] [PubMed]
42. Tang, H.; Ismail–Beigi, S. First-principles study of boron sheets and nanotubes. *Phys. Rev. B* **2010**, *82*, 115412. [CrossRef]

43. Zope, R.R.; Baruah, T. Snub boro nnanostructures: Chiral fullerenes, nanotubes and planar sheet. *Chem. Phys. Lett.* **2011**, *501*, 193–196. [CrossRef]
44. Simsek, M.; Aydın, S. First-principles calculations of two dimensional boron sheets. In *Abstracts of the 17th International Symposium on Boron, Borides and Related Materials, Istanbul, Turkey, 11–17 September 2011*; Yucel, O., Ed.; BKM: Ankara, Turkey, 2011; p. 86.
45. Kunstmann, J.; Boeri, L.; Kortus, J. Bonding in boron: Building high-pressure phases from boron sheets. In *Abstracts of the 17th International Symposium on Boron, Borides and Related Materials, Istanbul, Turkey, 11–17 September 2011*; Yucel, O., Ed.; BKM: Ankara, Turkey, 2011; p. 289.
46. Bezugly, V.; Kunstmann, J.; Grundkotter-Stock, B.; Frauenheim, T.; Niehaus, T.; Cuniberti, G. Highly conductive boron nanotubes: Transport properties, work functions, and structural stabilities. *ACS Nano* **2011**, *5*, 4997–5005. [CrossRef] [PubMed]
47. Tang, H. First-Principles Investigation on Boron Nanostructures. Ph.D. Thesis, Yale University, New Haven, CT, USA, 2011.
48. Zhou, X.-F.; Dong, X.; Oganov, A.R.; Zhu, Q.; Tian, Y.; Wang, H.-T. Semimetallic two-dimensional boron allotrope with massless Dirac fermions. *Phys. Rev. Lett.* **2014**, *112*, 085502. [CrossRef]
49. Wu, X.; Dai, J.; Zhao, Y.; Zhuo, Z.; Yang, J.; Zeng, X. Two-dimensional boron monolayer sheets. *ACS Nano* **2012**, *6*, 7443–7453. [CrossRef] [PubMed]
50. Lu, H.; Mu, Y.; Li, S.-D. Comment on "Two-dimensional boron monolayer sheets". *ACS Nano* **2013**, *7*, 879. [CrossRef] [PubMed]
51. Wu, X.; Dai, J.; Zhao, Y.; Zhuo, Z.; Yang, J.; Zeng, X.C. Reply to "Comment on 'Two-dimensional boron monolayer sheets'". *ACS Nano* **2013**, *7*, 880–881. [CrossRef] [PubMed]
52. Zhou, X.-F.; Oganov, A.R.; Shao, X.; Zhu, Q.; Wang, H.-T. Unexpected reconstruction of the α-boron (111) surface. *Phys. Rev. Lett.* **2014**, *113*, 176101. [CrossRef] [PubMed]
53. Mu, Y.; Chen, Q.; Chen, N.; Lu, H.; Li, S.-D. A novel borophene featuring heptagonal holes: Common precursor of borospherenes. *Phys. Chem. Chem. Phys.* **2017**, *30*, 19890–19895. [CrossRef] [PubMed]
54. Boroznina, E.V.; Davletova, O.A.; Zaporotskova, I.V. Boron monolayer $\gamma_3$-type. Formation of the vacancy defect and pinhole. *J. Nano-Electron. Phys.* **2016**, *8*, 04054. [CrossRef]
55. Chkhartishvili, L. All-boron nanostructures. In *CRC Concise Encyclopedia of Nanotechnology*; Kharisov, B.I., Kharissova, O.V., Ortiz–Mendez, U., Eds.; CRC Press: Boca Raton, FL, USA, 2016; pp. 53–69.
56. Li, W.-L.; Pal, R.; Piazza, Z.A.; Zeng, X.C.; Wang, L.-S. $B_{27}^-$: Appearance of the smallest planar boron cluster containing a hexagonal vacancy. *J. Chem. Phys.* **2015**, *142*, 204305. [CrossRef] [PubMed]
57. Vast, N.; Bernard, S.; Zerah, G. Structural and electronic properties of liquid boron from a molecular-dynamics simulation. *Phys. Rev. B* **1995**, *52*, 4123–4130. [CrossRef]
58. Krishnan, S.; Ansell, S.; Felten, J.J.; Volin, K.J.; Price, D.L. Structure of liquid boron. *Phys. Rev. Lett.* **1998**, *81*, 586–589. [CrossRef]
59. Price, D.L.; Alatas, A.; Hennet, L.; Jakse, N.; Krishnan, S.; Pasturel, A.; Pozdnyakova, I.; Saboungi, M.-L.; Said, A.; Scheunemann, R.; et al. Liquid boron: X-ray measurements and ab initio molecular dynamics simulations. *Phys. Rev. B* **2009**, *79*, 134201. [CrossRef]
60. Butler, S.Z.; Hollen, S.M.; Cao, L.; Cui, Y.; Gupta, J.A.; Gutierrez, H.R.; Heinz, T.F.; Hong, S.S.; Huang, J.; Ismach, A.F.; et al. Progress, challenges, and opportunities in two-dimensional materials beyond graphene. *ACS Nano* **2013**, *7*, 2898–2926. [CrossRef] [PubMed]
61. Zhao, L.; Xu, C.; Su, H.; Liang, J.; Lin, S.; Gu, L.; Wang, X.; Chen, M.; Zheng, N. Single-crystalline rhodium nanosheets with atomic thickness. *Adv. Sci.* **2015**, *2*, 1500100. [CrossRef] [PubMed]
62. Xu, J.; Chang, Y.; Gan, L.; Ma, Y.; Zhai, T. Ultra thin nanosheets: Ultrathin single-crystalline boron nanosheets for enhanced electro-optical performances. *Adv. Sci.* **2015**, *2*, 1500023. [CrossRef] [PubMed]
63. Zhang, L.Z.; Yan, Q.B.; Du, S.X.; Su, G.; Gao, H.-J. Boron sheet adsorbed on metal surfaces: Structures and electronic properties. *J. Phys. Chem. C* **2012**, *116*, 18202–18206. [CrossRef]
64. Penev, E.S.; Bhowmick, S.; Sadrzadeh, A.; Yakobson, B.I. Polymorphism of two-dimensional boron. *Nano Lett.* **2012**, *12*, 2441–2445. [CrossRef] [PubMed]
65. Liu, Y.; Penev, E.S.; Yakobson, B.I. Probing the synthesis of two-dimensional boron by first-principles computations. *Angew. Chem. Int. Ed.* **2013**, *52*, 3156–3159. [CrossRef] [PubMed]
66. Liu, H.; Gao, J.; Zhao, J. Fromboronclustertotwo-dimensionalboronsheetonCu (111) surface: Growth mechanism and hole formation. *Sci. Rep.* **2013**, *3*, 3238.

67. Yi, W.-C.; Liu, W.; Botana, J.; Zhao, L.; Liu, Z.; Liu, J.-Y.; Miao, M.-S. Honeycomb boron allotropes with Dirac cones: A true analogue to graphene. *J. Phys. Chem. Lett.* **2017**, *8*, 2647–2653. [CrossRef] [PubMed]
68. Zhang, Z.; Mannix, A.J.; Hu, Z.; Kiraly, B.; Guisinger, N.P.; Hersam, M.C.; Yakobson, B.I. Substrate-induced nanoscale undulations of borophene on silver. *Nano Lett.* **2016**, *16*, 6622–6627. [CrossRef] [PubMed]
69. Wu, R.; Drozdov, I.K.; Eltinge, S.; Zahl, P.; Ismail–Beigi, S.; Bozovic, I.; Gozar, A. Large-area single-crystal sheets of borophene on Cu(111) surfaces. *Nat. Nanotechnol.* **2019**, *14*, 44–49. [CrossRef] [PubMed]
70. He, X.-L.; Weng, X.-J.; Zhang, Y.; Zhao, Z.; Wang, Z.; Xu, B.; Oganov, A.R.; Tian, Y.; Zhou, X.-F.; Wang, H.-T. Two-dimensional boron on Pb(110) surface. *Flat Chem.* **2018**, *7*, 34–41.
71. Tarkowski, T.; Majewski, J.A.; Gonzalez Szwacki, N. Energy decomposition analysis of neutral and negatively charged borophenes. *Flat Chem.* **2018**, *7*, 42–47. [CrossRef]
72. Gao, N.; Wu, X.; Jiang, X.; Bai, Y.; Zhao, J. Structure and stability of bilayer borophene: The roles of hexagonal holes and interlayer bonding. *Flat Chem.* **2018**, *7*, 48–54. [CrossRef]
73. Liu, D.; Tomanek, D. Effect of net charge on the relative stability of different 2D boron allotropes (ContributedTalk). In Proceedings of the APS March Meeting 2019, Boston, MA, USA, March 4–8 2019. Abstract: X13.00003.
74. Vangaveti, R. Boron Induced Surface Modification of Transition Metals. MSc Thesis, New Jersey's Science & Technology University, Newark, NJ, USA, 2006.
75. Chkhartishvili, L. Interaction between neutron-radiation and boron-containing materials. In *Radiation Synthesis of Materials and Compounds*; Kharisov, B.I., Kharissova, O.V., Ortiz–Méndez, U., Eds.; CRC Press—Taylor & Francis Group: Boca Raton, FL, USA, 2013; pp. 43–80.
76. Chkhartishvili, L.; Murusidze, I. Band structure of all-boron 2D metallic crystals as a prospective electromagnetic shielding material. In Proceedings of the International Conference on Fundamental & Applied Nano Electro Magnetics, Minsk, Belarus, 22–25 May 2012; Belarusian State University: Minsk, Belarus, 2012; p. 11.
77. Zhang, Z.; Yang, Y.; Penev, E.S.; Yakobson, B.I. Elasticity, flexibility, and ideal strength of borophenes. *Adv. Funct. Mater.* **2017**, *27*, 1605059. [CrossRef]
78. Martin, P.M. Active thin films: Graphene-related materials graphene oxide and borophene. *Vac. Technol. Coat.* **2018**, *19*, 6–13.
79. Martin, P.M. Active thin films: Applications for graphene and related materials. *Vac. Technol. Coat.* **2018**, *19*, 6–14.
80. Zhao, Y.; Xu, Q.; Simpson, L.J.; Dillon, A.C. Prediction of diamond-like, metallic boron structures. *Chem. Phys. Lett.* **2010**, *496*, 280–283. [CrossRef]
81. Zabolotsky, A.D.; Lozovik, Y.E. Strain-induced pseudomagnetic field in Dirac semimetal borophene. *arXiv* **2016**, arXiv:1607.02530v2. [CrossRef]
82. Zhou, X.-F.; Oganov, A.R.; Wang, Z.; Popov, I.A.; Boldyrev, A.I.; Wang, H.-T. Two-Dimensional magnetic boron. *Phys. Rev. B* **2016**, *93*, 085406. [CrossRef]
83. Chkhartishvili, L. *Quasi-Classical Theory of Substance Ground State*; Technical University Press: Tbilisi, Georgia, 2004.
84. Chkhartishvili, L.; Mamisashvili, N.; Maisuradze, N. Single-Parameter model for multi-walled geometry of nanotubular boron. *Solid State Sci.* **2015**, *47*, 61–67. [CrossRef]
85. Chkhartishvili, L. Boron quasi-planar clusters. A mini-review on diatomic approach. In Proceedings of the IEEE 7th International Conference on Nanomaterials: Applications and Properties, Part 4, Track: Nanomaterials for Electronics, Spintronics and Photonics, Zatoka, Ukraine, 10–15 September 2017; Pogrebnjak, A.D., Ed.; Sumy State University: Sumy, Ukraine, 2017; pp. 1–5.
86. Chkhartishvili, L. Relative stability of planar clusters $B_{11}$, $B_{12}$, and $B_{13}$ in neutral- and charged states. *Char. Appl. Nanomater.* **2018**, *1*, 3. [CrossRef]
87. Chkhartishvili, L.; Murusidze, I. Frequencies of vibrations localized on interstitial metal impurities in beta-rhombohedral boron based materials. *Am. J. Mater. Sci.* **2014**, *4*, 103–110.
88. Chkhartishvili, L.; Tsagareishvili, O.; Gabunia, D. Isotopic expansion of boron. *J. Metall. Eng.* **2014**, *3*, 97–103. [CrossRef]
89. Chkhartishvili, L.S. Volume of the intersection of three spheres. *Math. Notes* **2001**, *69*, 421–428. [CrossRef]
90. Chkhartishvili, L.S. Iterative solution of the secular equation. *Math. Notes* **2005**, *77*, 273–279. [CrossRef]

91. Chkhartishvili, L.; Lezhava, D.; Tsagareishvili, O. Quasi-classical determination of electronic energies and vibration frequencies in boron compounds. *J. Solid State Chem.* **2000**, *154*, 148–152. [CrossRef]
92. Chkhartishvili, L. Quasi-classical approach: Electronic structure of cubic boron nitride crystals. *J. Solid State Chem.* **2004**, *177*, 395–399. [CrossRef]
93. Chkhartishvili, L.S. Quasi-classical estimates of the lattice constant and bandgap of a crystal: Two-dimensional boron nitride. *Phys. Solid State* **2004**, *46*, 2126–2133. [CrossRef]
94. Chkhartishvili, L. Density of electron states in wurtzite-like boron nitride: A quasi-classical calculation. *Mater. Sci. Ind. J.* **2006**, *2*, 18–23.
95. Chkhartishvili, L.; Murusidze, I.; Darchiashvili, M.; Tsagareishvili, O.; Gabunia, D. Metal impurities in crystallographic voids of beta-rhombohedral boron lattice: Binding energies and electron levels. *Solid State Sci.* **2012**, *14*, 1673–1682. [CrossRef]
96. Chkhartishvili, L.; Berberashvili, T. Intra-atomic electric field radial potentials in step-like presentation. *J. Electr. Magn. Anal. Appl.* **2010**, *2*, 205–243. [CrossRef]
97. Froese–Fischer, C. *Th eHartree–Fock Method for Atoms. A Numerical Approach*; Wiley: New York, NY, USA, 1977.
98. Radtsig, A.A.; Smirnov, B.M. *Parameters of Atoms and Atomic Ions. Reference Book*; Energoatomizdat: Moscow, Russia, 1986.
99. Galvez, F.J.; Buendia, E.; Sarsa, A. Excited states of boron isoelectronic series from explicitly correlated wave functions. *J. Chem. Phys.* **2005**, *122*, 154307. [CrossRef] [PubMed]
100. Dahm, T.; Schopohl, N. Fermi surface topology and the upper critical field in two-band superconductors—Application to $MgB_2$. *Phys. Rev. Lett.* **2003**, *91*, 017001. [CrossRef] [PubMed]


condensed matter

MDPI

*Brief Report*

# Simulation of the Process of Obtaining Nanoparticles by Thermal Decomposition

**Anastasiya Kuzmicheva [1,*], Victor Kosushkin [2,*] and Leo Kozhitov [2,*]**

[1] Kaluga Branch of Moscow State Technical University, Bazhenov St., 248001 Kaluga, Russia
[2] Moscow Institute of Steel and Alloys, Leninsky Prospect, 196036 St. Petersburg, Russia
* Correspondence: kao1996@rambler.ru (A.K.); kosushkin@gmail.com (V.K.); kozitov@rambler.ru (L.K.)

Received: 26 December 2018; Accepted: 26 January 2019; Published: 29 January 2019

**Abstract:** In this work, the possibility of modeling the process of thermal decomposition in the COMSOL Multiphysics program for the preparation of nanoparticles of metals and their alloys was determined. To identify the most suitable pyrolysis medium, two environments are presented: a water solution and ethanol.

**Keywords:** nanoparticles; thermal decomposition method; pyrolysis; laminar flow

## 1. Introduction

Today, nanopowders are in great demand for the creation of new materials and technologies, fundamentally new devices. The process of obtaining nanopowders is therefore an important direction in nanotechnology.

The synthesis of nanocrystalline powders of metals and compounds using pyrolysis is associated with the use of complex and organometallic compounds. Numerous studies show that thermal decomposition is a complex process, depending on a variety of parameters. Therefore, the current task is to develop synthesis methods, that is, the simulation of deposition modes in which the most accurate particles can be obtained. By changing the conditions for thermal decomposition and input parameters, one can control the quality and morphology of the resulting metal nanoparticles.

The goal of this work was to analyze a model for obtaining nanopowders by thermal decomposition. The relevance of the pyrolysis process is that the rate of the formation and growth of metal nanoparticles is regulated by changes in the ratio of the number of reactants and the process temperature. Using this method, metal powders were obtained with a particle size in the range of 10–100 nm.

## 2. Thermal Decomposition Modeling Using COMSOL Multiphysics

The preparation of nanopowders of metals and compounds using pyrolysis is associated with the use of complex and organometallic compounds, such as polymers, hydroxides, carbonates, formates, nitrates, oxalates, and acetates. Heating precursors to a certain temperature is a consequence of their decomposition, resulting in the formation of the synthesizing substance and the release of the gas phase [1].

Powders of highly dispersed metals are obtained by the pyrolysis of various salts. By carrying out the thermal decomposition of iron, nickel, and copper formats in vacuum or inert gas, it is possible to obtain metal powders with a particle size ranging from 100 to 300 nm [2].

Thermal decomposition is an imperative process. Nanoparticles of various metals can be obtained by selecting and changing the parameters of the environment in which the process occurs. The model under review explored the single molecular decomposition of a chemical passing through a parallel plate reactor. Its scheme is shown in Figure 1. After entering the reactor, the liquid first experienced expansion as it passed through the bottom plate, then through a heating cylinder [3].

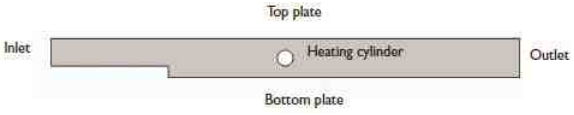


**Figure 1.** 2D representation of the modeling diagram.

The analysis showed that, with such a geometry, the velocity of the laminar flow couldbe described by a parabolic equation

Two media were chosen to represent the pyrolysis process model: a water solution and ethanol. The following are the results of the work focusing on a method for choosing a more favorable environment for thermal decomposition.

The liquid solution enters the reactor at a temperature of 300 K and then it is heated when passing through the cylinder. Figure 2 shows the temperature distribution in the reactor domain in the steady state.

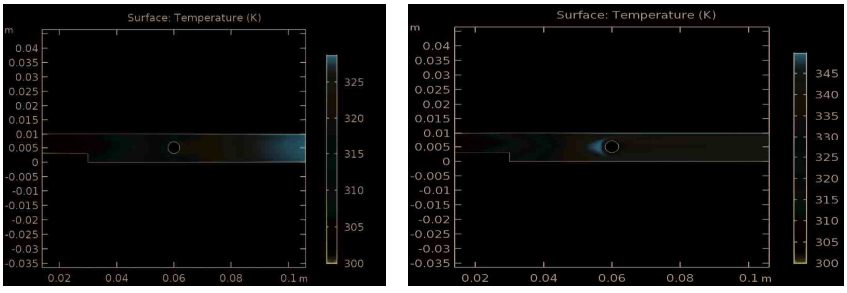


(**a**) (**b**)

**Figure 2.** Temperature distribution: (**a**) in a water solution, (**b**) in ethanol.

It can be concluded that the water, passing through the cylinder, heats up and reaches high values only in the right side of the reactor. The maximum temperature is 330 K. In the case of ethanol, the high temperature covers almost the entire area of the reactor, including the cylinder, where the maximum temperature reaches 350 K.

The distribution of the concentration of main carriers also depends on the choice of medium where pyrolysis will occur. Figure 3 illustrates the concentration of a thermosensitive chemical (mol/m$^3$), depending on the position in the reactor.

These graphs reveal some differences. In Figure 3a, it can be seen that decomposition occurs mainly after the liquid has been heated by the cylinder. In the first half of the reactor, where the temperature is relatively low, decomposition occurs near the walls. In the second part of the reactor, where heating occurs, areas with relatively low concentrations are visible. This has a physical meaning since the water velocity is relatively high. With regard to decomposition in ethanol, Figure 3b proves that decomposition occurs only in the left part of reactor; in the right part, the concentration is close to zero.

Figure 4 shows the reaction rate depending on the position in the reactor.

It can be seen from the figures that the maximum rate of thermal decomposition in water is observed only at the boundaries of the lower and upper plate of the reactor. During pyrolysis in ethanol, we observed the maximum temperature in almost all the reactor. Therefore, we can conclude that of the two environments presented above, ethanol is the most suitable one for the pyrolysis process.

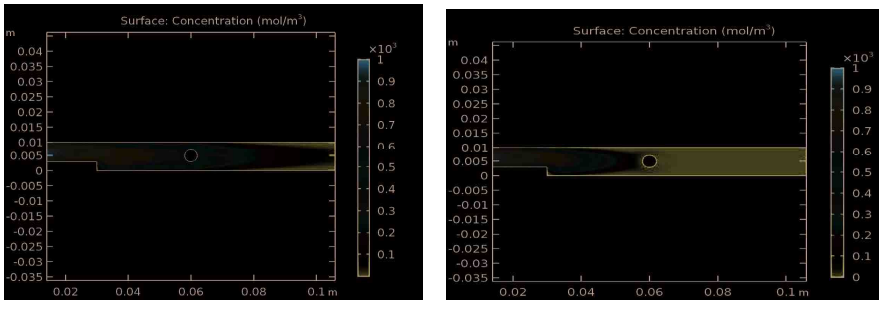


(**a**) (**b**)

**Figure 3.** Thermal decomposition concentration: (**a**) in a water solution, (**b**) in ethanol.

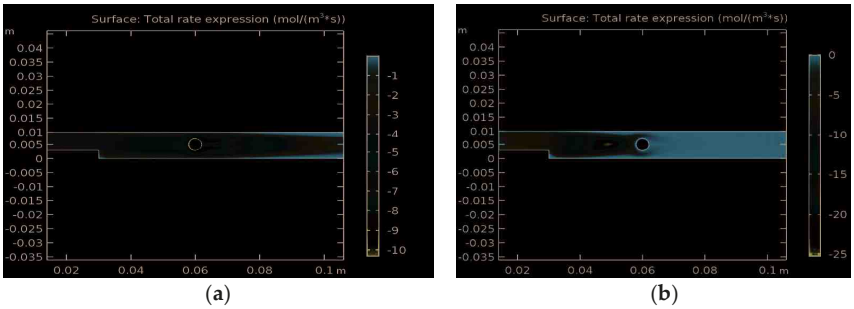


(**a**) (**b**)

**Figure 4.** Speed reaction: (**a**) in a water solution, (**b**) in ethanol.

## 3. Conclusions

The possibility of using the COMSOL Multiphysics package to simulate the process of obtaining nanoparticles by thermal decomposition was determined. The results of pyrolysis in two environments were presented and described, resulting in the choice of the most favorable one for this process.

**Author Contributions:** V.K. and L.K. provided the necessary theoretical materials, A.K. performed experiments and analyzed data.

**Funding:** This research received no external funding.

**Conflicts of Interest:** The authors declare no conflict of interest.

## References

1. Rempel, A.A. Nanotechnologies. Properties and applications of nanostructured materials. *Russian Chem. Rev.* **2007**, *76*, 435–461. [CrossRef]
2. Choi, C.J.; Tolochko, O.; Kim, B.K. Preparation of iron nanoparticles by chemical vapor condensation. *Mater. Lett.* **2002**, *56*, 289–294. [CrossRef]
3. Thermal Decomposition (In Chinese). Available online: https://cn.comsol.com/model/thermal-decomposition-2164 (accessed on 15 September 2018).

MDPI
St. Alban-Anlage 66
4052 Basel
Switzerland
Tel. +41 61 683 77 34
Fax +41 61 302 89 18
www.mdpi.com

*Condensed Matter* Editorial Office
E-mail: condensedmatter@mdpi.com
www.mdpi.com/journal/condensedmatter

MDPI
St. Alban-Anlage 66
4052 Basel
Switzerland

Tel: +41 61 683 77 34
Fax: +41 61 302 89 18

www.mdpi.com


ISBN 978-3-03921-969-8